THE EFFECT OF IONOSPHERIC CONDUCTIVITY ON MAGNETOSPHERIC DYNAMICS

BY

JOSEPH B. JENSEN

BS, Physics, Utah State University, Logan UT, 2013

DISSERTATION

Submitted to the University of New Hampshire
in Partial Fulfillment of
the Requirements for the Degree of

Doctor of Philosophy

in

Physics

June 2018

This dissertation has been examined and approved in partial fulfillment of the requirements for the degree of Doctor of Philosophy in Physics by:

Dissertation Advisor, Joachim Raeder,
Professor, Department of Physics
University of New Hampshire

Lynn Kistler,
Professor,Department of Physics
University of New Hampshire

Kai Germaschewski,
Associate Professor, Department of Physics
University of New Hampshire

Marc Lessard,
Associate Professor, Department of Physics
University of New Hampshire

Simon G. Shepherd,
Associate Professor of Engineering
Thayer School of Engineering at Dartmouth College

on 13 June 2018.

Original approval signatures are on file with the University of New Hampshire Graduate School.

This thesis is dedicated to my wife Tesha S. Harris Jensen.

ACKNOWLEDGMENTS

This is where I say thanks to all the people that helped me with this dissertation and my education here at UNH.

First off, thanks to Jimmy Raeder for being my thesis advisor and research mentor. He took a great gamble bringing me into the research group right when I got to UNH and I hope it has payed off. I have learned much from him.

My Wife Tesha S. Jensen has been an excellent support throughout undergraduate, and graduate school, and I am sure she is just as happy as I am to be done with school. My children, Benjamin, Zachary, Leah, Catharine, and Number 5, have been great sports for all the times that I have had to tell them that "Daddy has some homework to do." They are one of the main reasons I am doing this, so they will grow up knowing how important it is to gain a knowledge of things as they are.

Thanks to the physics department at UNH. I have had many wonderful teachers who have inspired me to think about how I perceive the world, which is the best compliment that I can give.

I would like to thank my family, my father, Robin S. Jensen, who inspired a curiosity of how things work in me at a young age. He is always getting lost in books and museums, and I now find getting lost in books or museums to be a fantastic opportunity. My mother Eleanor J. Jensen has always inspired me to be the best I can, and supported me always.

Thanks to Trillian, perhaps my wife is a little bit jealous how much time I spent with her, but it has been fantastic having our very own supercomputer here on campus. I have been absolutely spoiled during my graduate career. Computations were performed on Trillian, a Cray XE6m-200 supercomputer at UNH supported by the NSF MRI program under grant PHY-1229408.

Thanks to the New Hampshire Space Grant Consortium for sponsoring one of my years here at UNH, that is an awesome program and I have benefitted highly from it. I am also very grateful for the federal grants from both NASA and NSF that Jimmy received that have supported me during my years here at UNH, they are NSF grant AGS-1603021, NASA grant NNX15AW16G, NASA LWS grant NNX13AK31G.

TABLE OF CONTENTS

LIST OF TABLES

Table **Page**

LIST OF FIGURES

Figure **Page**

ABSTRACT

The Effect of Ionospheric Conductivity on Magnetospheric Dynamics

by

Joseph B. Jensen

University of New Hampshire, June, 2018

The connection between ionospheric conductivity and the dynamics of the magnetosphere was investigated, using several methods to change the ionospheric conductivity and then study the resultant changes to the magnetosphere. Computer simulations of the Earth's geospace environment were utilized using OpenGGCM coupled with an ionosphere model CTIM and a ring current model RCM.

Three methods were used to modify ionospheric conductivity. The incoming particle precipitation was modified by several orders of magnitude $\alpha = .01, .1, 1, 10$, the ionospheric conductivity was increased or decreased by factors $\beta = .25, .5, 1, 2,$ and 4, and for the last method differing values of $F_{10.7}$, $70, 110, 150, 200,$ and 250 were used. Each of the methods is different because $F_{10.7}$ mostly affects the dayside, while precipitation mostly affects the nightside, then using the β changes the conductivity over the whole ionosphere. This gives a good range for studying the effects of ionospheric conductivity on the magnetosphere.

The magnetospheric dynamics studied are: the dayside magnetopause location, the reconnection rate of the Earth's magnetosphere, X-line formation in the magnetotail, and substorm dynamics, both the frequency and magnitude of substorm occurrence.

To understand the effect of particle precipitation on conductivity two events were simulated, a calm period on 4 May 2005 and a strong storm period on 17 March 2013. Scaling the precipitation energy flux by several orders of magnitude, conductivities in the auroral oval were influenced which, in turn, influence the cross polar cap potentials. With the change in conductance, magnetospheric convection is enhanced or reduced, and the location of the subsolar distance of the magnetopause can change by up to one R_E. The investigation of the reconnection rate for the varying precipitation simulations using the Hesse-Forbes-Bern method shows that particle precip-

itation affects the magnetic reconnection rate in these two events. The most notable differences, up to 40%, occur on short time scales, that is, hours. A relation for longer time scales (tens of hours) between precipitation and reconnection for these two events is more difficult to ascertain. Differences in cross polar cap potential (CPCP) and reconnection rate (R) can be explained by viscous interactions and polar cap saturation. When precipitation was decreased, polar conductance was decreased, viscous interactions are stronger, and CPCP is higher than R. For high precipitation, high conductance cases the polar cap is in the saturation regime and CPCP is lower than R. Hemispheric asymmetries were found in the cross polar cap potential and in the calculated reconnection rate derived from the Northern and Southern Hemispheres. The majority of this research has already been published in the Journal of Geophysical Research: Space physics, "Particle Precipitation Effects on Convection and the Magnetic Reconnection Rate in Earth's Magnetosphere" https://doi.org/10.1002/2017JA024030

For the whole ionospheric conductivity study, different values of $\beta =, .25, .5, 1, 2, 4$ were used to modify the ionospheric conductivity after it had been calculated by the ionosphere model. A moderate storm period, 16 May 2011 was simulated. Many of the same conclusions found in the precipitation study were found in this study as well, such as, CPCP decreasing as conductivity increases, the point at which the polar cap saturates decreases with increasing conductivity, and reconnection rates change on short time scales, but the overall average rate remains very similar. The incoming precipitation was used to identify auroral brightening that is linked with substorms. The criteria for auroral brightenings used in this study is where the maximum precipitation increased by at least $1\ mW/m^2$ within 20 minutes. The criteria for substorms is that the maximum precipitation increases by 80% within 20 minutes. Identifying all the auroral brightenings and substorms showed that as conductivity increased the maximum amount of precipitation decreased, and also the number and frequency of both the substorms and auroral brightenings decreased. The occurrence of extended X-lines in the magnetotail was analyzed, where if an earthward flow of greater than 50 km/s extended for greater than 10 R_e in Y_{GSE} was classified as an extended X-line. This is not to be confused with a bursty bulk flow or dipolarization front, which happen from reconnection but usually do not have a large extent in Y_{GSE}. Identifying extended X-lines in this manner showed a similar trend that as conductivity increased the number of extended X-lines decreased, and while

there was not much of an indication if the size or location is affected much, the amount of time the simulation had extended X-lines present decreased.

For the $F_{10.7}$ study, using values of $70, 110, 150, 200,$ and 250, the ionospheric conductivity was influenced mostly on the dayside. A day during the spring equinox was simulated with ideal solar wind conditions as well as the 16 May 2011 storm period. The main results found is that $F_{10.7}$ does not affect the system as much as the precipitation study, or the whole ionosphere conductivity study, but there are still some indications that show the same conclusions obtained previously.

CHAPTER 1

INTRODUCTION

1.1 Introduction

This dissertation is divided into three chapters. The first is the introduction and background material. The second chapter deals with the importance of ionospheric conductivity due to particle precipitation. The material is taken from Jensen et al. (2017). Chapter three contains two studies where the ionospheric conductivity is modified as a whole over the entire ionosphere, and with changing $F_{10.7}$.

1.2 The Sun and Solar Wind

The most important object that is essential for all life in our solar system is the Sun. The sun is a massive sphere of plasma that is under such great pressure from it's own gravitational forces that fusion occurs in its core from four hydrogen atoms that bond together to make a helium atom releasing the energy making our lives on earth possible. The energy takes a multi-million year long trip through the sun's layers and reaches the surface of the sun at the photosphere, and the energy is released to warm our planet.

The photosphere is roughly 6000 degrees K and has lots of features, including sunspots, coronal holes, and active regions. Magnetic reconnection of field lines occurs at active regions where magnetic energy is converted into kinetic and thermal energy resulting in explosions of energy and mass from the surface of the sun. The mass accelerated from the surface of the sun in this manner is called a coronal mass ejection (CME). These particles interact with the solar wind particles that are streaming off the sun and cause the solar wind to speed up.

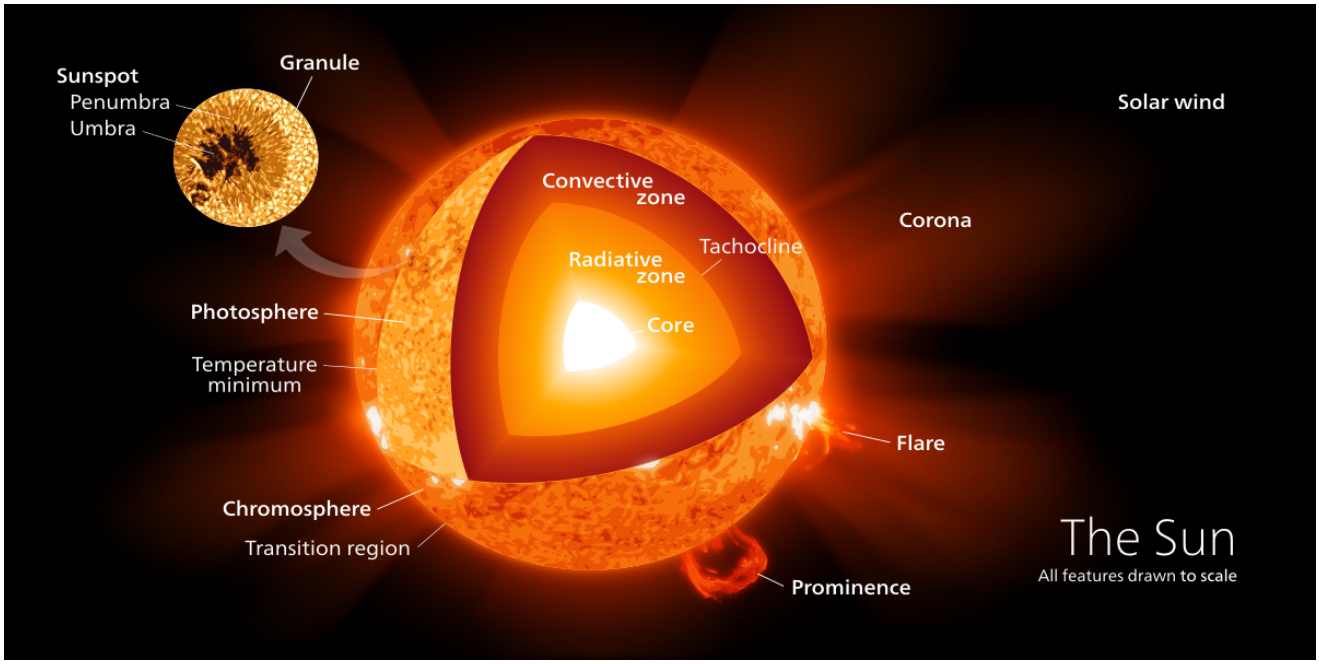

Figure 1.1: Diagram of the interior of the sun and important processes that occur on the surface of the sun, (By Kelvinsong - Own work, CC BY-SA 3.0, https://commons.wikimedia.org/w/index.php?curid=23371669).

From looking at comets tails scientists theorized that there must be some "wind" that is blowing the comet tails away from the sun, and that it must be there all of the time (Biermann, 1951). Parker (1958) showed the theoretical background and predicted a supersonic solar wind that leaves the sun, showing that at a critical point (about 10 solar radii) the solar wind transitions from a subsonic to supersonic solar wind. The existence of the solar wind was later confirmed through satellite observations of the Luna 1 spacecraft built by the Soviets (Harvey, 2007). Co-rotating interaction regions (CIRs) that originate from field lines tied to coronal holes and CMEs greatly influence the geoeffectiveness of the solar wind. The Solar Probe mission will report data closer to the sun than any previous mission has before.

1.3 Magnetosphere

The earth's magnetosphere is formed by dynamo currents in the earth's molten outer core that surrounds the earth's solid inner iron core. This magnetic field permeates through the earth's crust and for centuries was mapped using compasses and used for navigation on land and sea. The earth's magnetic field extends tens of thousands of kilometers into outer space where it has a profound effect on the plasma surrounding the earth.

1.3.1 Motion of Plasma

The motion of plasma is determined by temperature and pressure similar to gases and fluids on the surface of earth, but since plasma has an electrical charge, the electromagnetic fields from the earth and the impinging solar magnetic field are important for plasma dynamics. They can be described very generally with the Lorentz force equation

$$\mathbf{F} = q(\mathbf{E} + \mathbf{v} \times \mathbf{B}), \tag{1.1}$$

Where $\mathbf{F}$ is the force on the particle, q is the charge of the particle, $\mathbf{E}$ is the electric field, $\mathbf{v}$ is the velocity vector, and $\mathbf{B}$ is the magnetic field. Using the Lorentz force equation coupled with Maxwell's equations and the conservation of energy, one can derive other parameters of single particle motion that must be conserved under adiabatic conditions. These equations determines how charged particles move in electric and magnetic fields. These parameters are often referred to as adiabatic invariants, which describe the motion that charged particles take in a magnetic field.

The first conserved quantity is the magnetic moment, μ

$$\mu = \frac{mv_{\perp}^2}{2B} \tag{1.2}$$

where m is the mass, v is the velocity, and B is the magnetic field. The Lorentz force and conservation of μ result in particles gyrating around magnetic field lines or guiding centers as shown in

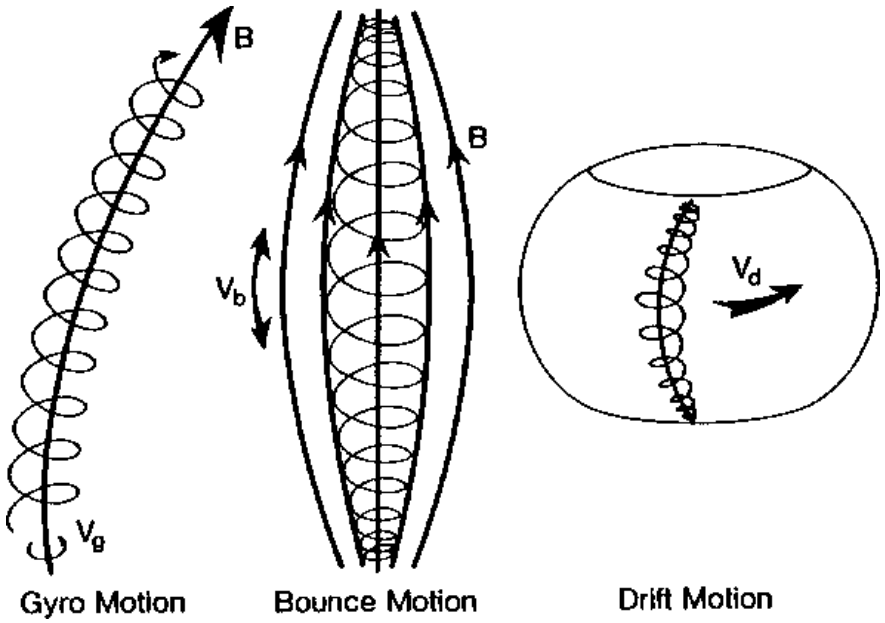

Figure 1.2: Charged particle motion in a magnetic field. Figure from http://www-ssc.igpp.ucla.edu/ssc/tutorial/msphere07.gif.

Figure 1.2. In cases where the particle originally has parallel motion along the magnetic field this results in helical motion along the magnetic field. Since μ is conserved as a particle moves along magnetic field lines, as the magnetic field strengthens to conserve μ, $V_\perp$ increases, which reduces the parallel velocity effectively stopping the particles motion along the field line. The particle then returns along the magnetic field resulting in a bounce motion as shown in Figure 1.2.

A particles pitch angle, α, describes the ratio of perpendicular to parallel velocity

$$\alpha = \tan^{-1}\left(\frac{v_\perp}{v_{||}}\right) \tag{1.3}$$

If particles have sufficiently large parallel velocity compared with their perpendicular velocity, then the particles will not be contained and escape the magnetic trap. The pitch angles at which the parallel velocity is great enough to overcome the magnetic trap is called the loss cone.

The second adiabatic invariant or longitudinal invariant J shows that the particle that is trapped in a magnetic will stay on the same magnetic field line as it bounces back and forth. J is described mathematically as

$$J = m \oint v_{||} ds \tag{1.4}$$

where the integral is along the magnetic field line. The longitudinal invariant remains constant as long as the magnetic fields do not change on the order of the bounce time, which for typical particles in the earth's inner magnetosphere is on the order of a few seconds.

The third adiabatic constant shows that particles on a magnetic field will drift around the earth as shown in Figure 1.2. The third invariant is only valid when the magnetosphere is quiescent on timescales of an hour, and for the earth's magnetosphere this is not often the case.

1.3.2 Structure of the Magnetosphere

Figure 1.3 is a diagram that shows some of the regions of the earth's magnetic field. The solar wind impinges on the earth's magnetic field from the left of Figure 1.3. The bowshock is the point where the supersonic solar wind is slowed down to subsonic which occurs before it makes contact with earth's magnetic field lines. The majority of the subsonic plasma proceeds to move around the magnetosphere through the magnetosheath. The boundary between the magnetosheath and the earth's magnetic field lines is the point where solar magnetic field lines and earth magnetic field lines interact and generate a current sheet at the boundary. This boundary is compressed on the dayside and stretched out on the night side. All magnetic field lines are closed (by Maxwell's equations) but it is common to refer to earth's magnetic field lines that are connected to solar magnetic field lines to be open, these are connected to polar regions of the earth and form the tail lobes. The boundary between the tail lobes is the plasma sheet. Figure 1.4 shows the major current systems in the magnetosphere. The magnetopause currents arise because there needs to be a boundary between the solar winds magnetic field and the earth's magnetic field. The only way to have the magnetic fields change is to have a current sheet at the boundary. The cross tail current sheet arises from the solar wind blowing past the magnetosphere and Amperes law must be satisfied so current is transported along the tail and over the lobes. The Birkeland current sheets are believed to arise from current being diverted from the cross tail current sheet, and close through

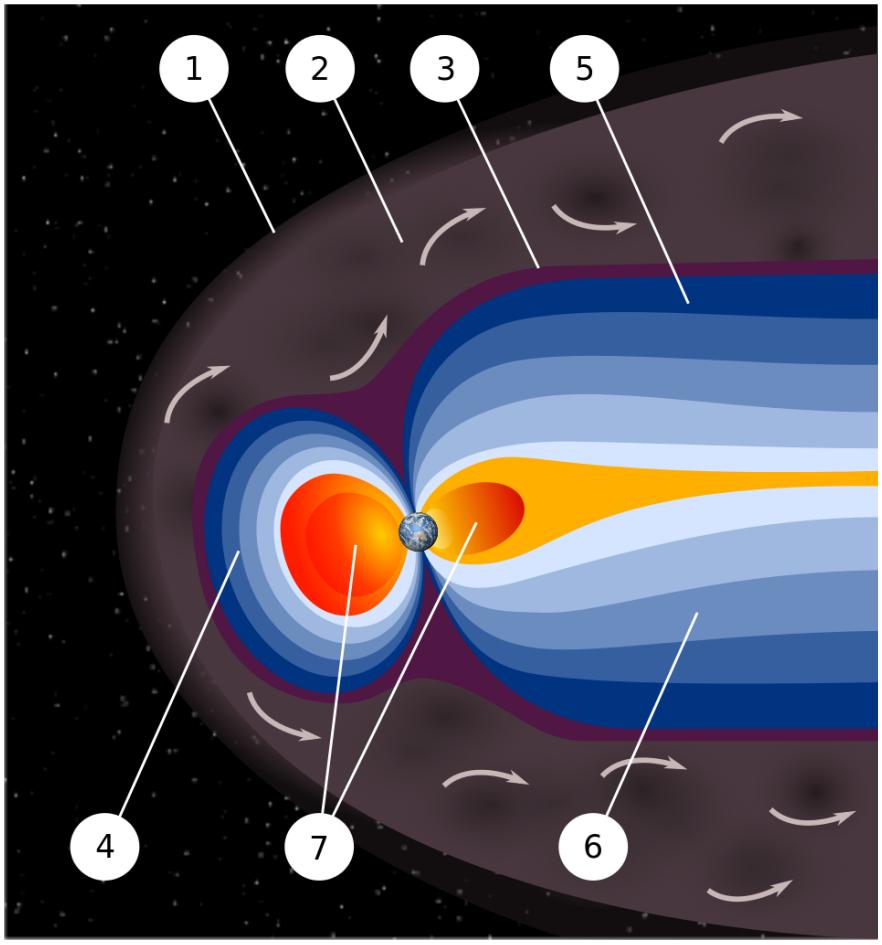

Figure 1.3: Diagram of the main parts of the earth's magnetosphere, 1) Bow shock, 2) Magnetosheath, 3) Magnetopause, 4) Magnetosphere, 5) Northern tail lobe, 6) Southern tail lobe, 7) Plasmasphere. The sun would be to the left of the figure. Figure is in Public Domain, https://commons.wikimedia.org/w/index.php?curid=9608059.

the ionosphere (Kepko et al., 2015). Ionospheric conductivity is an important factor to determine when, and how much current is supplied to the ionosphere.

1.3.3 Magnetohydrodynamics

Physics is the attempt to understand and predict with the language of mathematics future outcomes from the things seen around us. There are a few ways to describe electromagnetic fields and plasma in the geospace environment. One way is using the actual particles themselves and map out their motions and keep track of all the dynamics of each individual particle by using a distribution function that keeps track of the position and velocity of each particle in time. This is

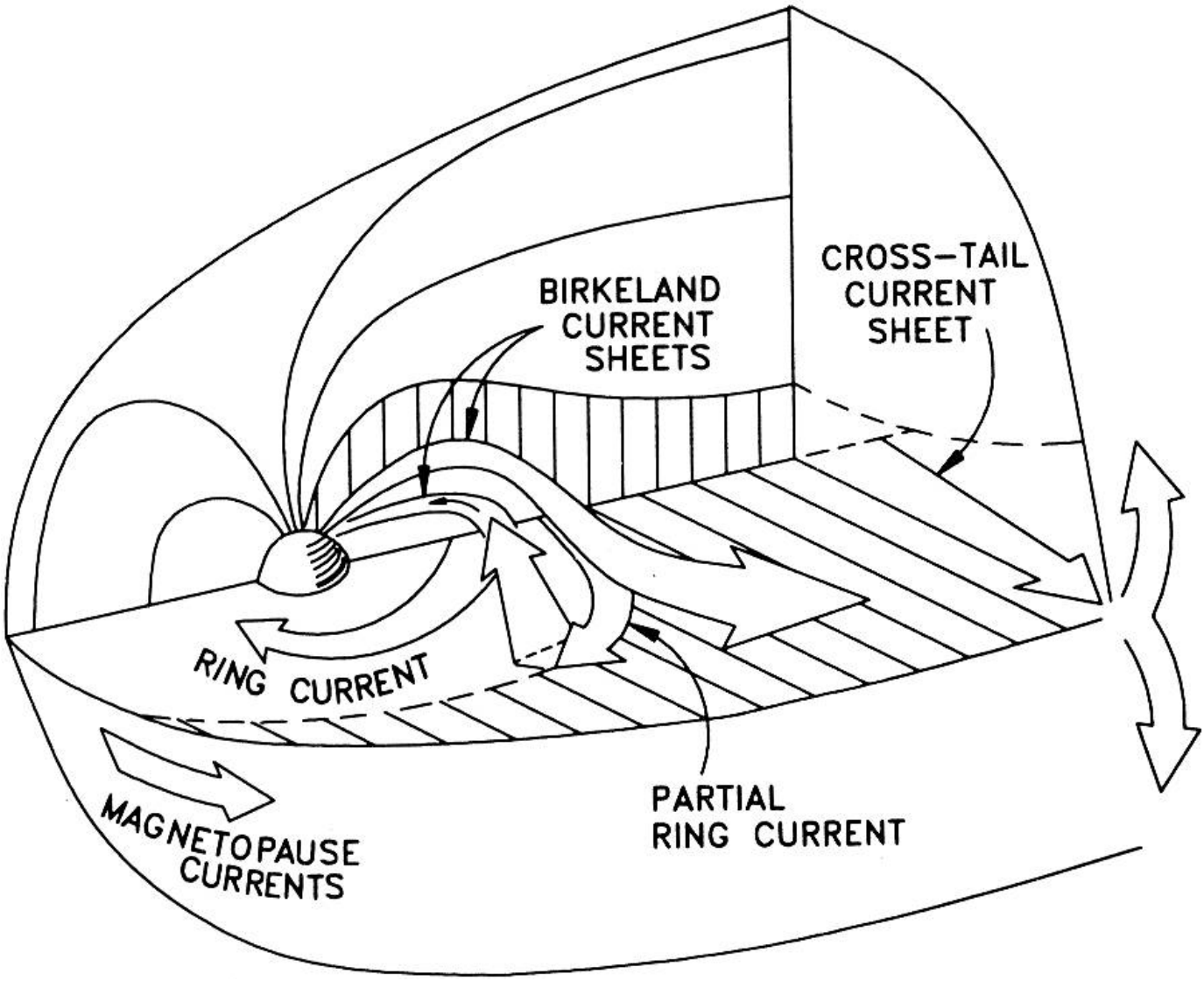

Figure 1.4: Major current systems in the earth's magnetosphere. Figure from Stern (1994).

accomplished using the Vlasov equation, which is also called the collisionless Boltzmann equation since he derived the statistical relation for fluids originally.

$$\frac{\partial f}{\partial t} + \mathbf{v} \cdot \frac{\partial f}{\partial \mathbf{r}} + \frac{q}{m}(\mathbf{E} + \mathbf{v} \times \mathbf{B}) \cdot \frac{\partial f}{\partial t} = 0 \tag{1.5}$$

where f is the distribution function for the particles, $\mathbf{v}$ is the velocity, $\mathbf{r}$ is the position, q, m, E, and B are the same as described in Equation 1.1.

Using the Vlasov equation to evolve a particle distribution function is the method used in particle in cell codes. Tracking each particle requires significant computer resources and constrains the size of the system to be simulated. That is why many simulations use a fluid description of plasma. This is done by taking velocity moments of the Vlasov equation which results in variables such as density and temperature and then using Maxwell's equations for the electric and magnetic fields. This is commonly referred to as Magnetohydrodynamics or MHD. The MHD equations that are used in the Open Geospace General Circulation Model(OpenGGCM) are shown here in the semi-conservative form.

$$\frac{\partial \rho}{\partial t} = -\nabla \cdot (\rho \mathbf{v}) \qquad \textit{(Mass Conservation)} \tag{1.6}$$

$$\frac{\partial (\rho \mathbf{v})}{\partial t} = -\nabla \cdot (\rho \mathbf{v}\mathbf{v} + pI) + \mathbf{j} \times \mathbf{B} \qquad \textit{(Momentum Conservation)} \tag{1.7}$$

$$\frac{\partial e}{\partial t} = -\nabla \cdot (\{e + p\}\mathbf{v}) + \mathbf{j} \cdot \mathbf{E} \qquad \textit{(Energy Conservation)} \tag{1.8}$$

$$\frac{\partial \mathbf{B}}{\partial t} = -\nabla \times \mathbf{E} \qquad \textit{(Faraday's Law)} \tag{1.9}$$

$$\nabla \cdot \mathbf{B} = 0 \tag{1.10}$$

$$\mathbf{E} = -\mathbf{v} \times \mathbf{B} + \eta \mathbf{j} \qquad (Ohm's\ Law) \tag{1.11}$$

$$\mathbf{j} = \nabla \times \mathbf{B} \tag{1.12}$$

$$e = \frac{\rho v^2}{2} + \frac{p}{\gamma - 1} \qquad \textit{(Plasma Energy)} \tag{1.13}$$

Where ρ and $\mathbf{v}$ are the density and velocity, p is plasma pressure, I is the unit tensor, $\mathbf{j}$ is the current density $\mathbf{B}$ is the magnetic field, e is the energy of the plasma, $\mathbf{E}$ is the electric field, γ is the ratio of the specific heats, and η is the anomalous diffusion.

The anomalous diffusion, η, is parameterized by,

$$\eta = \alpha j'^2 \quad \text{if} \quad j' \geq \delta, \quad 0 \text{ otherwise} \tag{1.14}$$

where α and δ are empirical constants, and j' is a normalized local current density given by,

$$j' = \frac{|j|\Delta}{|B| + \epsilon}. \tag{1.15}$$

For further reference on why the semi-conservative formalism is used, see Raeder (2003). It is important to note that the semi-conservative formulation allows for numerical difference schemes that allow the conservation of the plasma mass, momentum, and energy, but with no strict conservation of the total energy.

MHD is a powerful tool that can be applied to many systems, for example how the plasma in stars convect, how to confine plasma in tokamaks to produce energy. The Japanese even built a boat that propelled itself using MHD principles on the ocean, using the salt water as the conductive fluid. MHD works very well for much of the earth's magnetosphere, but there are some locations where the assumptions required for valid MHD break down, these assumptions are listed here,

- The length scales must be large compared to gyroradius of the particle and Debye lengths given as,

$$r_g = \frac{m v_\perp}{|q|B}\ , \qquad \text{and,} \qquad \lambda_D = \sqrt{\frac{\epsilon_0 k_B T_e}{n_e {q_e}^2}}. \tag{1.16}$$

  where r_g, m, $v_\perp$, q, ϵ_0, k_B, T_e, and, n_e are gyroradius, mass, velocity perpendicular to the magnetic field, elementary charge, permittivity of free space, Boltzmans constant, electron temperature, and density of electrons.

- The time scales must be long compared to the gyroperiod given as,

$$T_g = \frac{2\pi r_g}{v_\perp}\ . \tag{1.17}$$

  where T_g is the gyroperiod.

- Isotropic pressure is assumed in the momentum equation to have moment closure of the Vlasov equation.

- Quasi-neutrality, the same number of positive and negative charge carriers, is assumed.

These assumptions are valid for many locations in the magnetosphere, but they break down in the ring current where energies are very large and the pressure is not very isotropic. Another place MHD breaks down is in reconnection diffusion regions. Reconnection occurs on time and length scales that are comparable to the ion skin depth, which is given by,

$$\frac{c}{\omega_{pi}} = \sqrt{\frac{m_i}{m_e}}\, c\, \omega_{pe} \tag{1.18}$$

where ω_{pi} and ω_{pe} are the ion and electron plasma frequencies respectively.

There are many different flavors of MHD that scientists use depending on what further assumptions they take for the system they are studying. For example if conductivity is very large Ohm's law simplifies to $\mathbf{E} + (\mathbf{v} \times \mathbf{B}) = 0$ and ideal MHD is used. Multi-fluid MHD is another flavor of MHD that can be used to study multiple different ion species. Despite the few locations of the magnetosphere where MHD breaks down, it is a valuable tool for describing the solar wind-magnetosphere system.

1.3.4 Magnetic Reconnection

In a highly conducting fluid where dissipation is minimal, the magnetic field lines are tied to the plasma. There are places in the magnetosphere that under certain circumstances the frozen in flux approximation breaks down. At any points where a shear in the magnetic field exists, if there is sufficient pressure to have oppositely aligned fields interact, a diffusion region can develop. When this occurs the frozen in flux condition is lost, therefore plasma and fields can realign themselves within the diffusion region. The first to propose this idea were Sweet and Parker in the 1950's. They calculated a rate at which the reconnection occurs and showed that in their model all the plasma and magnetic field needed to be moved through the diffusion region. One of the major drawbacks of their model is that the reconnection rate calculated was too small to match observations on the sun, requiring solar flares to last for a few days instead of minutes.

In 1964 Petschek proposed a modification of the Sweet-Parker reconnection model. Figure 1.5 shows a model of Petschek reconnection (Petschek, 1964; Forbes, 2001) that shows the Sweet-

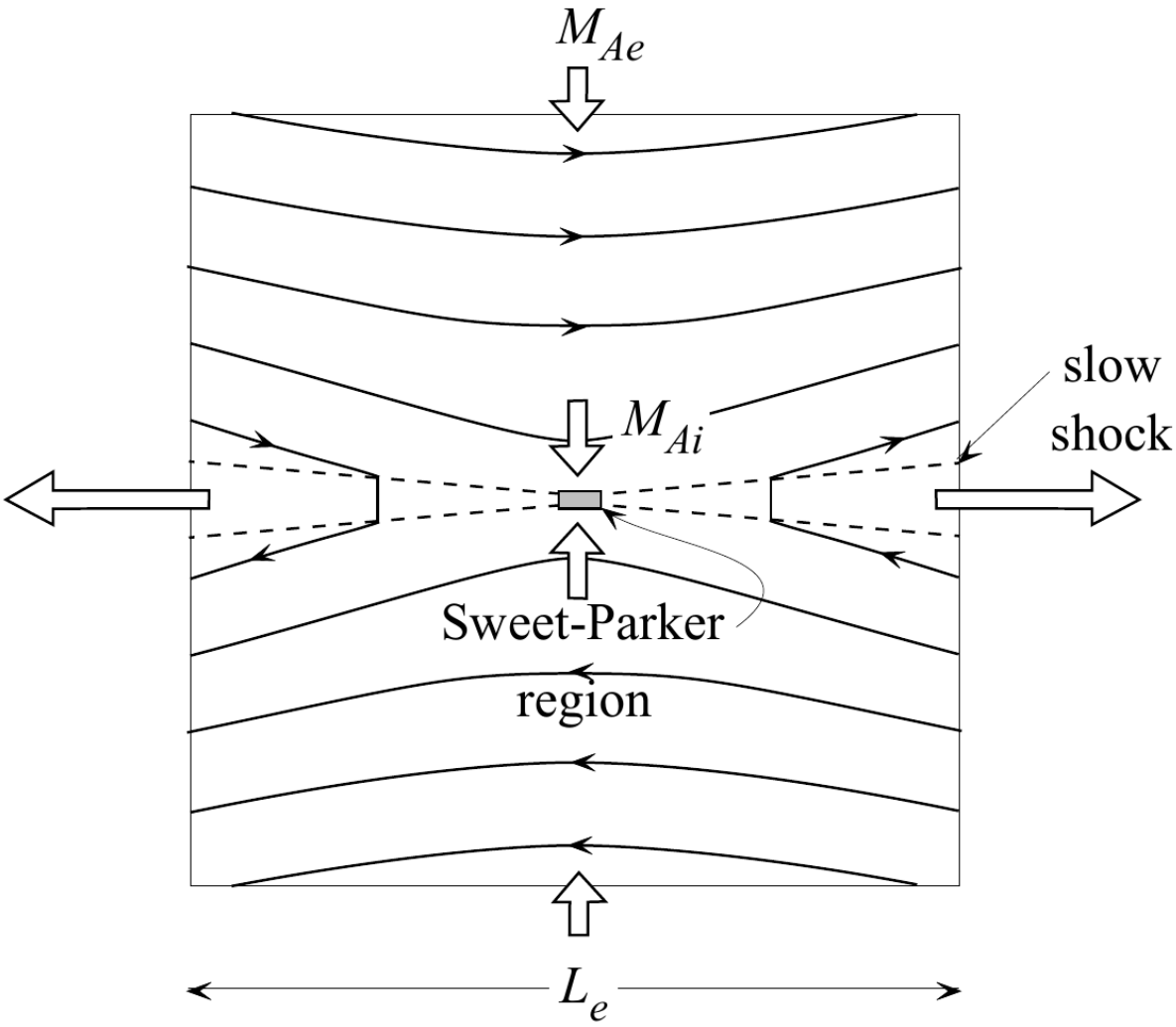

Figure 1.5: Diagram of a cross section of a Petschek magnetic reconnection region with slow mode shocks. Figure from Forbes (2001).

Parker diffusion region in the center. The proposed modification was that all the plasma did not have to pass through the diffusion region, but that the plasma could also be accelerated through slow shocks along the X-line which resulted in a much quicker reconnection rate which matched observations better. This resulted in a reconnection rate of

$$M_{Ae} = \frac{\pi}{8} \ln\left(\frac{L_e V_{Ae}}{\eta}\right)^{-1} \tag{1.19}$$

Where M_{Ae} is the Alfvén mach number, L_e is the length scale, V_{Ae} is the Alfvén speed in the region far upstream of the current sheet, and η is the magnetic diffusivity of the plasma. Scientist have

been trying to understand reconnection for a long time trying to get more accurate representations of the diffusion region by including mathematical terms that hadn't been used previously, such as the Hall term in Ohm's law.

1.3.5 Viscous Interaction

Viscous interaction occurs when the solar wind plasma pulls the plasma just inside the magnetosphere tailward, as shown in Figure 1.6. Some proposed mechanisms for this interaction are Kelvin-Helmholtz instabilities, and turbulence (Farrugia et al., 2001; Cowley, 1982). Viscous interaction is another way in which potential can be generated in the ionosphere from mapped convection patterns in the magnetosphere. It was first proposed by Axford and Hines (1961) the same years as the Dungey (1961) seminal paper on magnetic reconnection.

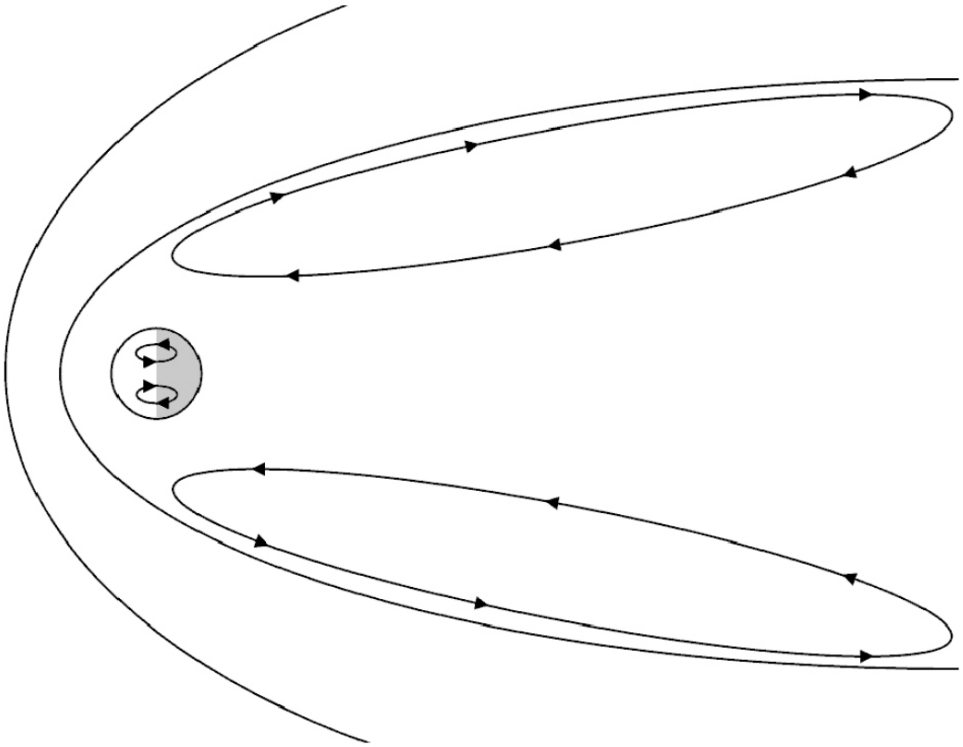

Figure 1.6: Diagram of how the viscous interaction can cause convections cells in the magnetotail to form in the magnetosphere, that then induces convection in the ionosphere. Figure from Bruntz et al. (2012).

Bruntz et al. (2012) carried out MHD simulations with the Lyon-Fedder-Moberry (LFM) Magnetohydrodynamic model from Dartmouth (Fedder et al., 1998), and they tested the dependence of viscous potential on the solar wind velocity and density. They found that as the velocity and density of the solar wind increased the viscous potential induced on the ionosphere increased substantially. The main mechanism whereby the plasma in the magnetosphere is pulled along the solar wind plasma is through Kelvin Helmholtz (K-H) instabilities (Farrugia et al., 2001). This is reasonable because increased density and velocity shears should cause more K-H instabilities and increase the viscous convection cells.

Bruntz et al. (2012) also carried out a study on the viscous interaction dependence on the ionospheric conductivity. They modified the ionospheric conductivity by increasing the Pedersen conductivity uniformly across the polar cap by values ranging from 1 to 30 mhos. Figure 1.7 shows the results they obtained. They found that the viscous potential had an inverse relationship to the conductivity.

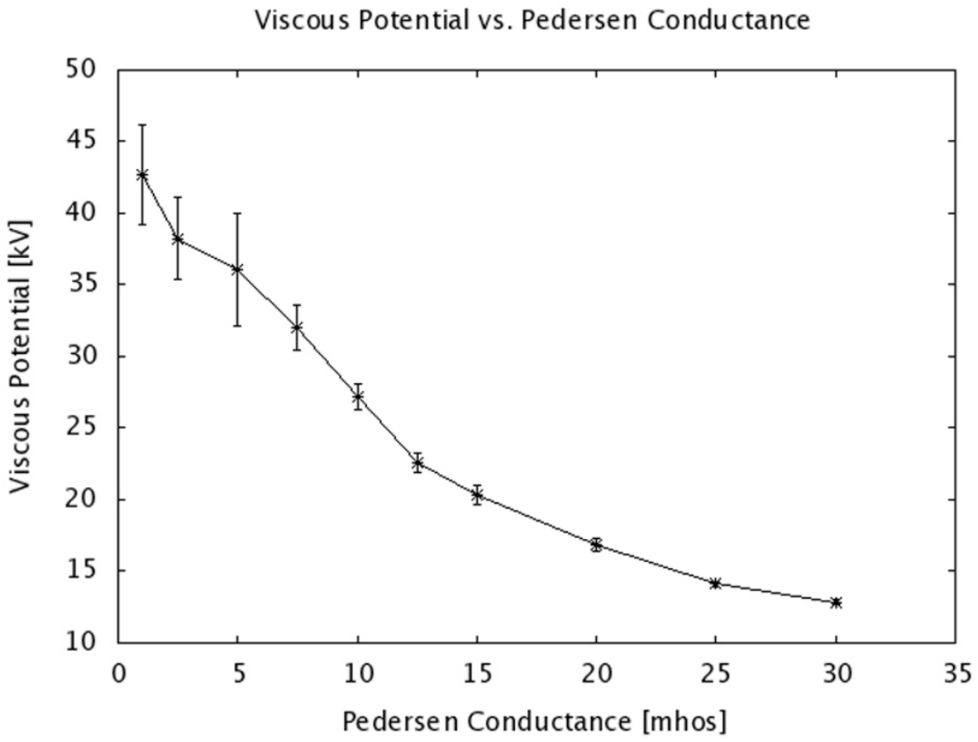

Figure 1.7: Conductivity dependence of the viscous potential, horizontal axis shows the Pedersen conductivity, and the vertical axis shows the potential. Taken from Bruntz et al. (2012).

Viscous potential is usually lower than the reconnection rate and does not have an appreciable contribution to the polar cap potential. When modifying the conductivity to extremes one must consider the contribution from this magnetospheric process.

1.4 Ionosphere

The earth's ionosphere ranges from about 80 km above the surface to upwards of 1000 km. The ionosphere is comprised of electrons and ions. As can be seen from Figure 1.8, O_2^+, and NO^+ are the primary ion species from about 80-150km, and this region of the ionosphere is called the E-region and it has a peak around 110km. O^+ dominates high altitudes with some H^+ and from 150 km above is called the F-region with a peak at around 250km. The ionosphere is primarily formed due to ultraviolet radiation from the sun, but in the polar regions ionization can also be caused by particles streaming from the magnetosphere.

The ionosphere exists in the same place as the thermosphere, or neutral atmosphere, and there are many ways the ionosphere and thermosphere can interact. Some of these processes are neutral winds, diurnal tides that come from the heating and cooling of the atmosphere each day, and gravity waves that come from any disturbances propagating up into the atmosphere such as wind blowing on mountain ranges, hurricanes, or earthquakes.

1.4.1 Photoionization

Photoionization occurs when photons from the ultraviolet (UV) and extreme ultraviolet (EUV) higher energy spectrum are absorbed by neutral particles in the ionosphere causing ionization. The Chapman production function deals with incoming solar radiation and the ionization that occurs,

$$Q = Q_m e^{(1-y-e^{-y})} \tag{1.20}$$

where Q_m, the peak production rate, and y are described as,

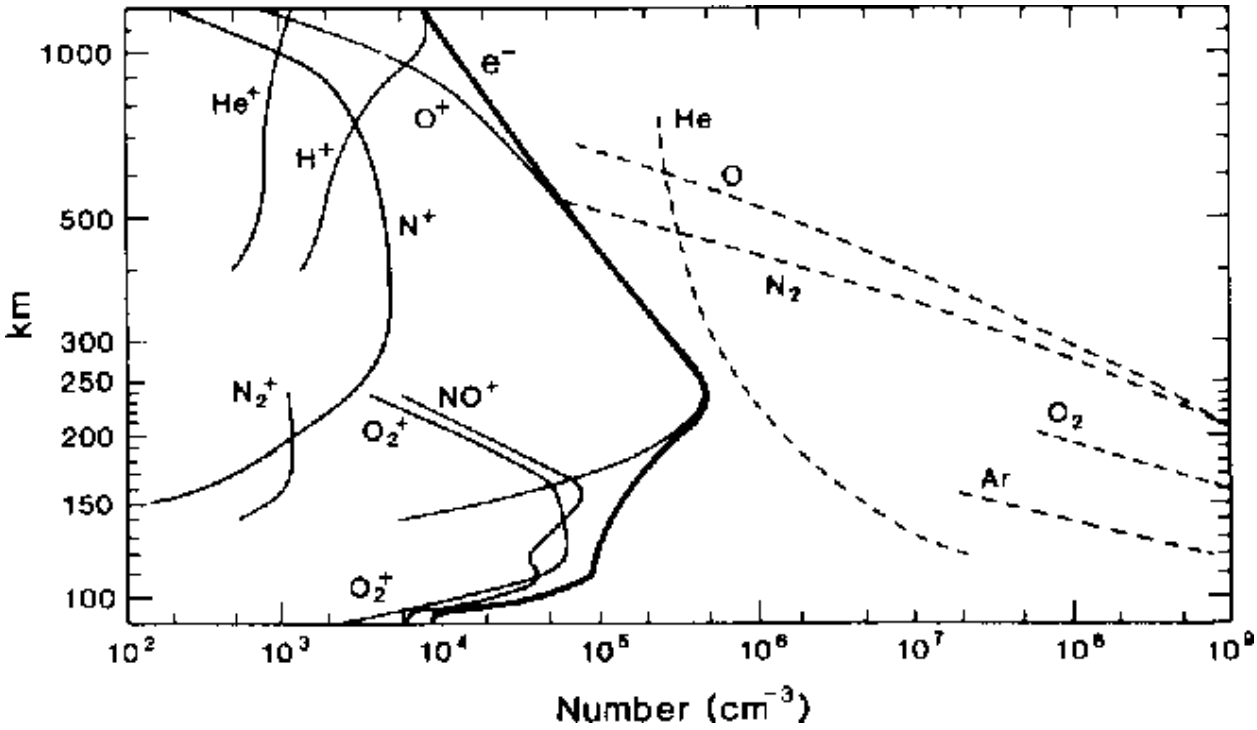

Figure 1.8: Density and composition profile of the ionosphere and thermosphere, vertical axis gives the altitude, while the horizontal axis gives the density (Johnson, 1969; Kivelson and Russell, 1995).

$$Q_m = \left(\frac{CIcos(\chi)}{H_n e}\right) \qquad and, \qquad y = \left(\frac{h_m - h}{H_n}\right) \tag{1.21}$$

Where Q is the production of ions, C is a constant of proportionality that equals 1 ionization for 35 eV (units of number of electrons per eV), I is radiation intensity from the sun (units of energy flux), χ is the solar zenith angle, H_n is the scale height of the neutral particles, which is the distance in altitude one must rise so the pressure decreases by e, and h_m is the height of the peak production.

There are a range of energies important for various regions of the ionosphere as shown in Figure 1.9. The red area shows where the full intensity of the sun interacts with the particles there, where it is black the solar irradiance at that wavelength has been completely absorbed. The extreme ultraviolet 1-10 nm wavelengths that can come from solar flares, can penetrate into the E-region of the ionosphere, and signatures of solar flares can be seen in the ionosphere (Sojka et al., 2013, 2014).

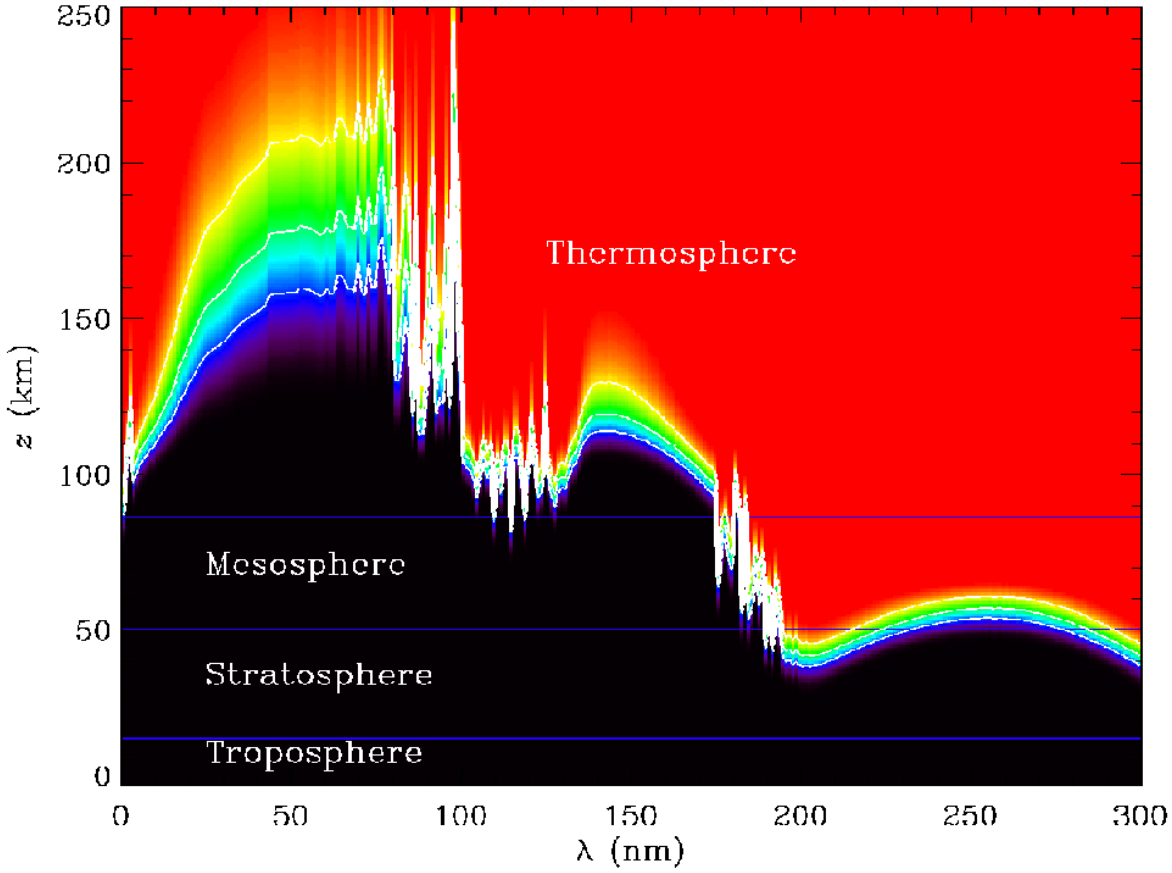

Figure 1.9: Solar irradiance is shown with the wavelength, or energy, on the horizontal axis, and the ionization altitude on the vertical axis. Figure taken from the NASA Solar Dynamics Observatory website, https://sdo.gsfc.nasa.gov/mission/science.php.

1.4.2 $F_{10.7}$ as a Solar Proxy

$F_{10.7}$ is a radio emission that comes from the sun and is a 100 MHz wide band centered at 10.7 cm (2800 MHz). These emissions come from the corona and chromosphere above active regions of the sun (Tapping, 2013). With the advent of radars during World War II many of these surplus radios were repurposed and used to study the sun. It was quickly realized that $F_{10.7}$ corresponded very well with the sunspot number (Covington, 1947).

After realizing that $F_{10.7}$ was well correlated with sunspot number it was realized that it also is a good proxy for ultraviolet and extreme ultraviolet irradiance which, as was shown in Figure 1.9, is a very importance electromagnetic band that is responsible for much of the ionization. It is such a good proxy that ionospheric modellers have used the $F_{10.7}$ parameter as an input for their models to calculate the photoionization

1.4.3 Particle Precipitation

Particles in a plasma move along magnetic field lines and if they have sufficient velocity parallel to the magnetic field, or a small enough pitch angle, they can "precipitate" into the earth's ionosphere and ionize molecules in the atmosphere. These particles can have several effects on the ionosphere ranging from beautiful aurora, to damaging radiation for airplane passengers, to localized changes in the conductivity of the ionosphere, and heating of the thermosphere/ionosphere which can slow down satellites in orbit. There are several forms of particle precipitation that depends on the type of particle, the amount of energy it has, and what process accelerated it.

The two types of particle precipitation that affect ionospheric conductivity are diffuse and discrete precipitation. Discrete precipitation often results in very well defined auroral arcs, and result from the acceleration of plasma along potential drops in magnetic field lines, thus causing discrete bands of higher conductivity in the ionosphere. Diffuse precipitation comes from pitch angle scattering of hot electrons and results in aurora that is more like a glow, and is often too dim for the human eye to perceive. The conductivity enhancements resulting from diffuse precipitation are likewise more broad.

1.4.4 Ionospheric Conductivity

The ionosphere is a conducting fluid with ions and electrons, but unlike the magnetosphere, there are many neutrals that interact with the plasma resulting in conductivity being attitudinally and directionally dependant. For the simplified case where B is only in the z direction (such as the polar regions) the ionospheric conductivity is in tensor form as shown in Equation 1.22.

$$\mathbf{j} = \begin{pmatrix} \sigma_1 & \sigma_2 & 0 \\ -\sigma_2 & \sigma_1 & 0 \\ 0 & 0 & \sigma_0 \end{pmatrix} \begin{pmatrix} E_x \\ E_y \\ E_z \end{pmatrix} \tag{1.22}$$

Two of the conductance directions have their own name, Pedersen conductance is the conductance perpendicular to the magnetic field but parallel to the electric field. Hall conductivity is perpendicular to both the magnetic and electric fields. If the electric field in Equation 1.22 is

applied perpendicular to the magnetic field then σ_1 is the Pedersen conductivity, and σ_2 is the Hall conductivity, where σ_0 is the conductivity parallel along the magnetic field line.

There are the different directions to the conductivity because as the particles descend into the ionosphere they begin to be uncoupled from the magnetic field lines due to collisions with neutral particles. The ions become uncoupled first since they have a larger gyroradius, then the electrons uncouple further into the ionosphere.

1.5 Magnetosphere-Ionosphere Coupling

To couple the ionosphere to the magnetosphere in computer simulations, the ionosphere code requires the potential electric field and the field aligned currents (FAC) to supply the particle precipitation. The magnetosphere code requires the potential at the boundary and the conductance of the ionosphere to close out the FAC. Ionospheric conductivity influences heavily the convection of the magnetospheric plasma. (Wolf, 1970; Vasyliunas, 1970; Tanaka, 2007).

1.5.1 Magnetospheric and Ionospheric Convection

Magnetospheric and ionospheric convection is important for understanding the dynamics of the magnetosphere-ionosphere (M-I) system. Figure 1.10 shows a schematic of the convection patterns during a period of southward IMF during an ideal Dungey process of magnetic reconnection and convection (Dungey, 1961). As the solar wind flows past the earth's magnetosphere, reconnection occurs on the dayside (field line 1) and flows past the polar caps (lines 2-5). After significantly stretching and still being anchored to the ionosphere, the oppositely aligned magnetic field lines are pressed together in the nightside and reconnection occurs with the stretched field lines now convecting back (lines 6-8). The field lines further convect as shown in the ionosphere around to the dayside of the magnetosphere, and the process begins again.

The footpoints of the field lines trace out a cell in the ionosphere, with anti-sunward flow over the polar cap with the plasma convecting back to the dayside along the auroral oval. The plasmas

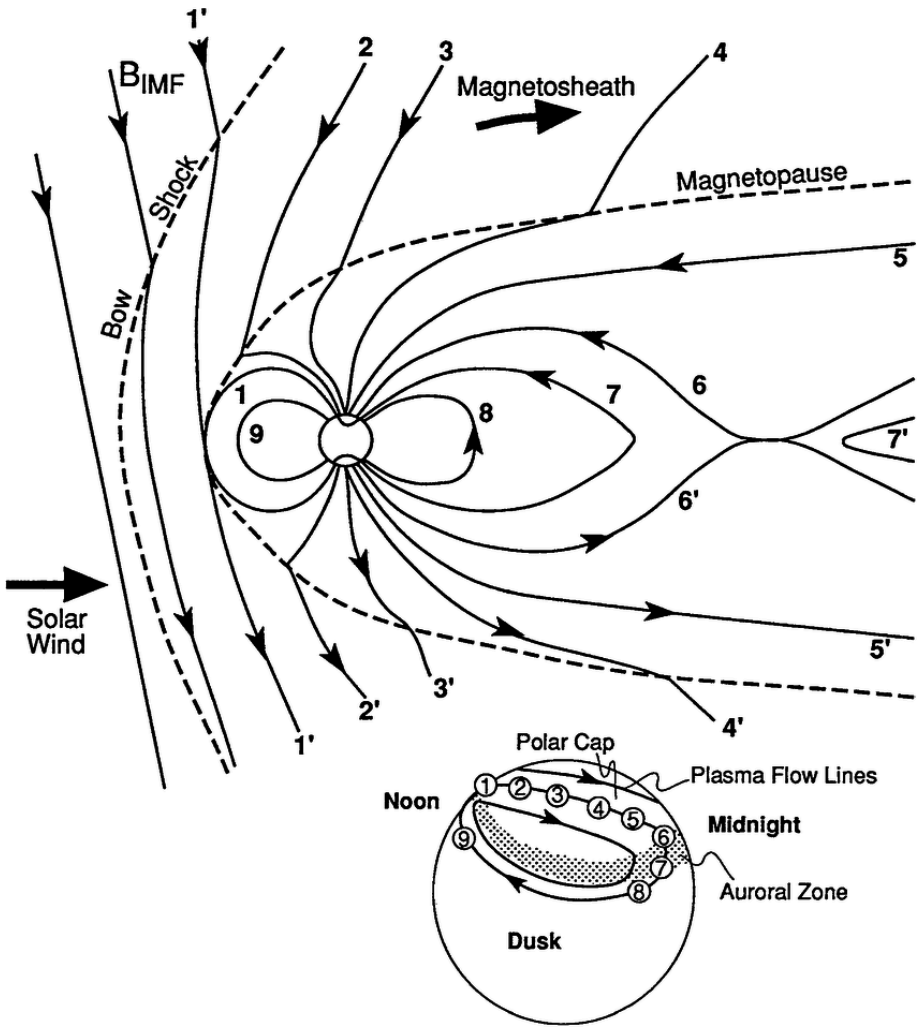

Figure 1.10: Diagram showing the convection of magnetospheric plasma in the magnetosphere, with the corresponding magnetic field footpoints in the ionosphere in the insert. Figure from Kivelson and Russell (1995).

in the magnetosphere and ionosphere behave differently due in part to the conductivity of the local plasma. At approximately 200km above the earth's surface the ionosphere is a resistive medium and currents and electric fields are related by Ohm's law for a resistive medium,

$$\mathbf{J} = \boldsymbol{\sigma} \cdot (\mathbf{E} + \mathbf{U} \times \mathbf{B}) \tag{1.23}$$

Where $\mathbf{U}$ is the velocity of the neutral winds. The plasma above 2000 km can be described using Ohm's law for a collisionless plasma,

$$\mathbf{E} = -\mathbf{v} \times \mathbf{B} \tag{1.11}$$

and momentum conservation,

$$\rho \frac{d\mathbf{v}}{\partial t} = -\nabla p + \mathbf{J} \times \mathbf{B} \tag{1.7}$$

The area between these two regions is a transition region. Electrical coupling between the lower ionosphere and the upper ionosphere/lower magnetosphere is governed by current continuity,

$$\nabla \cdot \mathbf{J} = 0 \tag{1.24}$$

and Faradays law,

$$\frac{\partial \mathbf{B}}{\partial t} = -\nabla \times \mathbf{E} \tag{1.9}$$

Assuming a simple southward IMF, using Ohm's law the imposed electric field can be determined. The electric field points from dawn to dusk on the northern hemisphere. The dawn dusk electric field (E_{SW}) is mapped along magnetic field lines into the ionosphere. This results in an imposed electric field in the ionosphere over the polar cap (E_{PC}) as shown in figure 1.11. The assumption that the field lines are considered electrostatic equipotentials is considered a good approximation for most field lines except those on auroral field lines where there is an accelerating potential that cause particles to precipitate (Kelly, 2009).

Figure 1.11 shows the idealized convection cells in the ionosphere during B_z south magnetic field. E_{PC} results from the impingement of the solar wind electric field, the other E fields on the duskside and dawnside result from Ohm's law with a magnetic field into the earth. The plasma convection in the polar regions are described by $\mathbf{E} = \mathbf{v} \times \mathbf{B}$.

Figure 1.12 shows convection patterns in the ionosphere during periods of strong northward IMF. The high latitude open polar cap region shows convective patterns that are consistent with reconnection occurring poleward of the cusp, but the lower latitude cells are from viscous interactions which are primarily driven from solar wind velocity and density, but ionospheric conductivity does play a role as well.

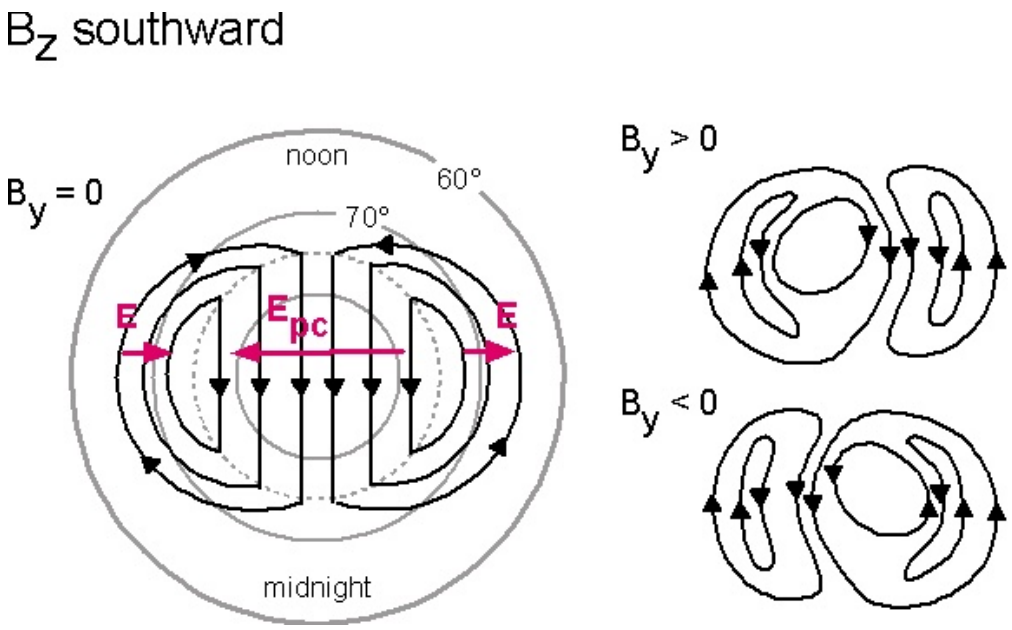

Figure 1.11: Idealized convection for the northern hemisphere during IMF B_z negative. Changes in B_y also factor into the convection. Figure is from https://wiki.oulu.fi/display/SpaceWiki/Ionospheric+convection.

1.5.2 The Role of Field Aligned Currents

Field aligned currents play an important role in connecting the ionospheric and magnetospheric regions electrically. To show how they are generated in the magnetosphere, Ohm's law and momentum conservation are written as,

$$\nabla \cdot \mathbf{J}_\perp = -\rho \frac{d}{dt}\left(\frac{\Omega}{\mathbf{B}}\right) - \frac{\mathbf{J}_\perp \cdot \nabla \mathbf{B}}{B^2} + \frac{\mathbf{J}_{in} \cdot \nabla n}{n} \tag{1.25}$$

where,

$$\Omega = B \cdot \nabla \times \frac{\mathbf{v}}{B} \qquad \text{(Vorticity)} \tag{1.26}$$

$$\mathbf{J}_{in} = \mathbf{B} \times \left(\frac{\rho}{B^2}\frac{d\mathbf{v}}{dt}\right) \qquad \text{(Inertia Current)} \tag{1.27}$$

and $\mathbf{J}_\perp$ is the current perpendicular to the magnetic field. Equation 1.25 can be rewritten using coordinates along the magnetic field line to calculate the intensity of the FAC following Sato and

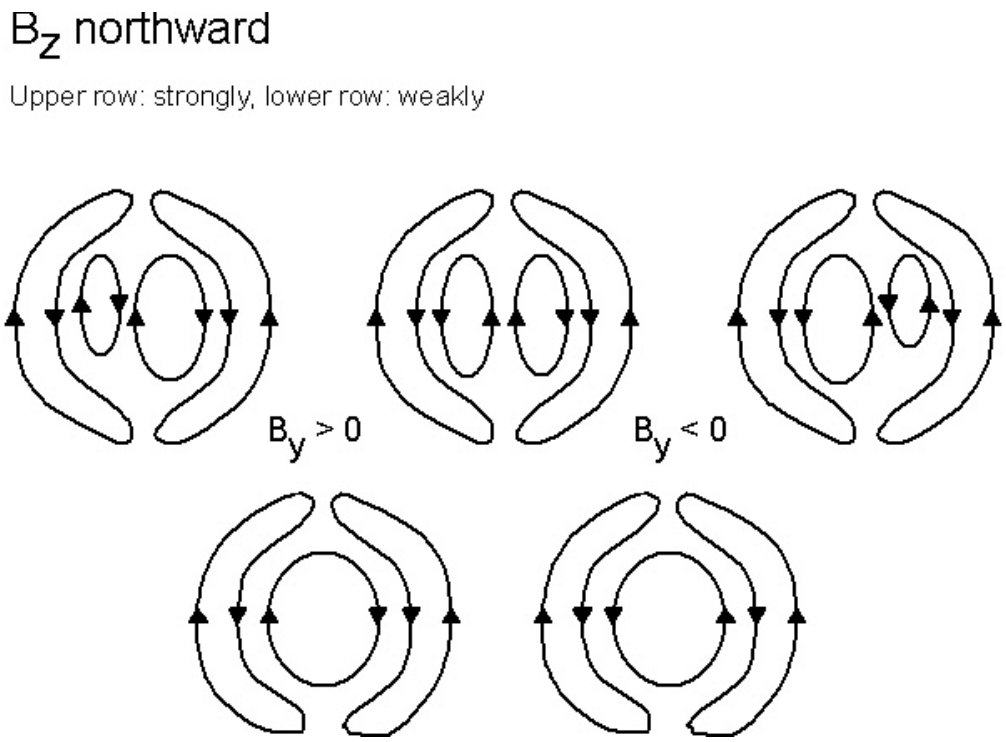

Figure 1.12: Idealized convection cell patterns for IMF B_z positive, with varying B_y. The upper row if for strong positive B_z, Lower row is for weaker B_z. This is from https://wiki.oulu.fi/display/SpaceWiki/Ionospheric+convection.

Iijima (1979) which results in,

$$J_{||I} = B_I \int_0^l \left[\frac{\rho}{B} \frac{d}{dt} \frac{\Omega}{B} + \frac{1}{B^2} \mathbf{J}_\perp \cdot \nabla B - \frac{1}{nB} \mathbf{J}_{in} \cdot \nabla n \right] ds \tag{1.28}$$

where the subscript I denotes the value at the iononspheric height and the integration is from the base of the ionosphere along the magnetic field line to the magnetic equator.

The three terms in the integrand of Equation 1.28 show the generation mechanisms for FAC. The first term in the integrand comes from convection cells in the magnetosphere. These FAC deposit energy in the ionosphere through Ohmic heating and the amount of energy deposited is dependent on the process generating the convection. If it is a vortex caused by an earthward flowing bursty bulk flow (BBF), the energy input will be short lived because BBFs are a transient process, and Ohmic dissipation will remove energy from the vortex.

If the FAC is a result of viscous interaction at the magnetopause boundary, as long as the solar wind supplies energy to the convection cells in the magnetosphere, the FAC will continue to dissipate energy into the ionosphere. FAC of this type are heavily dependent on the mechanism generating the vorticity, and also on the conductivity of the ionosphere, because the energy deposition occurs through moving the plasma through the ionosphere.

The second term in the integrand of Equation 1.28 shows FAC generation if gradients in the magnetic field are present in the direction of the total magnetospheric current. These FAC are entirely dependent on the spatial structure of the magnetosphere and are not dependent on the time variation, and are independent of the condition of the ionosphere (but still can influence it). The third term originates from density inhomogeneities in the direction of the inertia current and can be associated with cusp FAC (Sato and Iijima, 1979).

Figure 1.13 shows the placement of FAC in the ionosphere (Iijima and Potemra, 1976). It is still unclear the exact mechanism for region 1 current generation, as region 1 currents have been found on both open and closed field lines. For open field lines region 1 current generation has been attributed to reconnection and subsequent driving by solar wind, while on closed field lines viscous processes or the substorm current wedge can contribute to region 1 currents (Ganushkina et al., 2015). Region 2 currents are produced by current closure of the ring current.

1.5.3 Cross Polar Cap Potential

A very useful metric for understanding the coupling between the ionosphere and the magnetosphere is called the cross polar cap potential (CPCP). This is a measure of the difference between the maximum and minimum potential observed in the ionosphere $CPCP = V_{max} - V_{min}$. This is a difficult metric to observe because there should ideally be full coverage of the entire polar cap to find the true max and min. Satellite passes are difficult because it is not known if the satellite passed through the actual max or min. Efforts from ground based radar, such as the SuperDARN radars are very useful as they cover most of the polar cap, except the Russian sector. Modelling is used to fill in many of these gaps but there are limitations that come from modelling as well.

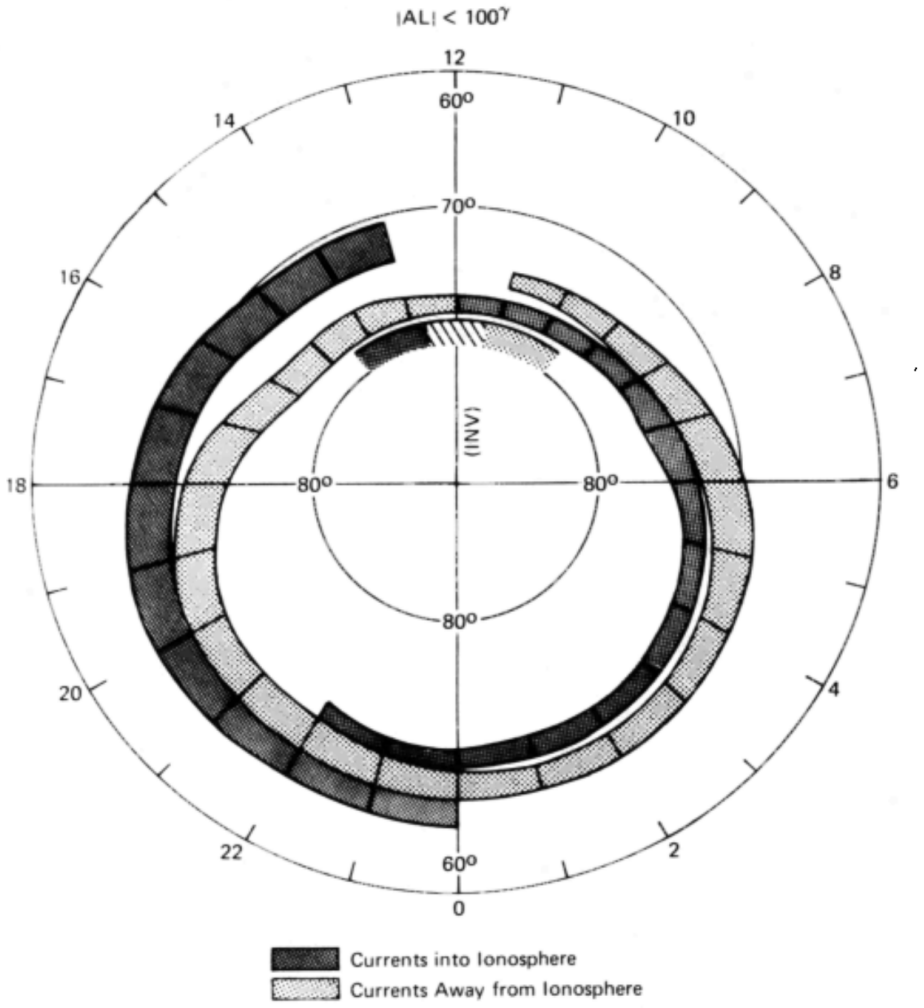

Figure 1.13: Region 1 currents are poleward, region 2 currents are equatorward, with cusp currents poleward at the noon meridian. Figure from Iijima and Potemra (1976).

There are more systematic possibilities such as using constellations of satellites to approximate the CPCP such as the effort with AMIE (Richmond and Kamide, 1988; Richmond et al., 1998) using the Iridium satellite constellation coupled with ground based measurements.

Despite the difficulties that come with identifying the CPCP, it is a valuable parameter and many trends have been identified. Many empirical relationships have been developed to try and predict the CPCP using a multitude of parameters. Table 1.1 is a general table identifying some of the parameters that can cause CPCP to increase or decrease. See Shepherd (2007) and Borovsky et al. (2009) for a good summary of many empirical relations used to find the value of CPCP.

As these parameters increase	
solar wind velocity, reconnection electric field, strength of magnetic field, southward magnetic field, length of reconnection line, and solar wind ram pressure	CPCP increases
Pedersen conductivity	CPCP decreases

Table 1.1: Brief summary of the parameters thought to influence the CPCP

The CPCP tends to increase linearly for certain values of the solar wind parameters, but after reaching a larger value, the linear increase of the CPCP tends to saturate. There are many theories for how the CPCP saturates, Borovsky et al. (2009) has compared many of them. CPCP is assumed an indicator of the magnetic reconnection in the magnetosphere, but there are some difficulties with this assumption. It is very difficult to measure CPCP from observation, but it is orders of magnitude more difficult to measure reconnection for the whole magnetosphere. Comparing the validity of this assumption with computer simulations is addressed further in this work in chapter 2.

1.5.4 The Ionosphere as a Plasma Source for the Magnetosphere

Particles are escaping from the ionosphere constantly, especially along open magnetic field lines. There are many mechanisms that explain how particles leave the ionosphere, but the relative contributions of each, and which mechanisms are dominant in which regions is still an open question. Some outflow originates from the nightside aurora since the mechanisms that can accelerate the electrons into the ionosphere can also accelerate ions out of the ionosphere. There is also significant outflow from the cusp regions of the earth. The particles that are accelerated and overcome the escape velocity of the earth flow along flux tubes in the magnetosphere. Many satellites have found high concentrations of plasma in the magnetosphere that originated from the earth (Hamilton et al., 1988; Kistler et al., 2016; Allen et al., 2017).

The upper atmosphere has a high O^+ and H^+ concentration and these ion are the main constituents of ion outflow. The effect H^+ on reconnection is not as large as the more massive O^+. The

mass of the particles plays a role in the reconnection rate as shown in the reconnection Equation 1.19,

$$M_{Ae} = \frac{\pi}{8} \ln(\frac{L_e V_{Ae}}{\eta})^{-1} \tag{1.19}$$

where L_e is the length scale, V_{Ae} is the Alfvén velocity, and ζ is the magnetic diffusivity of the plasma. The Alfvén velocity is one of the dependencies of reconnection and Alfvén velocity is given by $V_{Ae} = B/(\mu_0 \rho)^{1/2}$. A change in the density of the plasma will have an effect on the reconnection by increasing the mass of the particles in the reconnection region. The plasma density has a significant influence on the Alfvén velocity, which is an important parameter in reconnection rates. Ion outflow has been shown in simulations to have an affect on reconnection rate (Winglee, 2004; Zhang et al., 2016), but it is difficult to measure reconnection rates observationally to verify the effect.

Ion outflow effects on M-I coupling is beyond the scope of this work. OpenGGCM is in the process of becoming a multi-fluid code (Wang et al., 2015).

1.6 OpenGGCM-CTIM-RCM

The OpenGGCM-CTIM-RCM model (Raeder, 2003; Raeder et al., 2008; Fuller-Rowell et al., 1996; Toffoletto et al., 2003) is used to solve the magnetohydrodynamic equations on a stretched Cartesian grid over the entire simulation box. The program has it's origins with Joachim Reader while he was at UCLA and has been in active development for over 20 years.

1.6.1 MHD Numerics

To solve the MHD equations for the earth's magnetosphere there is a need to discretize both in space and time. Time discretization is fairly straightforward using an explicit second-order predictor-corrector finite differencing scheme. One thing to understand in time discretization is

that the Courant-Fredrichs-Levey(CFL)(Sod, 1985) criterion states that the time step $\Delta t \leq \Delta t_{max}$ where t_{max} is given by,

$$\Delta t_{max} \;\leq\; \delta \frac{\min(\Delta x, \Delta y, \Delta z)}{|\mathbf{v}| + v_{MS}} \tag{1.29}$$

This is problematic because if the Alfvén speed is high in just a few places, then the stable time step becomes very small over the whole magnetosphere. If the time step is too small the simulation takes up too much computer time. To get past this OpenGGCM uses the Boris correction (Boris, 1970; Brecht, 1985) that limits the $\mathbf{J} \times \mathbf{B}$ and $\nabla p_{\perp}$ in locations where the Alfvén speed would be too high.

To discretize the spatial derivatives in the MHD equations is more difficult. We use a finite difference method to discretize spatially, but since the flows in the magnetosphere vary significantly, OpenGGCM uses a hybrid scheme first proposed by Harten and Zwas (1972), a fourth order scheme with a minimal diffusion error (Zalesak, 1979) for the smooth gradient areas of the simulation. For the large gradient areas the first order Rusanov scheme is used. These schemes were chosen so that the variables are globally conserved. It is inherent in the numerics that these variables are conserved.

In order to maintain $\nabla \cdot \mathbf{B} = 0$ the electric and magnetic fields are calculated on a staggered grid, proposed first by Evans and Hawley (1988) and shown in Figure 1.14. Magnetic flux in conserved *a priori* by moving the electric field calculation to the center of the edges of the grid cell, and magnetic field calculation to the center of the cell faces.

1.6.2 Simulation Grid and Initial Conditions

There are many possible grid systems that could be chosen, but OpenGGCM uses a stretched Cartesian grid, as shown in Figure 1.15. Stretched Cartesian grids are used because the code is straightforward and the load balancing for parallelization is simpler than most grids, but high resolution is still preserved for locations of interest (i.e the dayside magnetopause). The earth is at

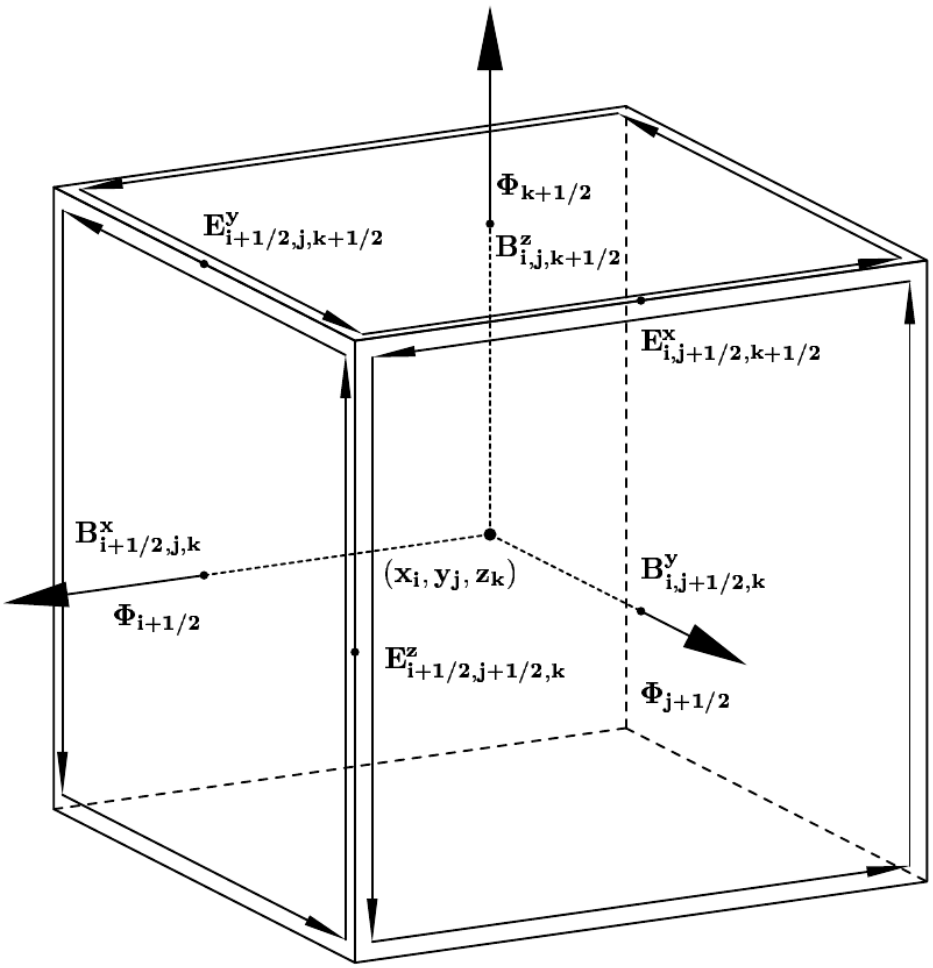

Figure 1.14: Grid cell layout of the electric and magnetic fields, this figure is taken from Evans and Hawley (1988).

the origin, and the MHD grid covers the simulation box except within a 3 R_E sphere originating with the earth, where dipole field lines are mapped to the MHD inner boundary.

The initial conditions for the simulation is a mirror dipole with $B_x = 0$ on the sunward simulation boundary. The initial plasma conditions are a cold (5000° K) tenuous (0.1 cm^3) plasma populating the magnetosphere. The solar wind enters from the sunward boundary, and the magnetosphere forms, but it takes a few hours to initialize and have magnetosphere fully formed.

Solar wind data is used from either of two NASA satellites orbiting at the Lagrange 1 point (L1), Wind or the Advanced Composition Explorer (ACE). We also use solar wind data from the OMNI repository that extends the solar wind data from L1 to the nose of the magnetopause. The

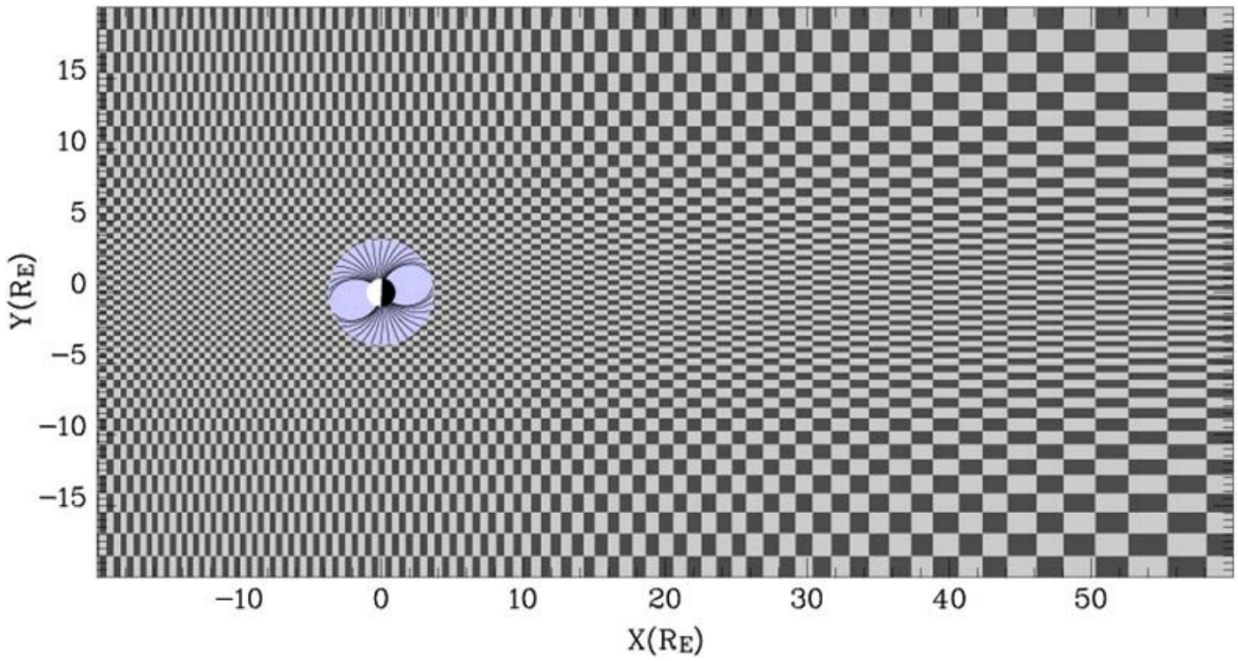

Figure 1.15: Stretched Cartesian grid that OpenGGCM uses. Most simulations use a resolution that is much higher than shown here. This figure is taken from Raeder et al. (2008).

solar wind flows from the sunward boundary, but in order to preserve $\nabla \cdot \mathbf{B} = 0$ B_x must remain the same as it propagates through the system. This difficulty can be minimized using the minimum variance method that finds the normal vector of the solar wind and uses it to propagate through the domain (Sonnerup and Cahill, 1967, 1968). For all the other outer boundaries of the MHD domain free flow conditions are applied.

1.6.3 CTIM and RCM Models

The Rice Convection Model (RCM) (Toffoletto et al., 2003) is a ring current model that determines quasi-static plasma flow due to ionospheric potential, magnetic gradient drift, and curvature drift. While the stand-alone RCM computes field aligned currents and precipitation to obtain the self-consistent ionosphere potential, when coupled with OpenGGCM, RCM does not directly pass FAC and precipitation information to the ionospheric model. Instead, it's pressure is fed back to the MHD solver, which creates a more realistic inner magnetosphere. This results in better precipitation patterns and FAC. Ninety minutes after OpenGGCM starts, the RCM takes the interpolated

pressure and densities and initializes its 2-D grid. Once the RCM has initialized it feeds the pressure and density back to the 3-D MHD grid, by tracing along field lines and interpolating the data to the 3-D grid. The OpenGGCM-RCM coupling is described in more detail by Cramer et al. (2017).

The Coupled Thermosphere Ionosphere Model (CTIM) (Fuller-Rowell et al., 1996) is an ionosphere-thermosphere model that calculates conductivities and sends it to the potential solver module. The potential solver then calculates the potential, and provides it to all three models. CTIM uses the potential, total energy flux, and the mean energy of the precipitating electrons as input from OpenGGCM, and calculates the Pedersen and Hall conductances self-consistently from the electron density, neutral density, and collision rates as described in Raeder et al. (2001a) and Raeder et al. (2001b). The height integrated conductivities, i.e., the conductances, are sent to the potential solver. The MHD and the RCM models use the resultant potential for their lower boundaries, thereby closing the convection cycle. For further references on how the models are coupled, see Raeder et al. (2016) and Cramer et al. (2017).

1.6.4 Inner Boundary

The potential and FAC must be determined on the inner boundary of the magnetosphere and upper boudnary of the ionosphere. The MHD/RCM portion extends down to 2 R_E from earth's surface, and the top of the CTIM model extends to about 600 km (.1 R_E) above the surface. The area between the boundaryies is the transition region, extending from 600km to 2 R_E. The potential and FAC are mapped along the dipole field of the earth, and solve the potential equation presented by Vasyliunas (1970),

$$\nabla \cdot \mathbf{\Sigma} \cdot \nabla \Phi = -j_{||} \sin(I) \tag{1.30}$$

Where Φ is the potential, $j_{||}$ is the FAC density, I is the magnetic field inclination angle, and Σ is the conductivity tensor. This equation is related to Equation 1.22, then the Σ can be given by,

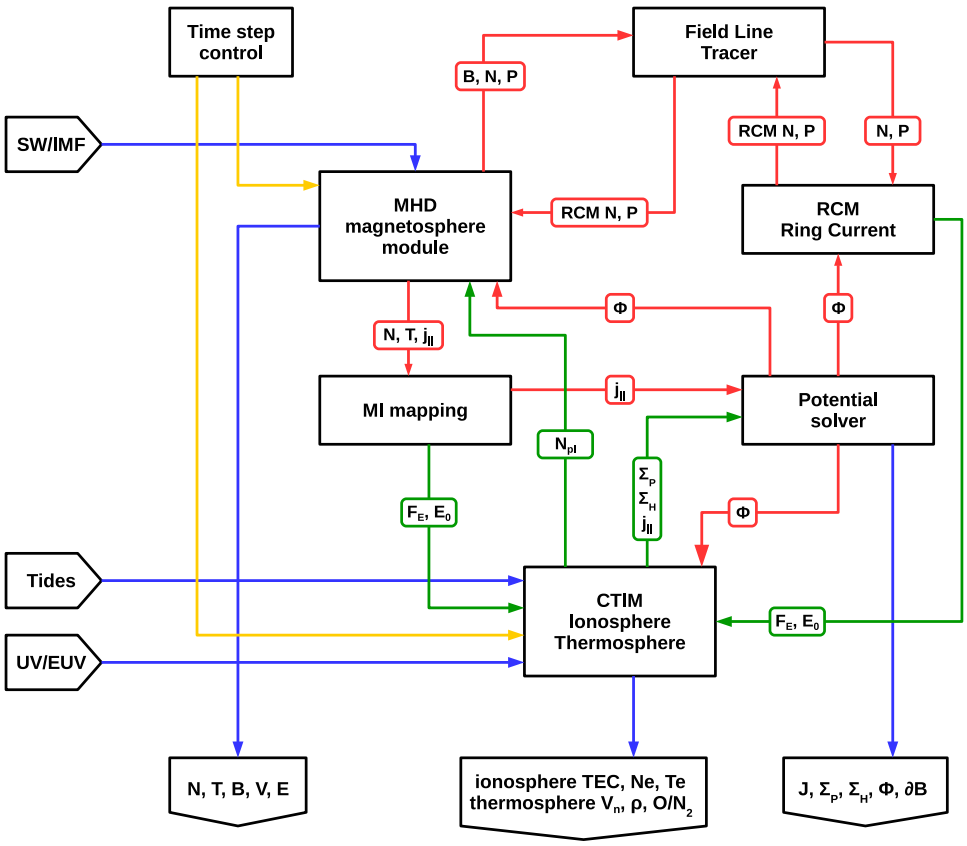

Figure 1.16: Map shows how OpenGGCM, CTIM and RCM are coupled. The lines are colored to show different types of data flow. Blue is input/output, red is data strongly coupled, green is weakly coupled data, and yellow is the control time step. The variables B, N, V, T, and E are magnetic field, plasma density, plasma velocity, temperature, and electric field, respectively. ϕ, $j_{||}$, Σ_H, and Σ_P, are the ionosphere potential, parallel current, and Hall and Pedersen conductances, respectively. F_E and E_o are the energy flux and mean energy of precipitating electrons. (Figure taken from Cramer et al. (2017)).

$$\Sigma = \begin{pmatrix} \Sigma_{\theta\theta} & \Sigma_{\theta\lambda} \\ -\Sigma_{\theta\lambda} & \Sigma_{\lambda\lambda} \end{pmatrix} \tag{1.31}$$

where,

$$\Sigma_{\theta\theta} = \frac{\Sigma_P}{\sin^2 I}, \qquad \Sigma_{\theta\lambda} = \frac{\Sigma_H}{\sin I}, \quad \text{and} \quad \Sigma_{\lambda\lambda} = \Sigma_p \tag{1.32}$$

with θ the magnetic latitude, and λ the magnetic longitude (Kelly, 2009). The potential is used to calculate the field and flow integration at the inner boundary of the magnetosphere.

$$\mathbf{v} = (-\nabla\Phi) \times \frac{\mathbf{B}}{|B|^2} \tag{1.33}$$

Because electron precipitation plays a central role in M-I coupling across the boundary, how OpenGGCM calculates the precipitation energy flux F_E and the mean energy E_0 will be explained in detail. There are two kinds of precipitation calculated in OpenGGCM, diffuse and discrete precipitation. Diffuse precipitation is assumed to be caused by pitch angle scattering of hot magnetospheric electrons, assuming a full loss cone, and is parametrized by,

$$E_o = kT_e \tag{1.34}$$

$$F_E = \alpha n_e (kT_e/2\pi m_e)^{1/2}. \tag{1.35}$$

T_e and n_e are the electron temperature and density respectively, E_o is the mean energy, and F_E is the energy flux of the precipitating electrons (Kennel and Petschek, 1966). Temperature is calculated using the MHD ion temperature and using the ratio $T_i/T_e = 7.8$ for inner plasma sheet electrons (Baumjohann et al., 1989). The n_e comes from the density calculated from the MHD equations and assumes a full loss cone. The variable α is introduced in the scaling study so the energy flux of the precipitation can be modified. Scaling the α can be seen physically as changing the number density of both the diffuse and discrete precipitating electrons.

Discrete precipitation comes from accelerated auroral electrons due to parallel potential drops along the magnetic field lines; it is parametrized by the Knight (1973) relation,

$$E_o = e\Delta\Phi_\parallel \tag{1.36}$$

$$F_E = \alpha\Delta\Phi_\parallel J_\parallel \tag{1.37}$$

$$\Delta\Phi_\parallel = e^2 n_e/\sqrt{2\pi m_e k T_e}\ \ \max(0, -J_\parallel) \tag{1.38}$$

where $\Delta\Phi_\parallel$ is the parallel potential drop of the magnetic field line, and $J_\parallel$ is the FAC density. For further references on how OpneGGCM works please see the following references (Cramer et al., 2017; Ferdousi, 2017; Raeder et al., 2016; Kavosi, 2015; Oliveira, 2015).

CHAPTER 2

PRECIPITATION EFFECTS ON THE MAGNETOSPHERE

2.1 Background Work

This chapter includes much of my work that has already been published in the Journal of Geophysical Research: Space Physics (Jensen et al., 2017).

The solar wind-magnetosphere-ionosphere (S-M-I) system is very complex, and each element is influenced by the others. Variations of the ionospheric conductance are important for current closure in the ionosphere, and are believed to have an effect on magnetospheric convection (Wolf, 1970; Coroniti and Kennel, 1973; Tanaka, 2007; Borovsky et al., 2009; Lotko et al., 2014).

It is well known that precipitation has a direct effect on conductance in the ionosphere (Robinson et al., 1987), and that conductance regulates magnetospheric convection. Raeder et al. (1996) showed the importance of conductance in controlling the occurrence of substorms. When Hall and Pedersen conductance was increased to 50 Siemens over the whole polar ionosphere, the magnetospheric convection, and thus the magnetic field lines were frozen into the ionosphere, preventing substorms from developing. Ridley et al. (2004) showed that conductivity influences the plasma pressure in the inner magnetosphere and causes asymmetries in the potential for both north-south and dayside-nightside geometries. Merkin et al. (2005) showed that the conductance of the ionosphere plays an important part in magnetosphere geometry, they found that for larger ionospheric conductance, the flanks of the magnetopause widen. They also found that for high conductances the cross polar cap potential tends to saturate.

Borovsky et al. (2009) did a similar study to that of Merkin et al. (2005) of conductance effects on the magnetosphere. They ran two simulations using the Block-Adaptive-Tree Solarwind Roe Upwind Scheme (BATS-R-US) with Pedersen conductance set at 5 mho and 20 mho over the entire

polar ionosphere. Hall conductance was set to zero and the simulation used constant solar wind parameters for a steady state magnetosphere. They analyzed the effects on the magnetosphere, and found, among other things, that as the Pedersen conductance increases, the cross-polar cap potential (CPCP) decreases, and the magnetopause nose moves inward. They also claimed, using the Cassak-Shay reconnection formulation (Cassak and Shay, 2007), that the reconnection rate on the dayside was unchanged by increases in the Pedersen conductance.

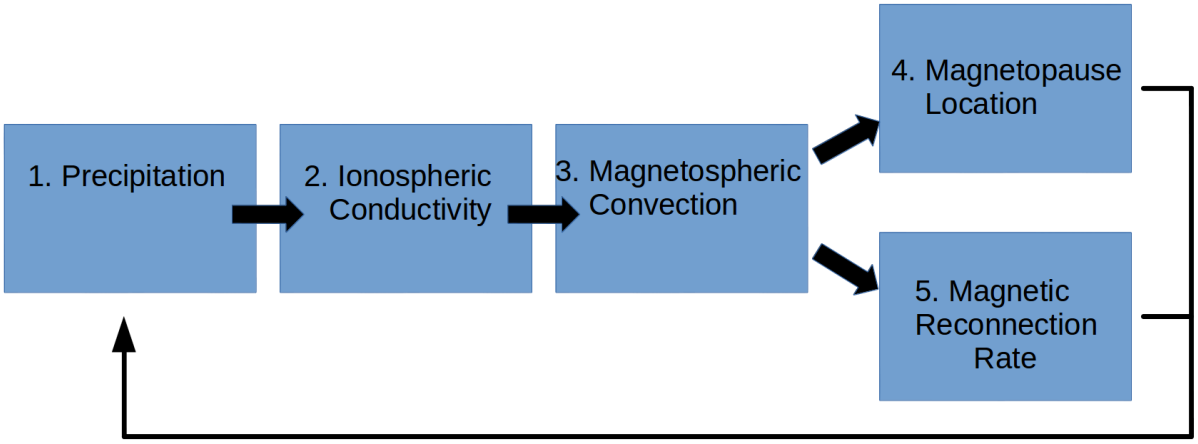

Figure 2.1: Shows the path whereby particle precipitation influences the magnetopause location and reconnection rate.

In this study the magnetopause location and magnetic reconnection rate dependence on particle precipitation is studied. Figure 2.1 shows how precipitation ultimately affects the magnetopause location and the reconnection rates. However, as the magnetosphere changes it also influences the precipitation, which results in a two way feedback that is captured in the model. Previous studies directly modified conductance of the whole ionosphere either uniformly (Raeder et al., 1996; Merkin et al., 2005; Borovsky et al., 2009), or by including an empirical relation (Ridley et al., 2004; Lotko et al., 2014). The simulations and results shown in this paper are thus unique in that the precipitation is changed. Changes to precipitation may happen in nature by various processes, for example due to different plasma sheet conditions, i.e., a cold dense plasma sheet versus a hot tenuous plasma sheet.

There are many contributing factors affecting the magnetopause location and reconnection rate, such as the force balance of the Earth's magnetic field and the solar wind plasma pressure. Additionally, the reconnection rate depends on the magnetic and electric fields and the Alfvén velocity at the reconnection location. While precipitation may not be the primary driver of determining the magnetopause location and of the reconnection rate, it has a significant influence on the dynamics of the system.

2.1.1 Simulation Setup

The OpenGGCM sunward boundary of the simulation is at 35 Earth radii (R_E) and the tail of the magnetospheric box is at 5000 R_E. The MHD simulation box extends out to 48 R_E in both the Y and Z directions. The grid spacing for the simulations has resolution along the X axis ranging from 0.17 R_e near the earth, to 100's of R_e in the distant tail, and 0.25-1.35 R_e in the Y and Z directions.

2.1.2 Event Selection

In order to cover different geophysical conditions, i.e., different levels of geomagnetic activity, two events were selected, one with average solar wind conditions (May 4, 2005), and one with storm-like conditions (March 17, 2013). Figure 2.2 shows the solar wind data from the Advanced Composition Explorer (ACE) satellite for the May 4, 2005 event. This day has a B_z magnitude no more than 3 nT, but the B_z component does change sign a few times. The solar wind velocity for this event is on average 400 km/s and the density of the solar wind stays around 2-4 particles/cm^3.

To simplify the simulations, the OpenGGCM version used in this study has a fixed dipole that does not rotate, but is set at a specific UT time for the duration of the simulation (Raeder et al., 2008). A fixed dipole introduces some error mostly at times when examining 12 hours before or after the fixed dipole time. However, since the objective of this work is to analyze effects due to changing precipitation, as opposed to accurately replicate observations, this is justified. A fixed dipole time of 12:00 UT on May 4, 2005 was selected.

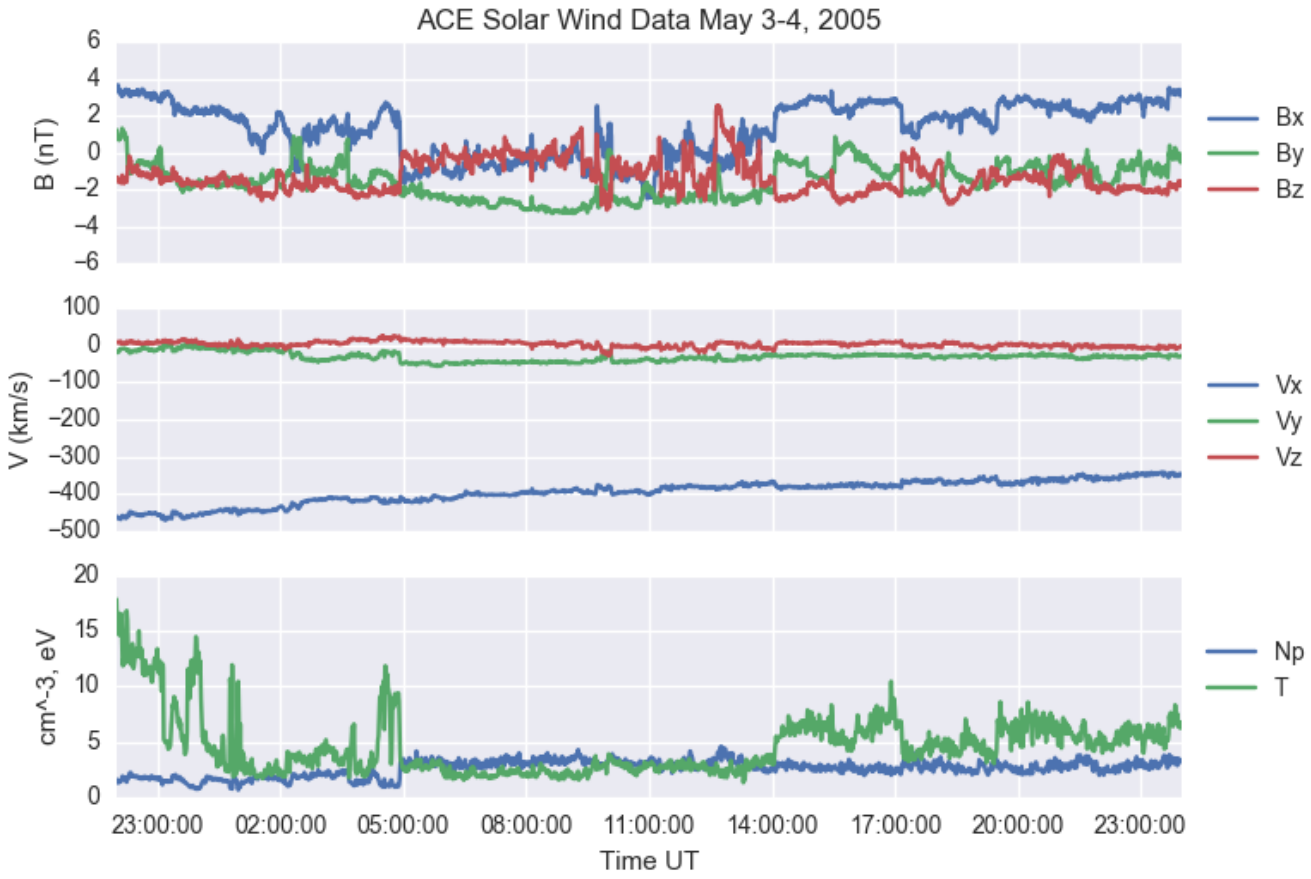

Figure 2.2: The solar wind data for May 4, 2005 taken from the ACE satellite. The top panel shows the 3 components of the magnetic field, the middle panel shows the 3 component solar wind velocity, and the bottom panel shows the number of particles and the average temperature (in eV). The x axis is the Universal Time (UT) that starts on May 3, 2005 at 2300 UT and contains all of May 4th.

Figure 2.3 shows the solar wind conditions for the March 17, 2013 storm event, also known as the 2013 St. Patrick's day storm. A coronal mass ejection arrives at about 0530 UT. The magnetic field is in the 10-15 nT range, and there are multiple B_z sign changes. The solar wind velocity is also higher at 600-700 km/s with the densities around 10 particles/cm^3. A fixed dipole time of 2130 UT was selected for this simulation.

2.1.3 Varying Precipitation

For both events, four different precipitation conditions are simulated. First is a control simulation where $\alpha = 1$ in equations 1.34 through 1.37. For the other simulations, α is set to 0.01, 0.1,

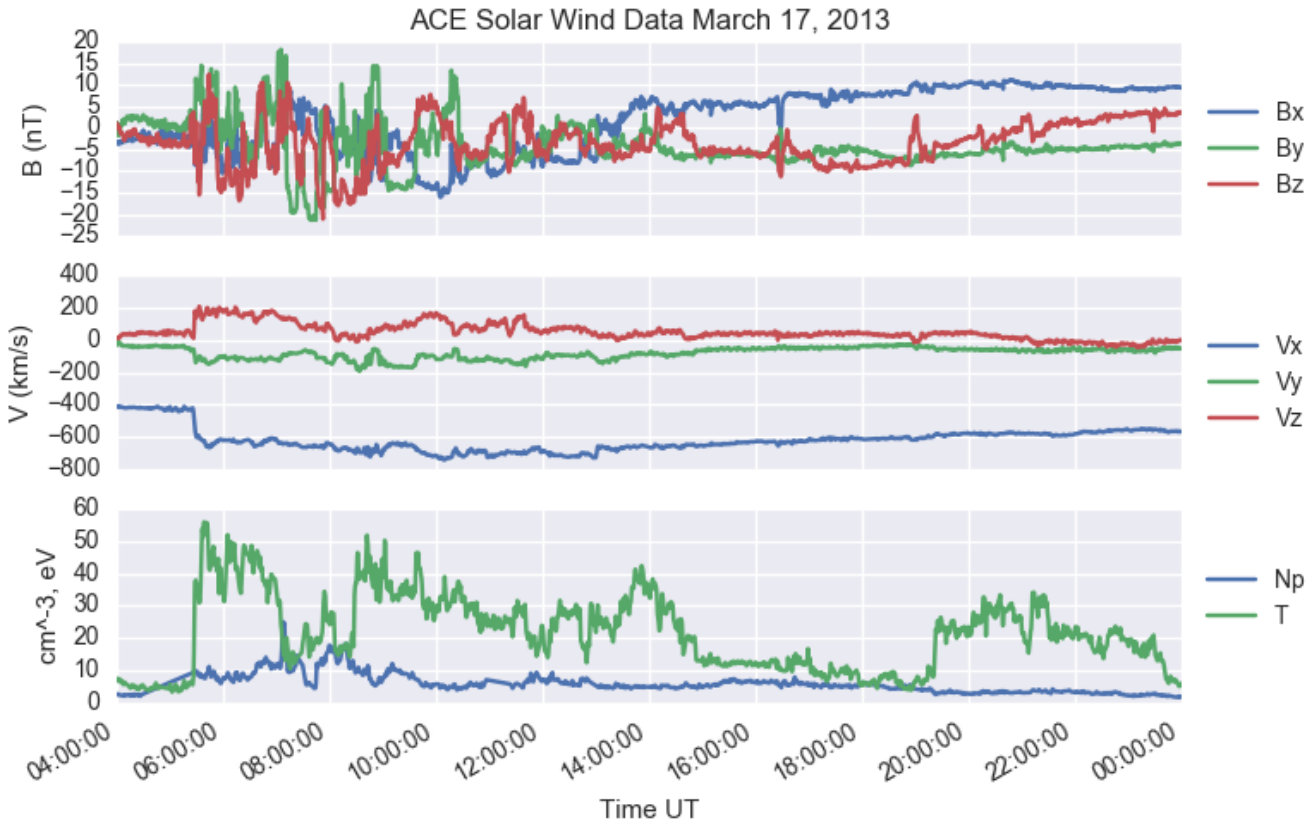

Figure 2.3: The solar wind data for March 17, 2013. This data is taken from the ACE satellite, and is in the same format as Figure 2.2. There is a CME that hits the satellite at 0530 UT.

and 10, respectively. The range of precipitation for each of these simulations varies from almost no precipitation to intense precipitation, with the mean energy remaining constant. The other drivers of the simulation, such as the solar wind input, are identical for all four runs. Each simulation is hereafter designated as the $\alpha = 0.01$, $\alpha = 0.1$, $\alpha = 1$, and $\alpha = 10$ simulation.

Figure 2.4 shows the precipitation into the ionosphere with the different modifications for the four values of α for one period of time in the simulation, March 17, 2013, 0900 UT. Both energy flux (left column) and Pedersen conductivity (right column) are graphed for all four α. If the precipitation played no role in the dynamics of the S-M-I system the patterns should be identical except for the scaling by the precipitation factors.

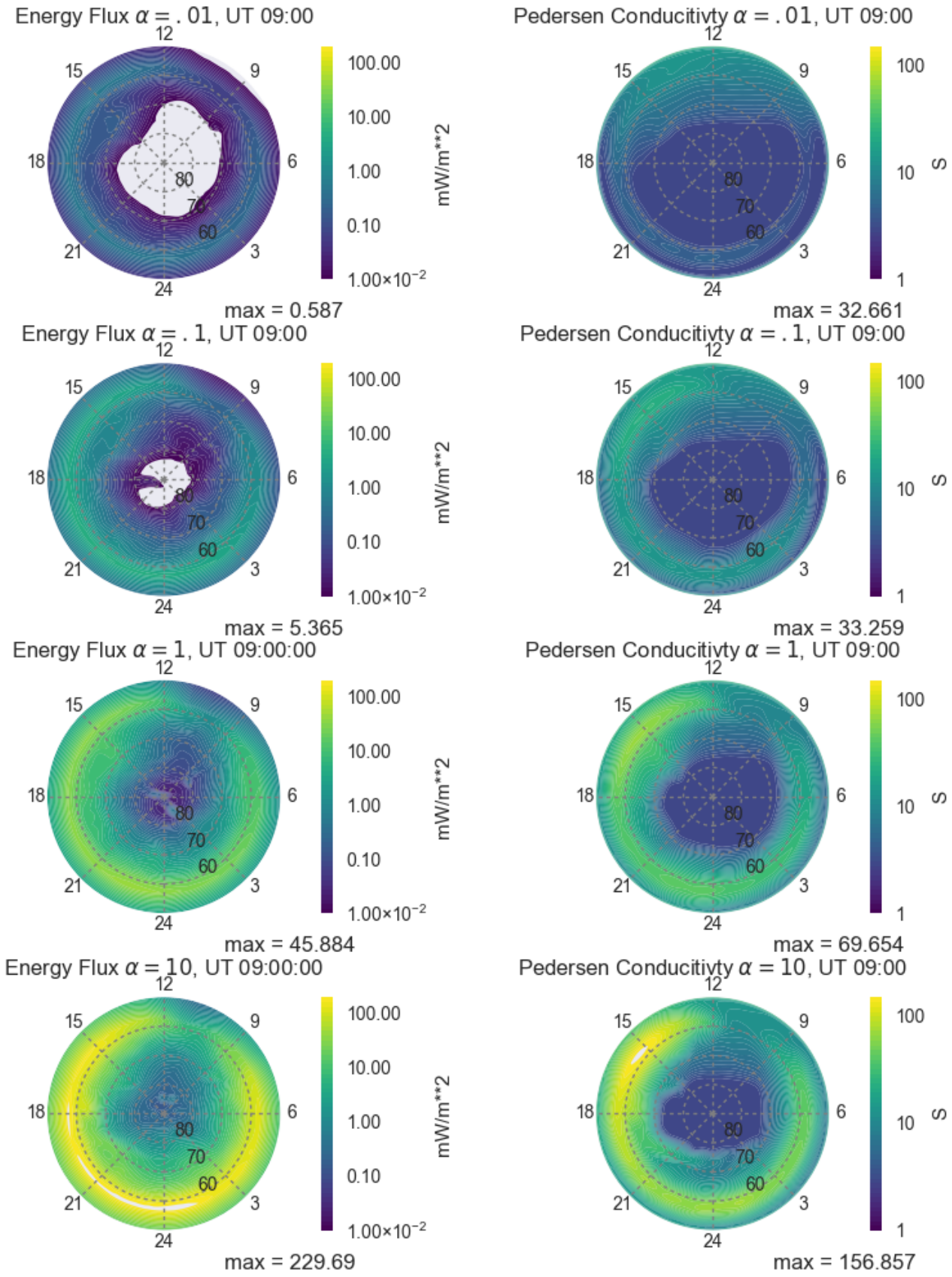

Figure 2.4: Graph of the precipitation from top to bottom for α = 0.01, 0.1, 1, and 10 for the northern hemisphere, at 0900 UT March 17, 2013. The total energy flux is shown in the left column, the Pedersen conductivity is shown in the right column.

The precipitation distribution and the conductivity patterns are different due to the feedback mechanisms. The distribution of the precipitation has significant dayside impacts to energy flux and conductivity.

The simulations for the May 4, 2005 case are modified by the same precipitation factors and show similar qualitative behavior. However, since it is a calm day the differences in precipitation and conductivity are less pronounced.

2.2 Cross Polar Cap Potential

The CPCP is an indicator of both the electromagnetic and plasma conditions in the polar cap regions. Figures 2.5 and 2.6 show the CPCP, and the effect of precipitation on the polar cap region. All other drivers of the CPCP are identical in each simulation except for the precipitation scaling factor. The four different cases show that a higher rate of precipitation in the polar caps reduces the CPCP. This result agrees with previous studies showing that an increase of conductivity reduces the CPCP (Fedder and Lyon, 1987; Ridley et al., 2004; Merkin et al., 2005; Borovsky et al., 2009). Another aspect of this trend could also be due to CPCP saturation which is dependent on the conductivity of the ionosphere. As the ionospheric conductivity is increased, the value at which the polar cap becomes saturated decreases, thus leading to the trend shown in the simulations. (Siscoe et al., 2002, 2004; Raeder and Lu, 2005; Shepherd, 2007).

The CPCP for May 4, 2005 event is shown in Figure 2.5. The CPCP for the $\alpha = 10$ case is much less than the other cases $\alpha = 0.01, 0.1, 1$, less than half during some periods. On the other hand, the decrease in the precipitation by a factor of 0.1 or 0.01 does not have as large of an effect on the CPCP during quiet times, because the percentage of ionospheric conductivity attributed to particle precipitation is small to begin with when compared to conductivity caused by photoionization. Thus reducing the already low precipitation has a small impact on the system.

There is a large hemispheric asymmetry during most of the simulation. The event date is close to the summer solstice and thus the northern hemisphere is more sunlit than the southern

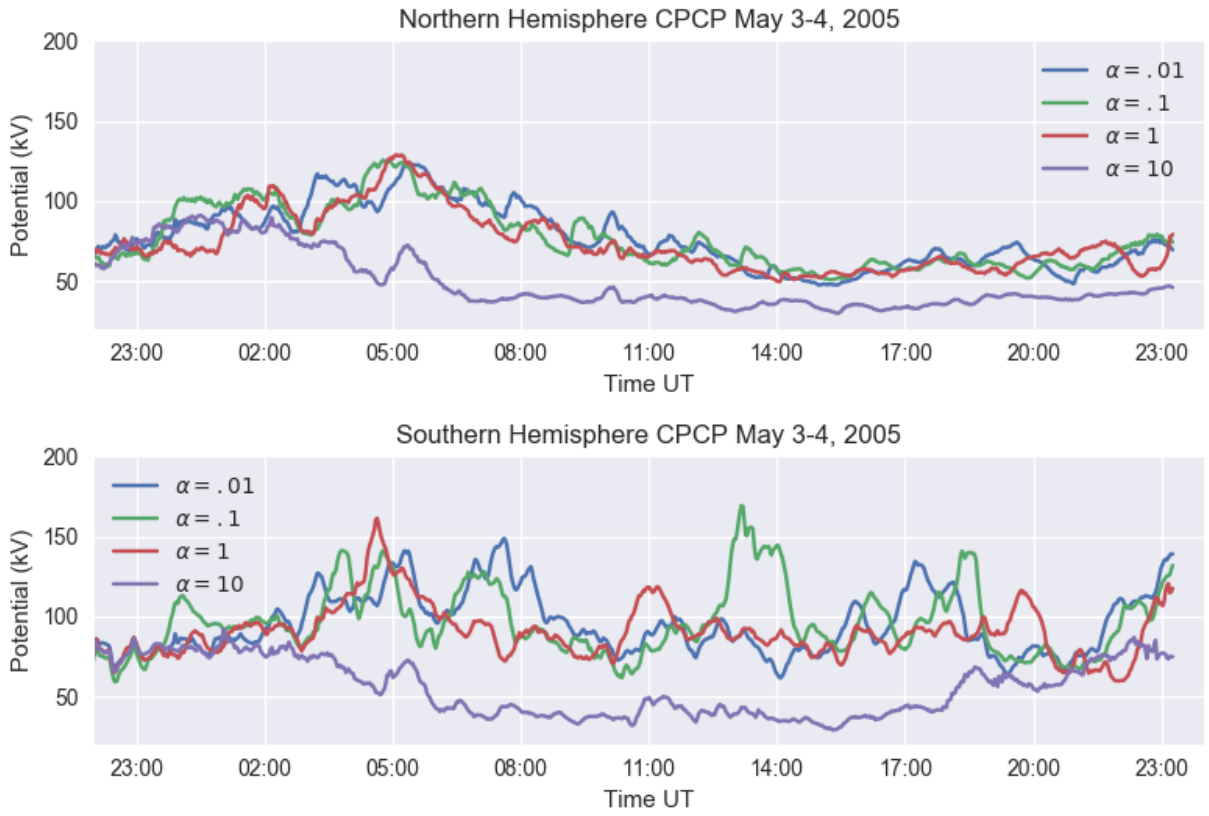

Figure 2.5: The cross polar cap potential for the May 4, 2005 simulation for both the northern (top panel) and southern (bottom panel) hemispheres. The horizontal axis shows the time starting May 3, 2100 UT and covers all of May 4. The vertical axis gives the potential in kV.

hemisphere. This results in more uniform polar conductivities in that region, largely caused by photoionization. By contrast, the southern hemisphere is experiencing winter, and thus the conductivity here is dominated by precipitation as opposed to photoionization. In the $\alpha = 10$ case the asymmetry almost disappears because of the enhanced contribution of precipitation to the conductivity. Where there is low conductivity, the CPCP is also more erratic (Lu et al., 1994), whereas CPCP is much less erratic in the $\alpha = 10$ simulation, where conductivities are larger.

Figure 2.6 shows the CPCP for the four different α cases for the March 17, 2013 event. The trend of decreasing CPCP with increasing precipitation is much more evident here. While the May 4, 2005 simulation had a small difference between the $\alpha = 0.01, 0.1$, and 1 cases, for the storm period the difference is significant. Because storms produce more precipitation that contribute

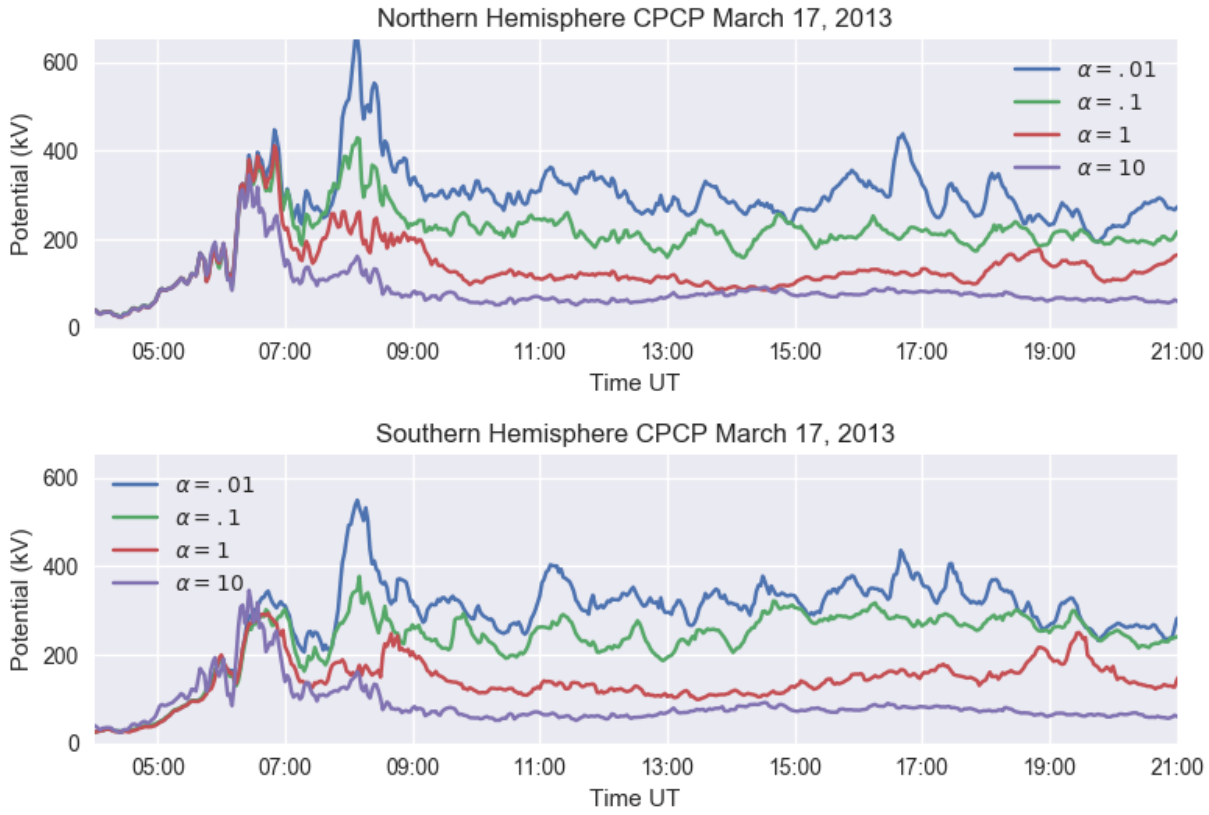

Figure 2.6: The cross polar cap potential CPCP for the northern and southern hemispheres on March 17, 2013, in the same format as Figure 2.5.

more significantly to ionospheric conductivity, reducing the precipitation by $\alpha = 0.1$ or $\alpha = 0.01$ causes the CPCP to be very different from the $\alpha = 1$ simulation.

The $\alpha = 0.01$ and 0.1 storm simulations have also more erratic CPCP than the $\alpha = 1$ and 10 cases. However, unlike in the the calm case, the CPCP has no significant hemispheric asymmetry for the storm time simulation. We attribute the overall symmetry to the increased conductivity due to precipitation, and to the equinox proximity that causes the photoionization to be about equal in both hemispheres.

2.3 Magnetopause Location

To find the location of the magnetopause in the simulation the maximum of the current density in the Y direction (GSE) was located along the Sun-Earth line from 5 to 15 R_E. The maximum marks the location of the subsolar distance of the magnetopause.

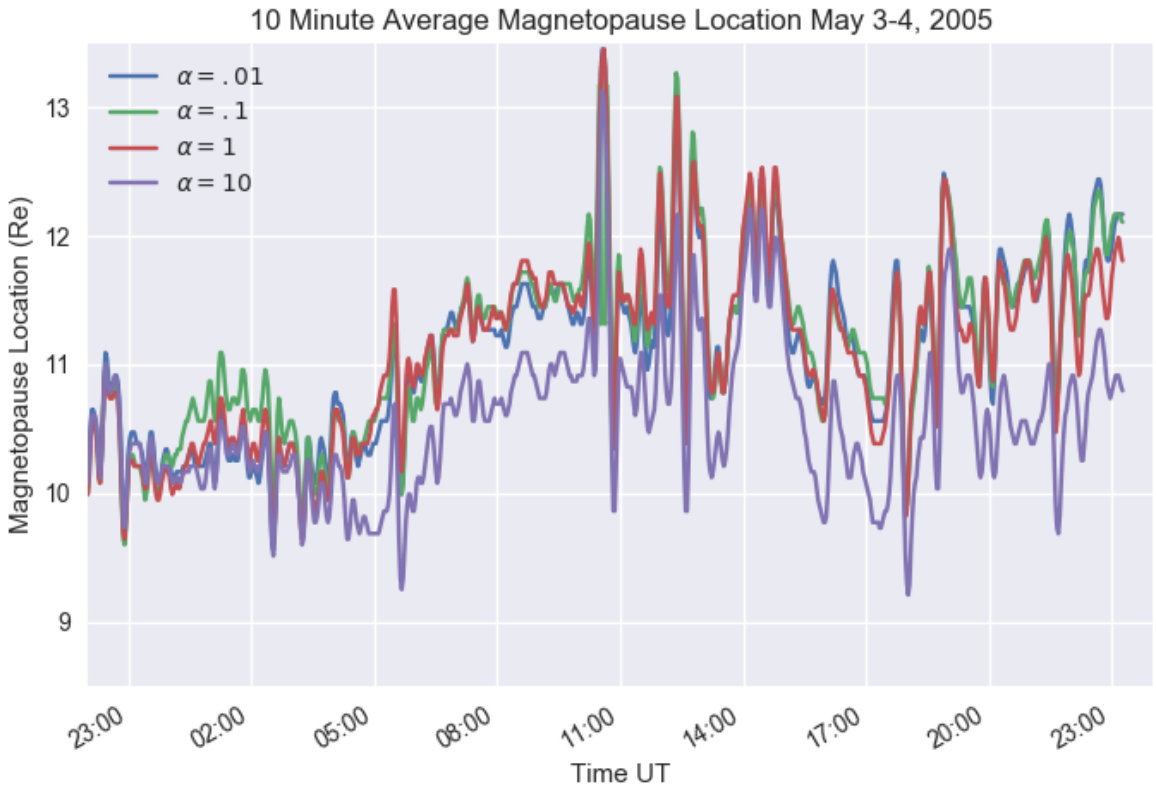

Figure 2.7: The magnetopause location along the Sun-Earth line is shown for the 4 simulations during the May 4, 2005 period. The horizontal axis is UT, and the vertical axis is the distance from the Earth in R_E. The data are plotted with a 10 minute running average to smooth out faster variations.

Figure 2.7 shows the location of the magnetopause along the Sun-Earth line for the four simulations for the May 4, 2005 case. We used a 10 minute running average to filter out short term variations. The magnetopause position is closest to Earth in the $\alpha = 10$ simulation due to the suppressed convection by the higher polar conductivities. From 0500 UT to 1000 UT the magne-

topause location differs from the $\alpha = 1$ simulation by as much as one half R_E. The magnetopause location in the $\alpha = 0.01$ and 0.1 simulation is similar to the $\alpha = 1$ simulation. The actual effect of decreasing the already low precipitation is small, therefore the magnetopause location for the lower α values are similar. These differences reflect the differences in CPCP for the various α values.

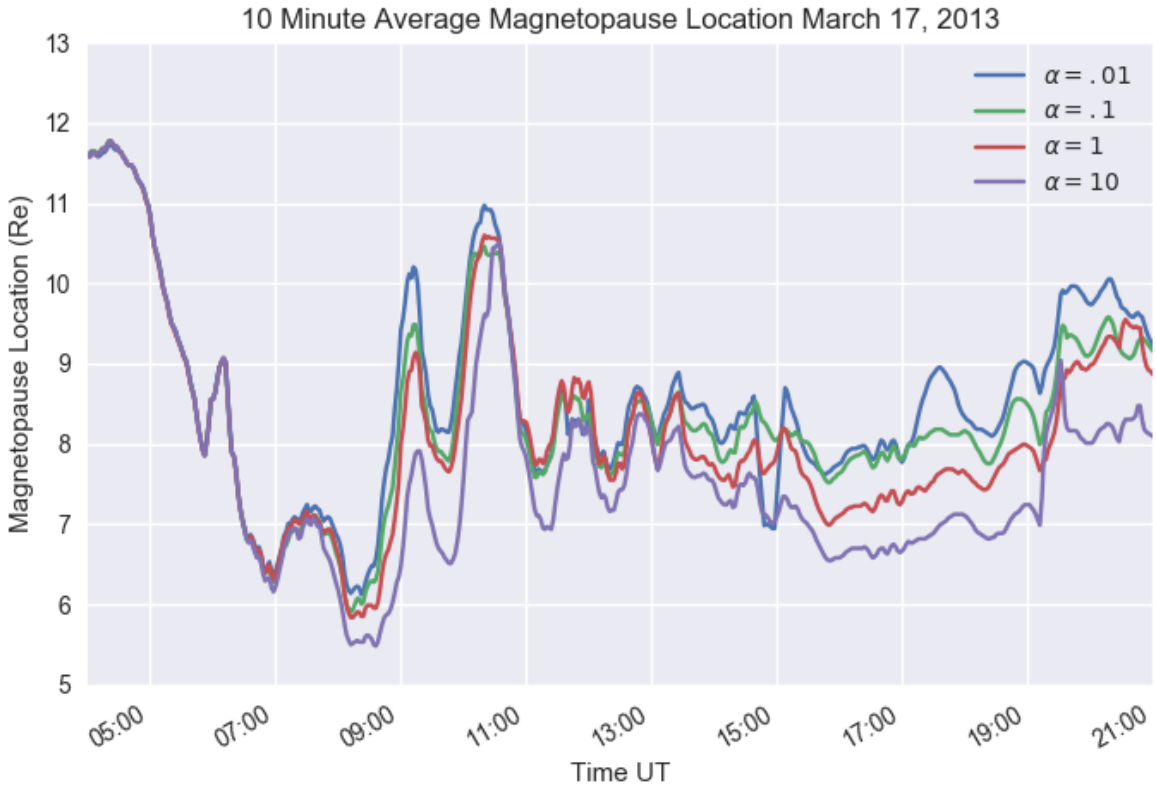

Figure 2.8: The magnetopause location for March 17, 2013 along the Sun-Earth line in the same format as Figure 2.7.

Figure 2.8 shows the magnetopause results of the four simulations of March 17, 2013. As for the other case shown in Figure 2.7 the location of the magnetopause in the $\alpha = 10$ simulation is most earthward. In the $\alpha = 0.01$ simulation the magnetopause is further away from the control simulation because the precipitation for $\alpha = 0.01$, 0.1, and 1 are noticeably different for this storm

event. The lower levels of precipitation and ionospheric conductivity cause the magnetopause to move further from Earth in the $\alpha < 1$ cases. Between 1500 UT to 2100 UT the location of the magnetopause differs at times by more than $1\ R_E$ between all four cases.

2.4 Reconnection Rates

2.4.1 The Hesse-Forbes-Birn Method

In a magnetic system where topologies of field lines with well-defined separatrices exist, Sonnerup (1984) showed that the reconnection rate is equivalent to the integral of the electric field along the separator line. Thus, the reconnection rate is reported as a voltage, which by Faraday's law is equivalent to the rate at which magnetic flux reconnects. For cases when the solar wind is steady and the magnetosphere reaches a steady state, identifying the separator is generally a straightforward process (Dorelli et al., 2004; Ouellette et al., 2010; Komar et al., 2013; Glocer et al., 2016). During periods when the magnetosphere is not in a steady state, especially during storm periods, identifying the separator for the magnetosphere is much more difficult because reconnection is highly time-dependent and several separatrices can exist concurrently.

Hesse, Forbes, and Birn developed a method that does not depend on identifying the different topologies of field lines or the separatrix (Hesse et al., 2005). The Hesse-Forbes-Birn (HFB) method was first used in calculating the reconnection rate in solar corona simulations, but it is extensible to other magnetic domains where the field can be expressed in terms of defined Euler potentials (α,β) (Stern, 1970).

In steady-state ideal MHD, magnetic field lines are equipotentials. However, in non-steady-state, and resistive MHD, localized diffusion regions can create potential differences along the field lines (Hesse and Schindler, 1988). A field line that intersects a diffusion region can have a substantial potential difference on either side of the diffusion region, even though they are one the same field line. This difference defines a quasi-potential, Ξ,

$$\Xi(\alpha,\beta) = -\int_{\alpha,\beta} E_{\parallel}\, ds = \psi_2 - \psi_1, \tag{2.1}$$

where the α and β are the Euler coordinates defining a magnetic field line, $E_{\parallel}$ is the parallel electric field, and $\psi_{1,2}$ are the potentials at different points along the field line. In magnetosphere simulations the latitude and longitude of the ionospheric field line footpoints provide a convenient system of Euler coordinates. Hesse et al. (2005) further showed that the field line that contains the maximum quasi-potential contains the entirety of the reconnection rate distributed along that one field line and equals the total reconnection rate in the domain,

$$R = -\Xi_{\max} = \max \int_{\alpha,\beta} E_{\parallel}\, ds. \tag{2.2}$$

The HFB method greatly simplifies the reconnection rate calculation since no magnetic topologies or magnetic separators need to be identified. The maximum quasi-potential along any single field line is sufficient to describe the magnetic reconnection rate. The tradeoff, is the necessity to calculate the integral in equation 2.2 for all field lines to find the function $\Xi(\alpha,\beta)$. This needs to be repeated for each time step.

A numerical difficulty arises from identifying the field line with the maximum Ξ. Since the size of the reconnection region mapped onto the ionosphere can be much smaller than the ionospheric grid cell size, it is necessary to super-sample the ionospheric grid to assure all the possible reconnection regions are sampled sufficiently. We accomplish this by taking the ionospheric surface and dividing each grid cell, originally 0.5° in latitude and 3° in longitude, into 256 (16x16) rectangles. We performed a convergence test by dividing evenly each grid cell into 8x8, 16x16, 32x32, and 64x64 smaller rectangles, then field lines were traced and compared the maximum Ξ found. We found that dividing by each grid cell into 16x16 gave sufficient accuracy of Ξ.

We then trace from each of the super-sampled rectangles on the ionospheric grid until the field line either comes back to the Earth, or exits the simulation box. We integrate $E_{||}$ while tracing and identify the Ξ_{max} and Ξ_{min} with R as,

$$R = \Xi_{\max} - \Xi_{\min}. \tag{2.3}$$

The HFB method has already been shown to be effective for studying magnetic domains on the sun and gives reconnection rates that are reasonable (Hesse et al., 2005). To assure that the HFB method was implemented correctly in OpenGGCM, the HFB method was benchmarked against separator reconnection measurements in a steady state simulation with southward IMF and imposed constant resistivity of $\eta = 5 \cdot 10^4\ \Omega m$. The solar wind conditions for this simulation are $V_{sw} = 400\ km/s$, $B_{IMF} = 5\ nT$, and IMF clock angle $45°$.

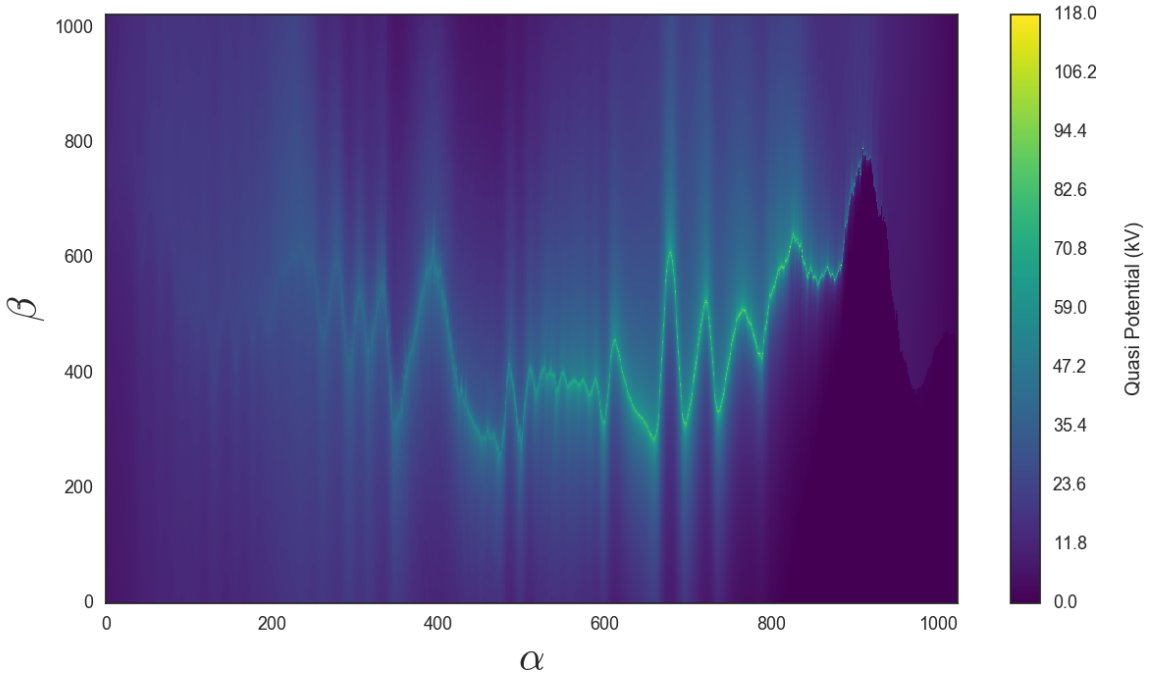

Figure 2.9: Shows the calculation of Ξ for the test simulation as a function of α and β, where the axis numbers are the flux coordinates labelled by integer ie, β covers $0.5°$ latitude at a resolution of $0.5°/1024$.

Figure 2.9 shows Ξ as a function of flux coordinates chosen in the northern ionosphere. In this case, α is chosen along lines of constant longitude that span $130°$ around noon MLT and β is along lines of constant latitude that span $0.5°$ around the open-closed boundary. The ridge in Ξ follows

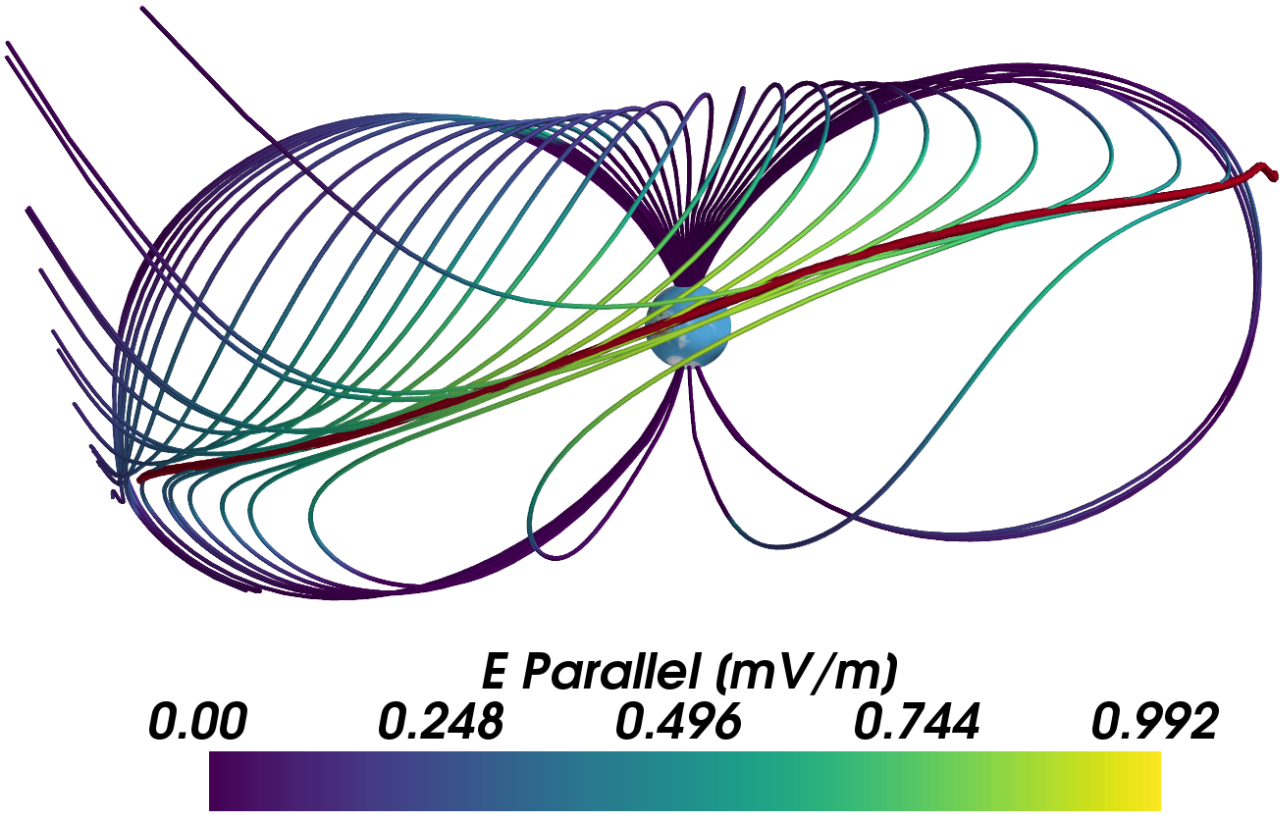

Figure 2.10: A three-dimensional projection of some of the day-side magnetic field lines that contribute in the calculation for Ξ in the test simulation. They are colored by the $E_{||}$ with the dark red line marking the separator.

A subset of the magnetic field lines used to calculate Ξ is shown in Figure 2.10. They are colored by the parallel electric field, which highlights the dayside reconnection that peaks at the subsolar point. The global separator line is shown in dark red stretching across the dayside magnetopause. The Earth is shown for scale.

In benchmarking the HFB method against traditional methods, Ξ is calculated to be $118\ kV$ for flux coordinates that sample dayside reconnection. In the same simulation, the electric field integrated along the dayside separator (the singular field line that connects the magnetic nulls) is $134\ kV$. The HFB method is low by approximately 12%. For the study of real events where separators are difficult to find, we conclude that the HFB method gives a sufficiently accurate measure of the reconnection rate.

2.4.2 Reconnection Rate Results

Figures 2.11 and 2.12 show the results of the reconnection rate R calculated in OpenGGCM for both days, and for all four cases. The global reconnection rate calculation is performed three times. We use the magnetic field lines originating from the northern hemisphere (NH) and field lines originating from the southern hemisphere (SH), and a global calculation with all field lines originating from both hemispheres. Splitting the hemispheres allows a more accurate comparison of the reconnection rates with the CPCP for each hemisphere. The HFB method depends on finding the field lines that contain the largest potential drop right after reconnection occurs. These field lines should be connected to the solar wind, trace back to either hemisphere, and ideally should give the same result. We thus trace the field lines that originate from the NH, the SH, or globally, and use equation 2.3 to take the respective $\Xi_{\max}$ and $\Xi_{\min}$.

We examine the global reconnection rate where the $\Xi_{\max}$ and $\Xi_{\min}$ are taken globally. If the $\Xi_{\max\,/\,\min}$ are in the same hemisphere the value obtained by the hemispheric calculation is identical to the global reconnection rate. If the $\Xi_{\max\,/\,\min}$ are in different hemispheres then there is a slight increase in the global reconnection rate when compared to the global reconnection rate derived from the hemispheric calculation. We find that in these cases the global reconnection rate is on average 0-15% larger than the largest hemispheric rate. The global reconnection rate has the same qualitative pattern as the hemispheric calculations.

Figure 2.11 shows the reconnection rates calculated for the May 4, 2005 event. The $\alpha = 10$ case has the lowest reconnection rate on average, while the $\alpha = 0.01, 0.1, 1$ cases are about the same. There are spikes in each of the α cases, and some are similar across all four α's, but there are also some peaks in R that are unique in each case. These reconnection rate spikes may correspond to substorms. It is well established that substorm reconnection is tied to the ionospheric precipitation (Raeder et al., 1996) and can affect the substorm reconnection timing.

For the March 17 case shown in Figure 2.12, the trend of decreasing R with increasing precipitation is more evident, and most pronounced during the 0600-0900 UT period. For both events the difference in the magnetic reconnection rate is not as significant as the CPCP or magnetopause

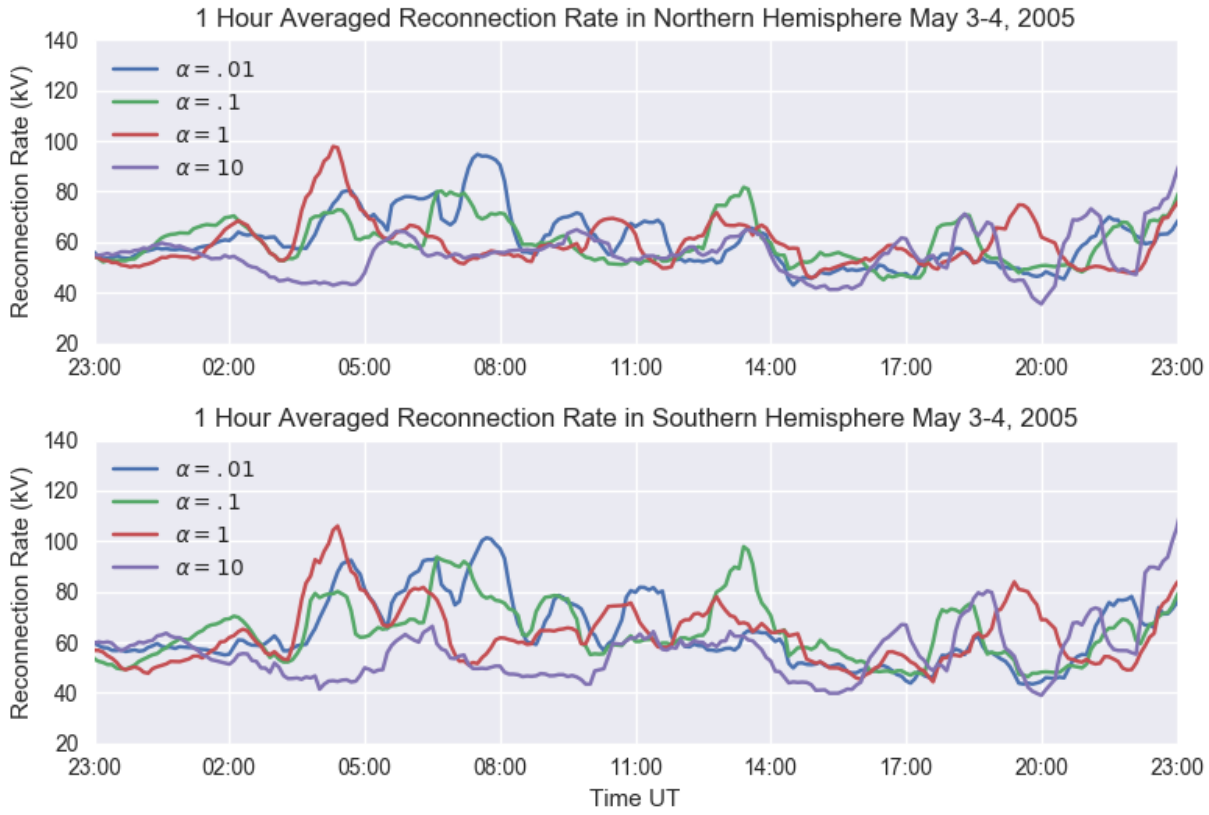

Figure 2.11: The reconnection rates for May 4, 2005 for the four precipitation factor cases, obtained for the northern hemisphere (top panel) and southern hemisphere (bottom panel). The horizontal axis is the UT and the vertical axis is the reconnection rate in kV. Data points are a one hour running average.

location, but there also appears to be a small trend of decreased, and more stable reconnection when the precipitation is increased.

2.5 Chapter Discussion

Figure 2.13 shows the mean of the values examined over the whole simulation period for May 4, 2005, for the average values of CPCP, and reconnection rate (R).

An asymmetry is clearly evident in the CPCP between the NH and SH with the SH values greater than the NH values because the NH is more sunlit. The CPCP also shows that for the $\alpha =$

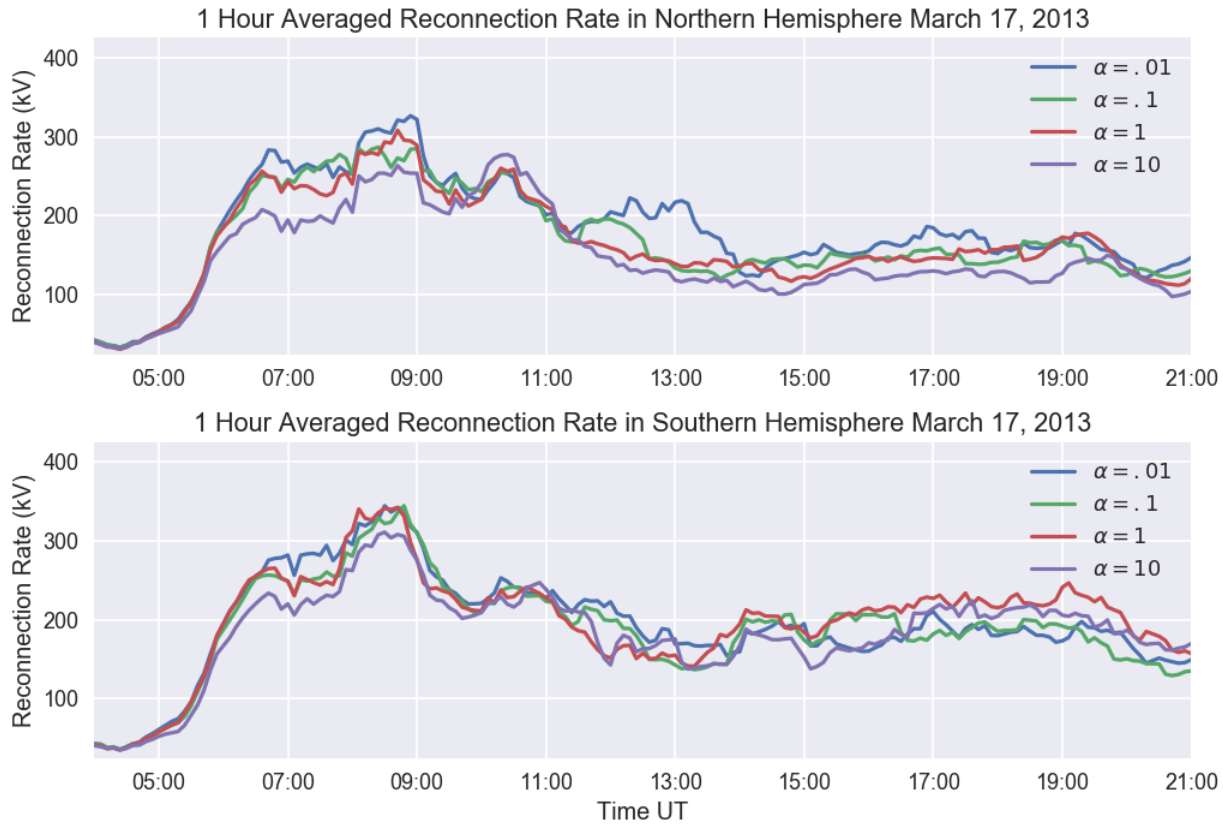

Figure 2.12: The reconnection rates for March 17, 2013 for the four precipitation factor cases in the same format as Figure 2.11.

$0.01, 0.1, 1$ cases the CPCP remains very similar, because the effect of precipitation on Pedersen conductance is small compared to the photoionization. As the precipitation is increased in the $\alpha = 10$ simulation, the CPCP decreases as expected. A similar pattern is found for the magnetopause location; it remains quite stable except for the $\alpha = 10$ simulation where it is reduced by as much as 0.5 R_E (this corresponds to about 6 grid cells in the simulation).

The reconnection rates are more symmetric than the CPCP. As the precipitation is increased from $\alpha = 1$ to $\alpha = 10$ magnetic reconnection in the magnetosphere is reduced by about 7 percent. During some intervals the variation can be very large, for example, up to 50% reduced compared to the control simulation at 0400 UT, which may be attributed to substorm activity. The $\alpha = 0.01$ and $\alpha = 0.1$ cases remain at values similar to the control simulations as expected. The global reconnection rate is included to show the accuracy of the separate hemispheric calculations.

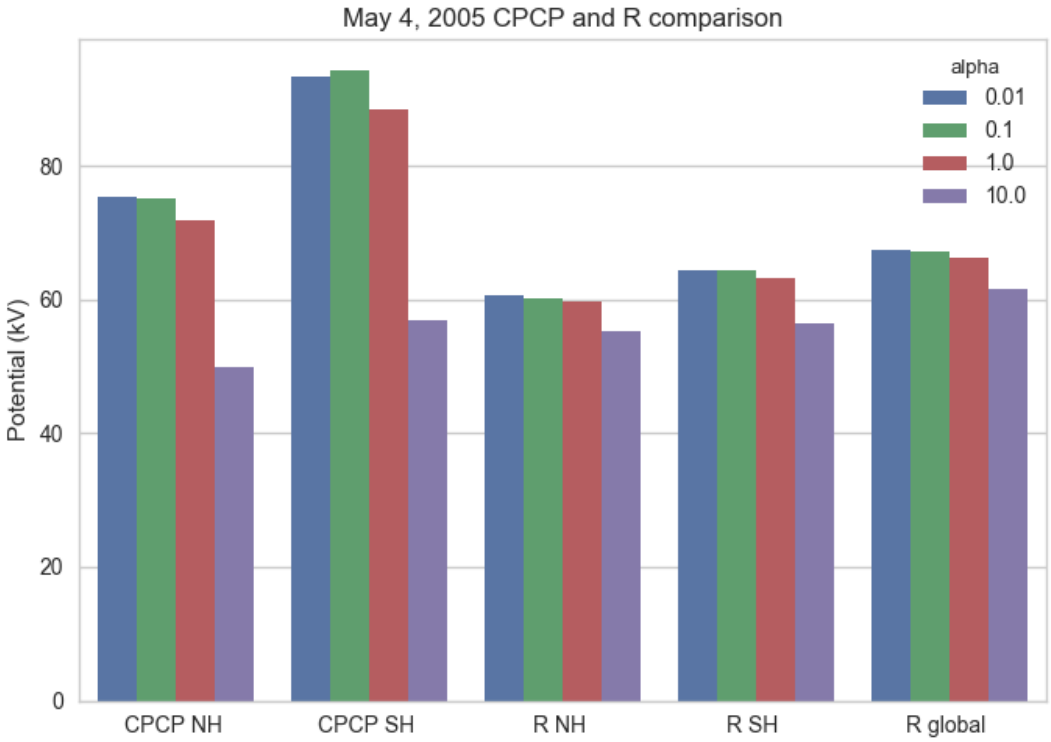

Figure 2.13: Bar plot showing a comparison of the CPCP and R for the May 4, 2005 calm day event. Each alpha is graphed for the CPCP in the northern (NH) and southern (SH) hemishere, as well as the reconnection rate R for NH, SH, and the global rate. The vertical axis gives the potential in kV.

Figure 2.14 shows the simulated CPCP values averaged over the length of the simulation for the March 17, 2013. The CPCP shows the same pattern found in the May 4, 2005 simulation, namely, as precipitation is increased the CPCP decreases significantly. March 17 is three days from the equinox, so both hemispheres are sunlit approximately the same amount. Therefore close hemispheric symmetry exists the magnitude of the CPCP.

The trend of increasing precipitation resulting in lower reconnection is likewise evident for this day, more so in the northern hemisphere (a range of 19% from the $\alpha = 0.01$ to $\alpha = 10$ cases), than in the southern hemisphere (a range of 6% from the $\alpha = 0.01$ to $\alpha = 10$ cases). This may result from the large variation of the reconnection rate in the southern hemisphere for the $\alpha = 1$

case from 1400 to 2000 UT. During this period the reconnection rate in the southern hemisphere is 17% larger than in the northern hemisphere, but it is not clear where this asymmetry comes from.

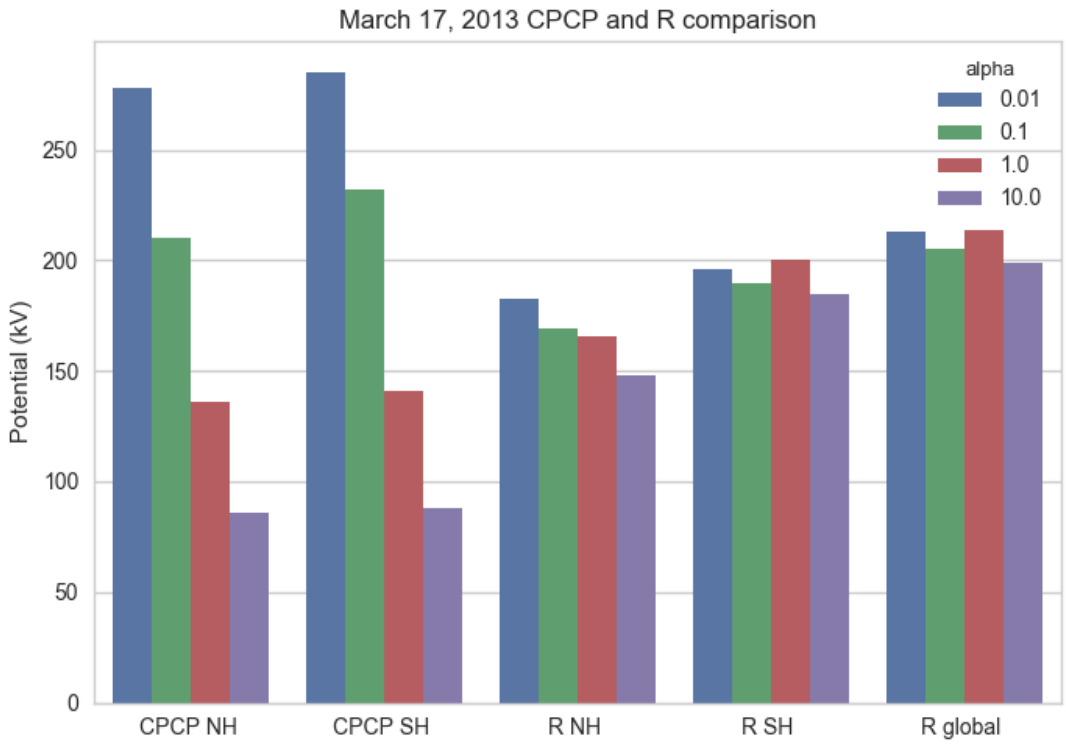

Figure 2.14: The bar plot shows a comparison of the CPCP and R for the March 17, 2013 storm day event in the same format as Figure 2.13.

The question arises whether the reconnection rate is affected by the precipitation? The answer seems to be both yes and no. On short time scales (hours) the reconnection rate in the magnetosphere is influenced by the amount of conductance in the ionosphere which is directly related to the precipitation. On longer time scales (tens of hours) the relation is not as clear. There appears to be a slight decrease in the reconnection rate as precipitation is increases for these two simulation events, but the correlation is weak. The only outlier of this trend is the $\alpha = 1$ case for the 2013 storm period.

The difference between R and CPCP is significant for both events and for some α values. In ideal steady state conditions the R and CPCP values should be very close to each other. Although

the cases simulated here are rarely in steady state, the differences between R and CPCP should average out, however, the differences in R and CPCP are significant. For the calm day $\alpha = 0.01, 0.1, 1$ cases the R value is smaller than the CPCP value by about 25%, while in the $\alpha = 10$ case the R values and the CPCP values are comparable. For the storm day there is a general trend of decreasing difference between CPCP value and R value, with R being more than double the CPCP in the $\alpha = 10$ case.

Viscous interaction (Axford, 1964) with the solar wind can explain why CPCP is higher than R. It was shown by Bruntz et al. (2012) that the viscous interaction has an inverse relationship with Pedersen conductance. For typical solar wind conditions, such as those in the 2005 case, they found that viscously driven potentials could range from 45 to 15 kV, depending on the Pedersen conductance. This is close to the threshold of the difference that is seen in the calm period with small influence of precipitation. The differences are larger for the 2013 case, but there the solar wind velocity and densities are much higher, resulting in larger viscous potentials for low the precipitation/conductance cases.

Nagatsuma (2004) studied the conductivity dependence of CPCP saturation by changing the solar zenith angle. They found that when the Pedersen conductance increased, the limit at which CPCP saturated decreased. This explains how the cases where CPCP is lower than R, due to polar cap potential saturation. In the simulations, precipitation is causing the Pedersen conductivities to significantly increase leading to the CPCP being substantially lower than R for the 2013 $\alpha = 10$ case.

2.6 Chapter Summary

Scaling ionospheric precipitation has significant effects on the magnetosphere - ionosphere system. We have shown that,

1. There is an inverse relationship between the amount of precipitation energy flux and the CPCP. By only modifying the amount of precipitation and leaving all other inputs of the

model the same it was found that increasing precipitation by an order of magnitude into the ionosphere reduces CPCP by up to 30%. Decreasing the precipitation by two orders of magnitude during the calm case did not have much effect on CPCP because Particle precipitation did not have a large affect on the CPCP in the first place. During the storm period however, decreasing the precipitation by two orders of magnitude nearly doubled the CPCP.

2. There is an inverse relationship between the amount of precipitation and the location of the magnetopause standoff distance. Increasing the precipitation by one order of magnitude caused the subsolar magnetopause location to move closer by 0.5 R_E for the calm period and by 0.4 R_E for the storm period. Decreasing the precipitation by two orders of magnitude increased the magnetopause standoff distance by 0.5 R_E only for the storm period.

3. The relationship between the precipitation and the magnetic reconnection rate is not as clear. On short time scales (hours) the reconnection is significantly modified by different conductivities, but for longer time scales (tens of hours) the reconnection rates average out. There is a slight decrease in reconnection rate as precipitation is increased, but it is not clear if this stems from event selection bias, viscous interactions, or numerical errors.

4. CPCP and R are not always the same in the simulations. A potential explanation for this could be viscous interaction and polar cap potential saturation. Both have an ionospheric conductance dependence which could explain why CPCP and R can be different. For low conductance cases, viscous interactions are strong which should result in CPCP being higher than R. For high conductance cases the polar cap is in the saturation regime and CPCP may be lower than R. Both the effect of viscous interaction and CPCP saturation would require further study to affirm this relationship.

5. The Hesse-Forbes-Birn method for calculating the magnetic reconnection rate works well when applied to the Earth's magnetosphere and obviates the need to find topological features in the magnetic field such as nulls and separators.

The changes in ionospheric conductance due to variable precipitation thus play an important part in the S-M-I system, and can influence the cross polar cap potential, magnetopause location, and the magnetic reconnection rate.

CHAPTER 3

EFFECTS OF IONOSPHERIC CONDUCTIVITY ON SUBSTORM FREQUENCY AND MAGNITUDE

3.1 Entire Ionospheric Conductivity Effects on Substorms

The previous chapter showed that changing the ionospheric conductivity made significant changes to the CPCP and some changes to the reconnection rate. These parameters can give indications of the frequency and magnitude of substorms. Changing the energy flux of the precipitation mostly affects the nightside, so in this chapter the ionospheric conductivity over the whole ionosphere is varied. Once the ionospheric model has both the solar input and the particle precipitation, and the height integrated Hall and Pedersen conductance are calculated, the conductivity was changed by multiplying it by factor β. The factors chosen for β are .25, .5, 1, 2, and 4.

Section 3.2 is a study where different values of $F_{10.7}$ are used to demonstrate how dayside conductivity affects substorms. Changing the ionospheric conductivity in these ways to see how the frequency and magnitude of substorms change, gives an indication of the importance of conductivity on substorms.

3.1.1 Simulation Setup

The fully coupled OpenGGCM-CTIM-RCM model was used. The grid extended from 40 R_e in the sunward direction to 1000 R_e tailward, with the y and z directions extending 48 R_e. A moderate resolution of 16 million grid points was used. It is helpful to simulate a period that someone has studied previously to see how the simulation compares to observational data, the date 16 May 2011 from 0 UT to 18 UT was selected, it has previously been studied by Murphy et al. (2013). They used AMPERE, ground magnetometers, and all-sky imagers to identify onset and

FAC current structures. They identified a substorm onset at 8:17 UT in ground magnetometer data, followed by auroral enhancement and poleward expansion with a strengthening of the field aligned currents in the nightside.

Solar wind data from the WIND satellite was used as input, and is shown in Figure 3.1. The solar wind velocity is close to a constant 500 km/s and the B_z turns negative and stays negative from 6:00 to 8:30 UT which coincides with a substorm identified by Murphy et al. (2013). There are many B_z turnings that occur for the rest of the day, but not many sustained negative periods.

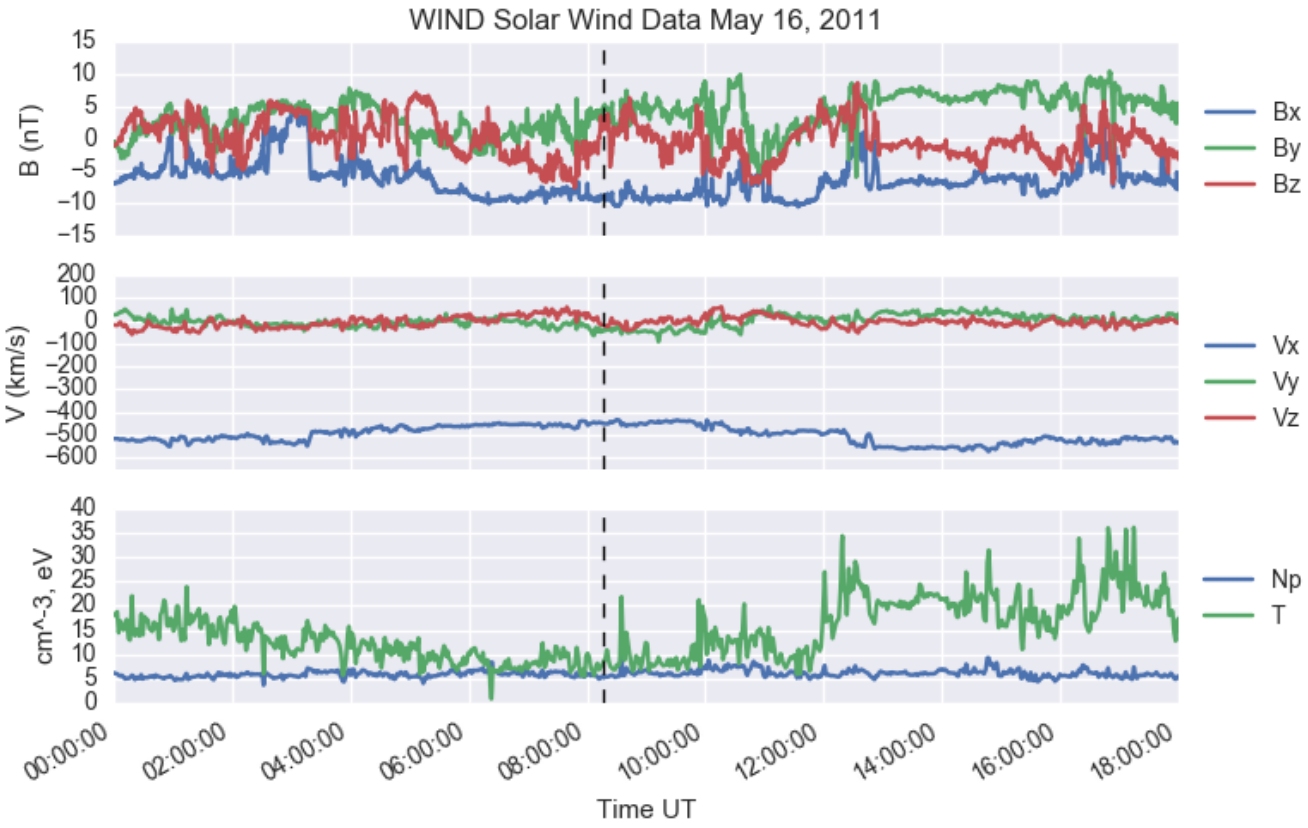

Figure 3.1: This figure shows solar wind data from the WIND satellite for 16 May 2011. The black dashed line indicates a time of a substorm identified by Murphy et al. (2013).

3.1.2 Effect of Changing β on Ionospheric Conductivity

Figure 3.2 shows the ionospheric potential and the Pedersen conductance of the simulations at 8:00 UT, just before Murphy et al. (2013) found a substorm in the ground data. The left panels show the potential and range from a β of .25 in the uppermost left to the β of 4 on the bottom. The potential patterns show a simple dual cell convection pattern. As the conductivity increases the potential decreases, as was found in previous simulations. The right panels of Figure 3.2 show the Pedersen conductance of the simulations. Again, recognize that both the photoionization and particle precipitation effects are changed by β.

As another measure of the ionospheric conductivity in the system the CPCP was graphed in Figure 3.3, the hemispheres were separated to show the hemispheric asymmetry. May is close to summer so the Northern Hemisphere (NH) is expected to have a lower total CPCP and less variability as it is more sunlit which is evident in the cases for β larger than 1 (Lu et al., 1994).

The CPCP and the variability decrease as conductivity increases. There is a significant peak at 7:50 that is visible in all the β simulations, and the timing is similar in all simulations. Another peak in CPCP occurs around 10:30-10:45, each higher β value simulations appears to shift to a later time. The last peak can be described as a plateau, as the values increase around 14:00 and stay there for the rest of the simulation. It is more pronounced for the lower β simulations. This is about 30 minutes earlier than the substorm identified by the Murphy et al. (2013) study, who identified a substorm at 8:17 UT.

Figure 3.4 shows the reconnection rates calculated using the HFB method as described in section 2.4.1. The reconnection rate with field lines connected to the NH and SH are graphed. The magnitude of the reconnection and the CPCP for the lower β simulations are similar, but reconnection rate is larger than CPCP for the high β simulations, showing CPCP saturation.

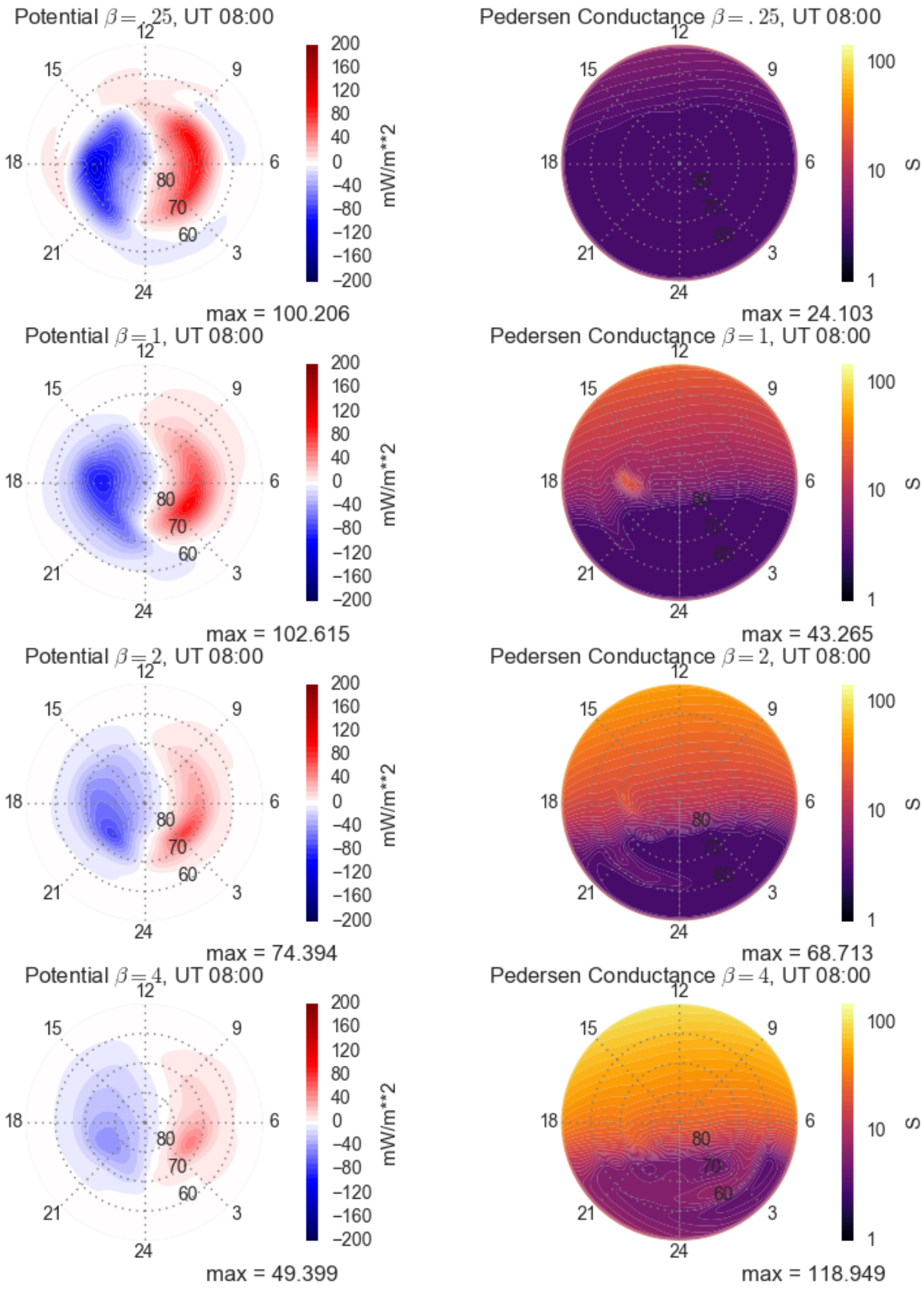

Figure 3.2: Graph of the ionospheric potential (left panels) and the Pedersen conductance (right panels) from one snapshot of time at 8:00 UT 16 May, 2011.

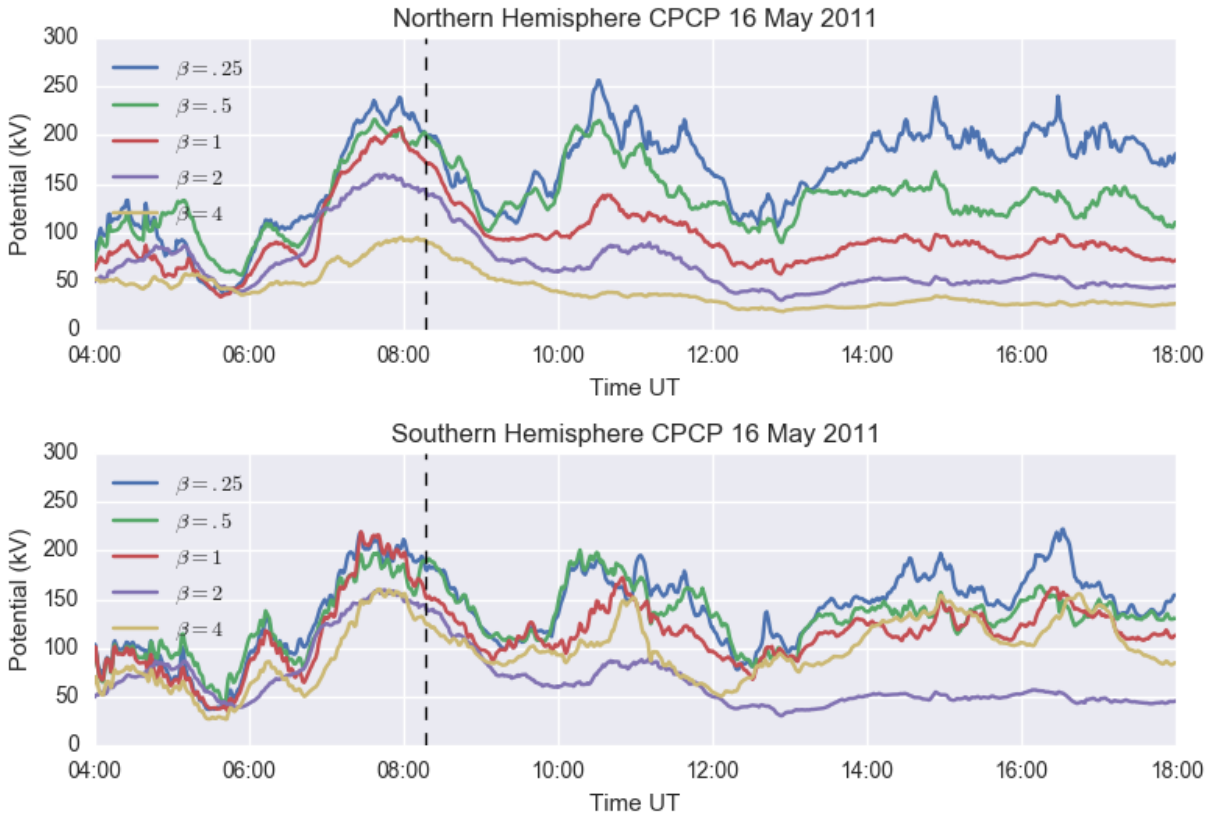

Figure 3.3: Graph of the CPCP for the Northern and Southern Hemisphere. Vertical axis is potential in kV. CPCP is graphed at 1 minute cadence for 16 May 2011. The black dashed line indicates a time of a substorm identified by Murphy et al. (2013).

Similar to Chapter 2, the reconnection rate values do not cover as large of a range as the CPCP. In the reconnection rates there are 3 general peaks that correspond at about 7:30, 10:30 and 13:00 UT, these peaks correspond with similar peaks in the CPCP. The 7:30 peak precedes the CPCP peak by about 20 minutes, while the timing of the 10:00-10:40 peak corresponds to the 10:30-10:45 peak in CPCP. The 13:00 peak in reconnection rates precedes the 14:00 UT CPCP plateau by about an hour.

It should be noted that there is significant asymmetry specifically in the $\beta = 4$ simulation. The SH CPCP is significantly higher than the NH, while the reconnection rates for NH are generally higher than the SH. The NH saturating at a lower CPCP is expected since it has a higher conductance, and the higher the β the more the asymmetries already present are magnified.

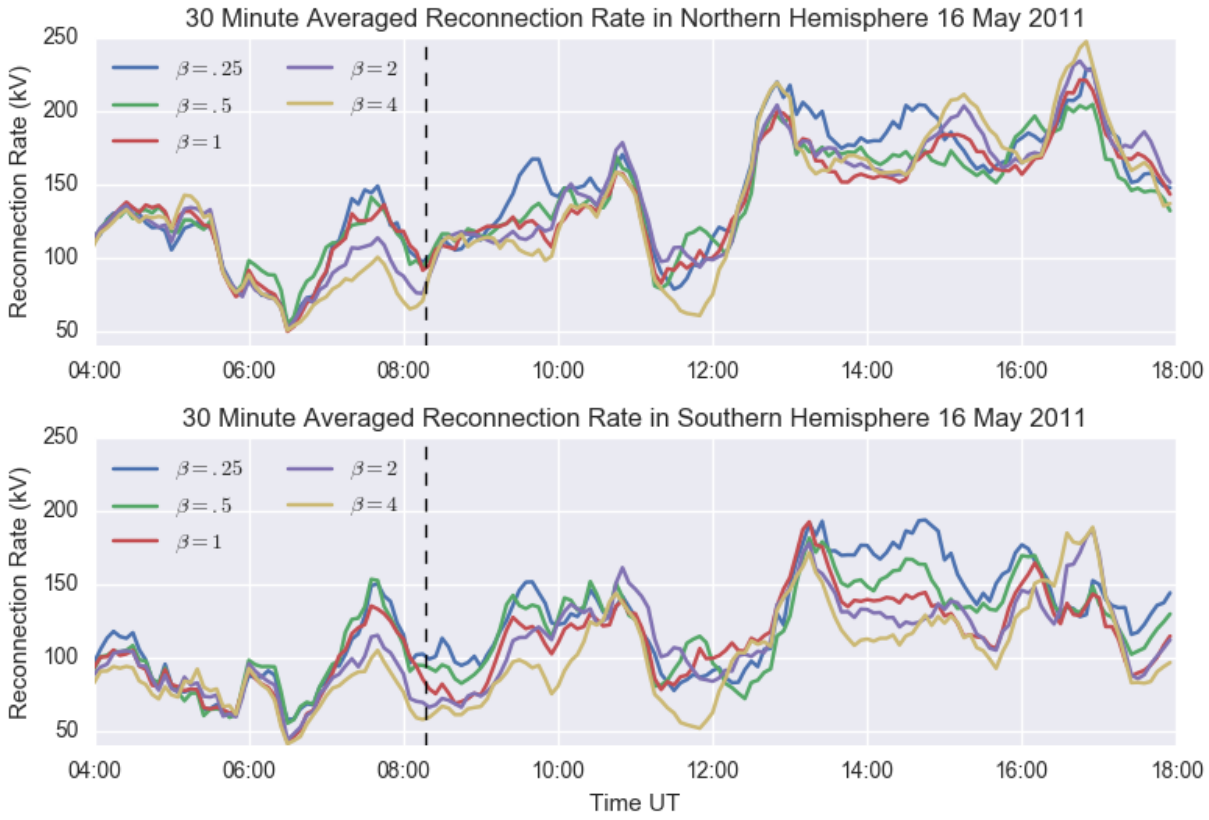

Figure 3.4: Reconnection rate calculated from Northern and Southern Hemisphere field lines using the HFB method. The five different β values are plotted. These reconnection rates are a running average with a window of 30 minutes.

Figure 3.5 shows the averages for the CPCP and reconnection rates (R) for the β simulations. The CPCP in the NH and SH have a much wider range than R, and the NH has a wider range than the SH.

The values of the reconnection rate are greater than the CPCP, especially for higher β runs, showing the polar cap is operating in the saturation regime. The viscous potential does not have much of a contribution. By decreasing the conductance four-fold, the CPCP and R are comparable. The polar cap was saturated as the control simulation shows R is greater than CPCP by an average of 52 kV.

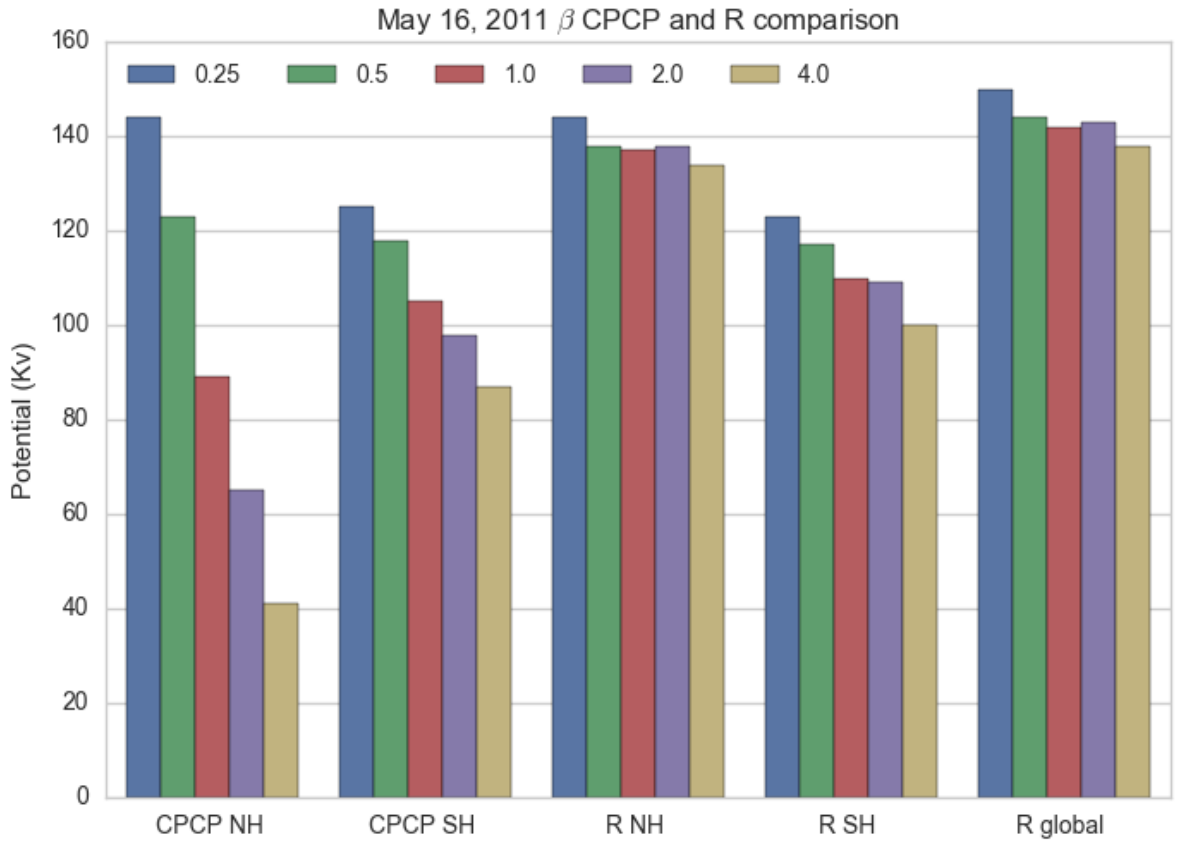

Figure 3.5: The averaged CPCP and reconnection rates are plotted as a bar plot for the five β simulations for 16 May 2011. The black dashed line indicates a time of a substorm identified by Murphy et al. (2013).

3.1.3 Substorm Onset Time Identified by Auroral Intensification

Being able to determine the substorm timing is difficult as there are many different methods used to determine the start of a substorm, such as, magnetogram signatures, auroral signatures, Pi2 pulsations, electric field enhancements, (Rostoker et al., 1980). The method of detecting auroral enhancements in the midnight sector is used to see if there is a difference in the substorm occurrence rate by varying β to change the ionospheric conductivity. In order to understand the dynamics of the magnetosphere-ionosphere system, auroral enhancements were identified using a less restrictive criteria, and introduce a more strict criteria for substorms.

The criterium for auroral enhancements is the maximum precipitation energy flux increases by at least $1\ mW/m^2$ within 20 minutes. This criteria permits the identification of many auroral enhancements that have corresponding X-lines in the magnetotail. This criterium includes substorm events, but also includes many reconnection and particle precipitation events that are not as strong as substorms.

A more strict criterium that is associated with a traditional substorm, is also used, stating that if the maximum precipitation increases by 80% within 20 minutes it is classified as a substorm. This study is classifying events by two levels, that describe M-I coupling through reconnection and particle precipitation, one that included many of the smaller reconnection events, and one level that is associated with only substorms.

Figure 3.6 shows the precipitation energy flux during a substorm for the $\beta = .5$ simulation during a substorm that occurs from 13:40-14:30 UT, each frame progresses 10 minutes showing the variation through time. The initial enhancement occurs at 14:00 UT and then expands for the next 30 minutes. This event fulfills the substorm criteria because it shows the intensification with the westward travelling surge. For the substorm events identified there was a strong westward travelling surge, whereas for many of the weaker auroral enhancements, westward travelling surges do not occur.

Figure 3.6 shows a typical intensification signature of a substorm. Auroral enhancement signatures were identified in the data by graphing the maximum particle precipitation energy flux, shown in Figure 3.7 for the five different β variations. Again, each peak that rises more than $1\ mW/m^2$ in 20 minutes is categorized as a auroral enhancement.

Table 3.1 shows the auroral enhancements for each simulation and the times that they start. The enhancements that occur for each separate simulation within 30 minutes of each other were grouped together. The events having lower conductance have a greater occurrence of auroral enhancements.

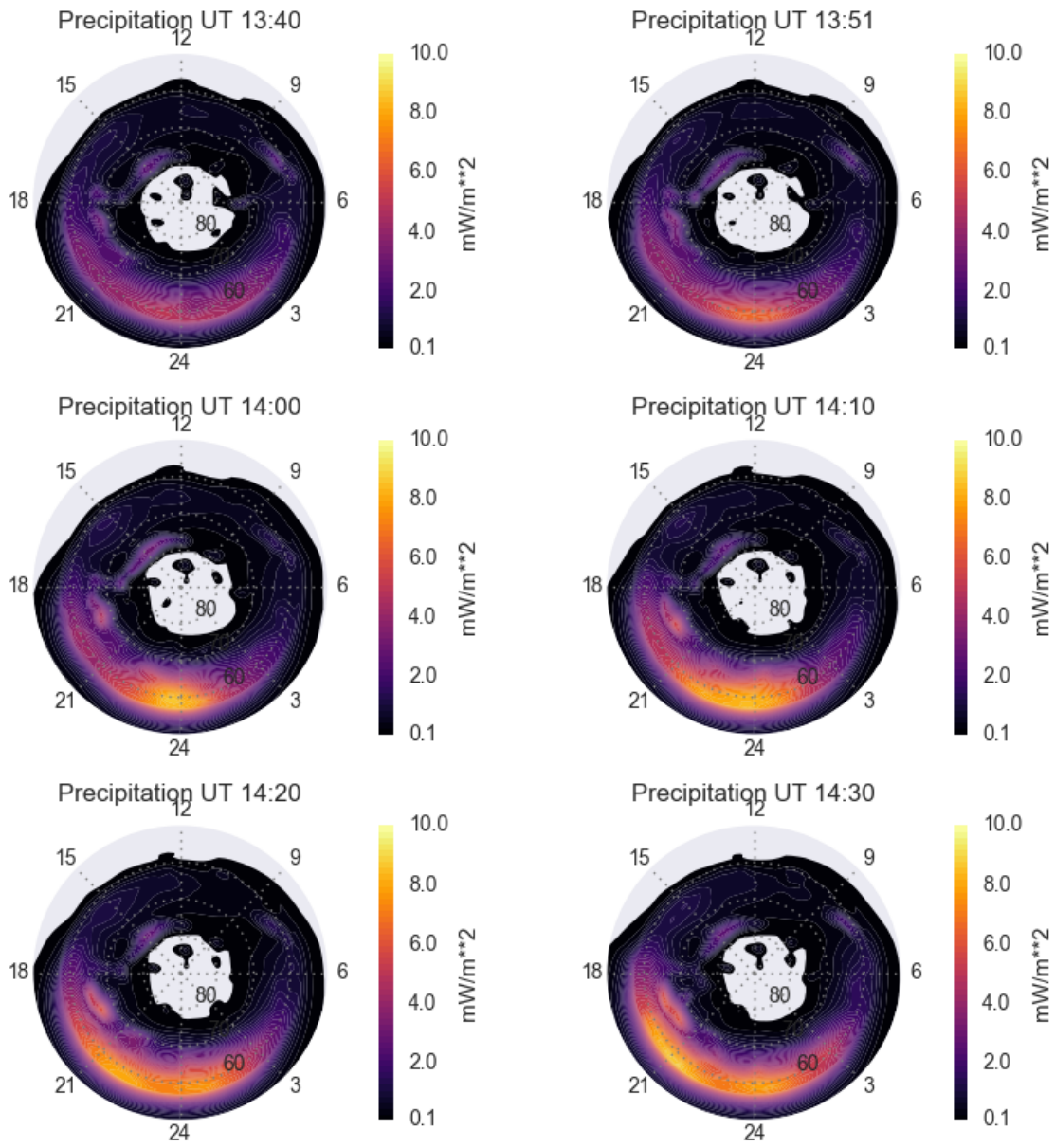

Figure 3.6: Shows the total precipitation energy flux for both diffuse and discrete precipitation for the $\beta = .5$ simulation. Snapshots of the simulation are shown every 10 minutes from 13:40 to 14:30.

An auroral enhancement does not necessarily mean that a substorm is occurring in the model. The times that are underlined are the auroral enhancements that satisfy the more strict criteria of a substorm, namely they increase by 80% within 20 minutes. The only auroral enhancements that qualify with this more strict criteria are the $\beta = .25$, and $.5$, at around 9:50 UT and then the $\beta = .25$

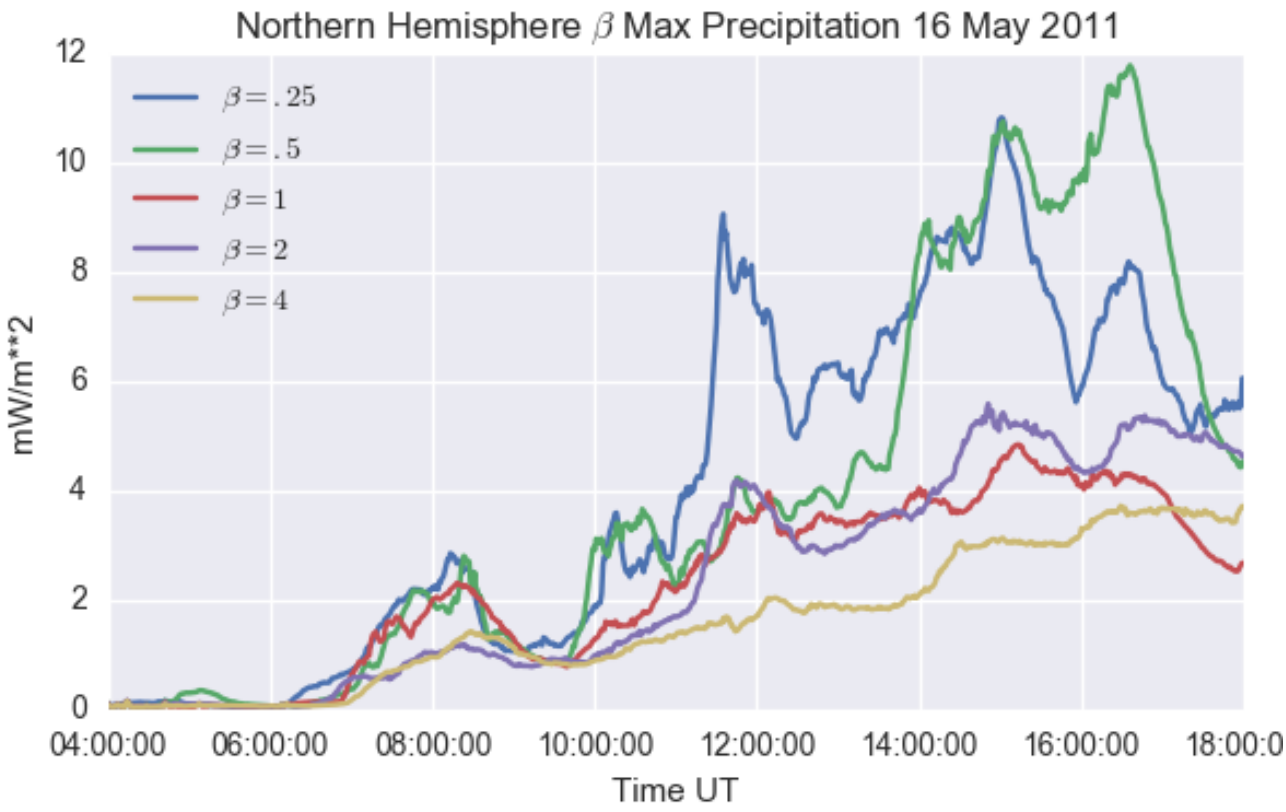

Figure 3.7: The maximum precipitation energy flux is shown for all five simulations.

at 11:20 and the $\beta = .5$ at 13:50 UT. The auroral enhancements at 7:00 UT all qualify under the substorm criteria, but this is because the simulation is still initializing and the precipitation is still too low. Another peak to note is the one in $\beta = 2$ at 11:20 UT. It increased by 78% in 20 minutes so it just missed the cutoff.

Figure 3.8 shows the trend that increasing the β will cause a decrease in the number of auroral enhancements. The two substorms that do occur also seem to occur later as the conductivity is increased. The $\beta = .5$ simulation substorm is 2.5 hours after the $\beta = .25$ substorm.

3.1.4 Substorm Identification by Magnetotail X-line Formation

Another tool for identifying substorms is to look at the X-lines in the magnetotail. Each of the simulations were analyzed and if the auroral enhancement occurred in conjunction with an

Auroral Enhancement	β = .25	β = .5	β = 1	β = 2	β = 4
~7:00	**6:55**	**6:55**	**7:00**	**7:05**	**7:10**
~9:50	**9:52**	**9:44**	n/a	n/a	n/a
~11:15	**11:12**	n/a	**11:00**	**11:20**	n/a
~13:50	**13:40**	**13:50**	n/a	n/a	n/a
~14:30	**14:30**	**14:30**	**14:40**	**14:20**	14:10
~16:00	**15:58**	15:48	n/a	16:09	n/a

Table 3.1: The times of auroral enhancements during the simulation. Times shown in bold correspond with a X-line in the magnetotail. Boxes with an n/a had no enhancements around that time. Underlined times satisfy the substorm criteria.

X-line in the tail, the time in the Table 3.1 is in bold. The criteria for an extended X-line in these simulations is a velocity enhancement in the $+X$ direction (towards the earth) of at least 50 km/s and has a length of at least 10 R_E in the Y direction. The other side of the velocity enhancement has to be in the $-X$ direction. The X-line has to occur within 20 minutes of the enhancement if the time is in bold. Note that while there are often bursty bulk flows (BBF) they are mostly high X velocity enhancements that extend in the X direction, but usually have a 1-2 R_E length in Y, and often are not as long lived, but still have auroral signatures. BBF's and reconnection events that have a small extension in Y do not qualify for the established X-line criteria, and so are not included in this analysis. To help differentiate between small scale X-lines and the X-lines studied in this section, they are referred to as extended X-lines.

Figure 3.10 shows the X-Y plane of the magnetosphere for four of the simulations and shows the X velocity of the plasma. The figures show certain snapshots of time when there are significant X-lines for $\beta = .25, .5, 1$ and 2 simulations. The smaller β values have a more distinct X-line and cover a wider range in Y. The $\beta = .25$ simulation has a well defined X-line at 14:17 UT at $X = -20$ and covers from $y = 20$ to $y = -5$. The $\beta = .5$ simulation has a strong X-line at similar X distances but with not as much coverage in Y, and it has a large kink at $y = 5$.

The $\beta = 1$ simulation has an X-line further down the tail at around $X = -35$ and Y ranges from 0 to 20. Note that this snapshot of time is five minutes later than the previous simulations.

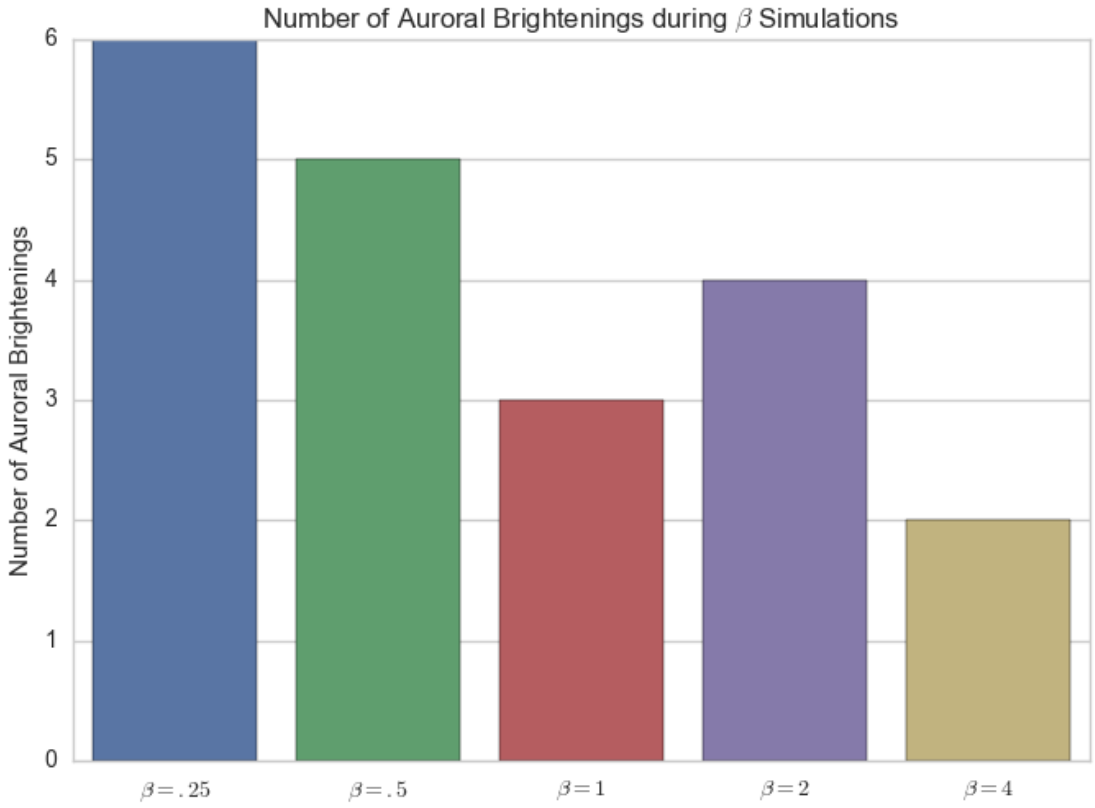

Figure 3.8: The number of auroral enhancements, identified by an increase of maximum precipitation energy flux of 1 mW/m^2 in 20 minutes, is plotted for each β simulation.

The $\beta = 2$ simulation has an X-line that fulfills the criteria at $X = -30$ and $Y = 8$ to 20 at 14:33. $\beta = 4$ does not have an X-line for this time.

Table 3.2 identifies the X-lines in the simulations that corresponded to auroral enhancements. For each simulation, every X-line that fulfills the established criteria was identified. The start and end times, the range in Y, and the average X location for each X-line were listed. The bottom row lists the X-lines that occur during times other than the auroral enhancements.

Table 3.2 also shows that as the conductivity increases the number of X-lines decrease, which changes from six X-lines for the $\beta = .25$ simulation to two X-lines during the $\beta = 4$ simulation. Most X-lines occur during the maximum enhancements but there are other X-lines that do not contribute to the maximum auroral enhancements.

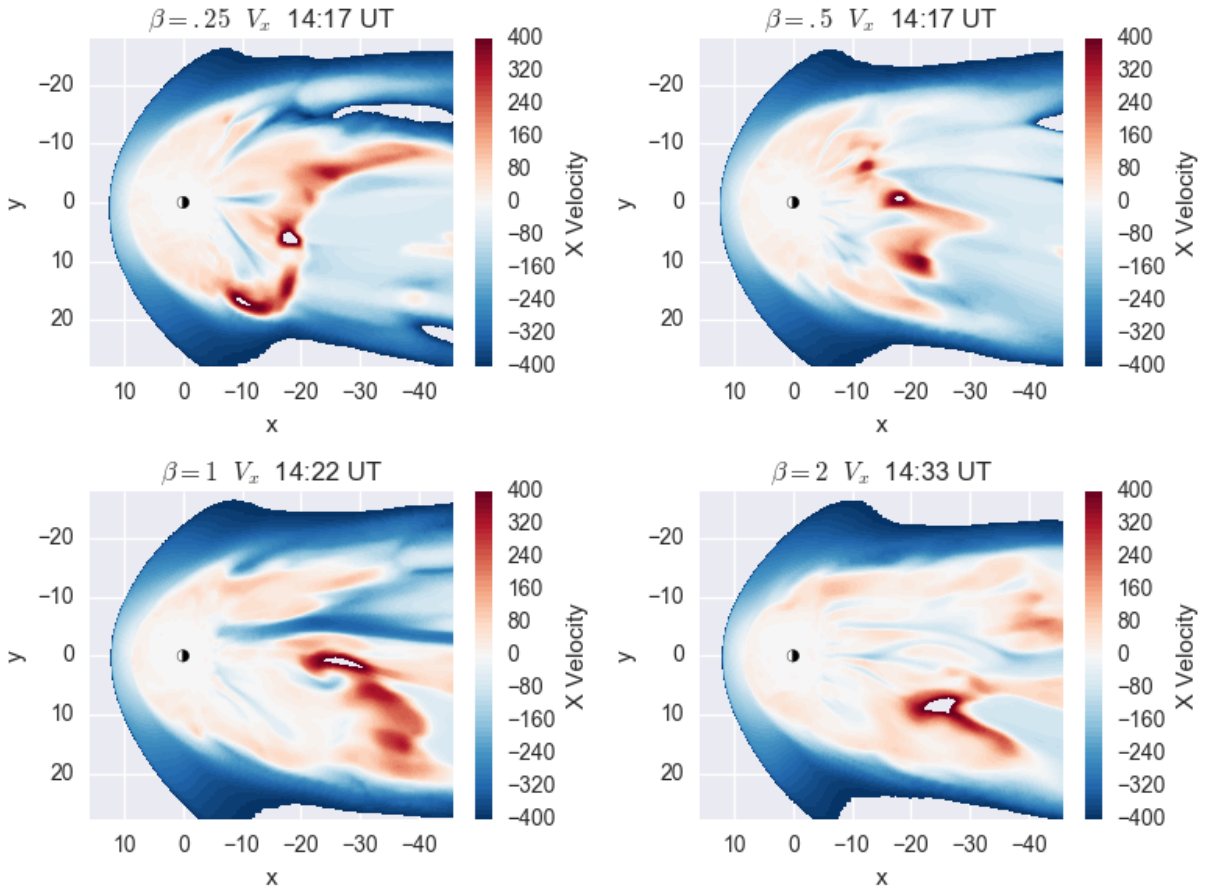

Figure 3.9: The velocity in the X direction is shown along the X-Y plane for four of the β simulations at varying times.

Twelve of the sixteen X-lines associated with auroral enhancements occur, on average, ten minutes after the initial enhancement. The other four X-lines occur before the initial enhancement. The uncertainty of the auroral enhancement time measurements is ± 5 minutes, while the X-line start and stop times are ± 2 minutes. The X-line formation occurs during the quick rise of the precipitation, sometimes extending further into the peak of the precipitation.

The total time that there are X-lines in the simulation is also included at the bottom of the table and again the trend is a decreasing one with the exception of $\beta = .5$. The first auroral enhancement is at the end of the initialization and could still have initialization effects. If the first auroral enhancement is excluded, the totals would be, 109, 99, 64, 61, and 17 minutes.

Auroral Enhancement	$\beta = .25$	$\beta = .5$	$\beta = 1$	$\beta = 2$	$\beta = 4$
~7:00	7:10-8:40 y = -10, 10 x = -10	6:59-9:05 y = -10, 10 x = -18	6:54-8:38 y = -14, 12 x = -13	7:09-8:45 y = -17, 13 x = -19	7:18-9:04 y = -15, 14 x = -19
~9:50	9:52-10:32 y = -8, 8 x = -30	9:58-11:00 y = -15, 12 x = -15	no AB no X-line	no AB no X-line	no AB no X-line
~11:15	10:52-11:03 y = -8, 8 x = -30	no AB no X-line	10:46-11:20 y = -15, 19 x = -28	10:50-11:11 y = -16, 15 x = -21	no AB no X-line
~14:00	14:03-14:32 y = -7, 20 x = -20	14:11-14:42 y = -10, 13 x = -20	14:20-14:32 y = 6, 20 x = -40	14:29-14:41 y = 7, 18 x = -35	no AB no X-line
~16:00	16:18-16:43 y = -16, 8 x = -22	no X-line	16:22-16:40 y = 0, 16 x = -27	no X-line	no AB no X-line
Other X-lines	11:38-11:42	11:47-11:49 12:20-12:24		12:30-12:58	12:35-1252
Total minutes	199	225	168	157	123

Table 3.2: The times X-lines exist that satisfy the criteria, $y > 10R_e$ at $V_x > 50km/s$. For each X-line that occurs during an auroral enhancement, the start and end time, the maximum spread in Y, and the average location in X are listed. Boxes that do not have auroral enhancements or X-lines have been noted. Underlined times correspond with the substorms. Other times where X-lines existed but not during periods of identified auroral enhancements and the total amount of time with an X-line are included at the bottom.

The data in Table 3.2 shows a comparison of the length and duration of the X-lines versus conductivity. These events are a small subset for a specific date and a much wider study will need to take place to establish a better comparison of the length and duration of the X-lines versus conductivity during substorms, but this small subset may lend some insight for a further study. Many more simulations are required to definitively state if X-line duration, extension in Y and location in X are affected by ionospheric conductance.

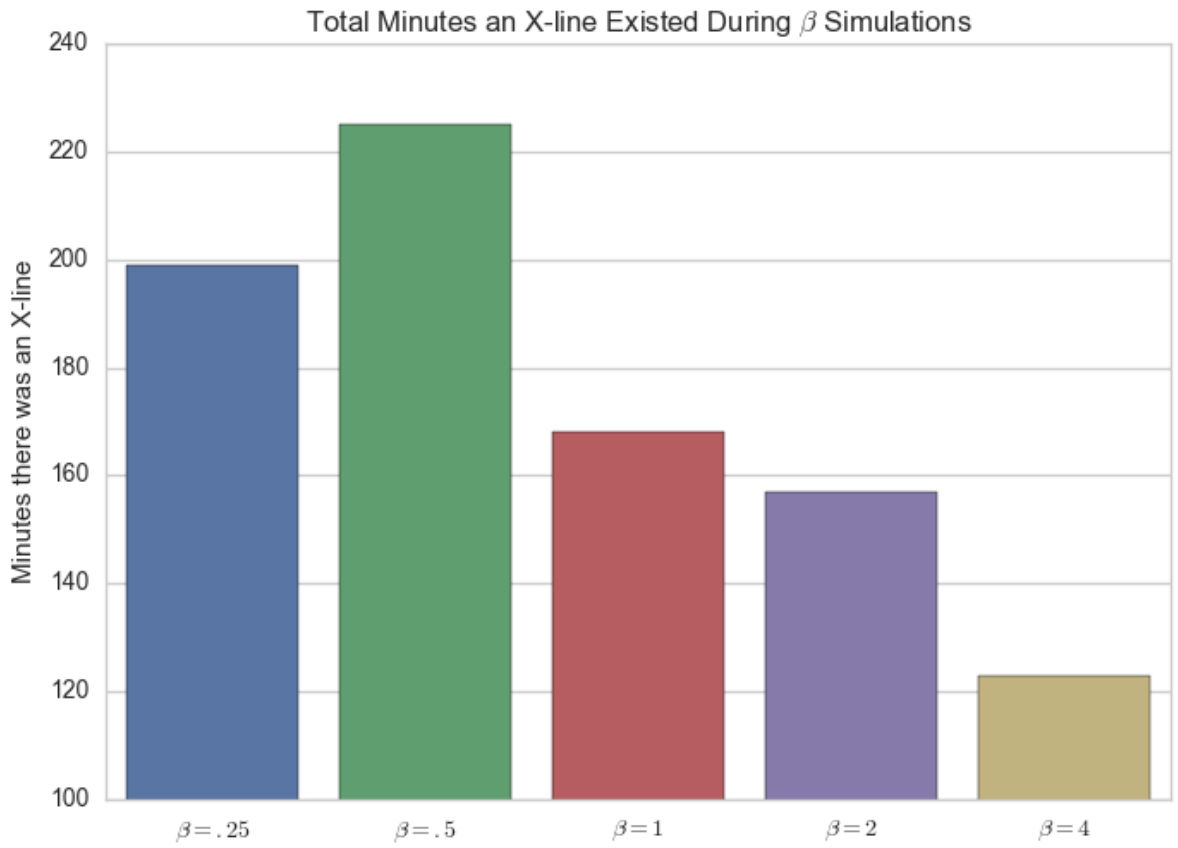

Figure 3.10: The number of minutes an extended X-line exists in the magnetotail for each β simulation is shown.

3.1.5 Discussion and Summary of Findings with β Variation

Identifying substorm timing is particularly difficult in observations and simulations, and with the different methods to identify them it is hard to determine exactly when a substorm occurs. This study has identified substorm formation by auroral intensification and by X-line formation in the tail. The main findings are listed,

1. By increasing the conductivity over the whole ionosphere, both the magnitude and frequency of substorm signatures, as identified by auroral enhancements, decrease.

2. Similarly, X-line occurrence decreases as conductivity increases. A possible explanation for this trend is the increased conductivity constricts convection in the ionosphere and magne-

tosphere (Raeder, 2003). Increased ionospheric conductance makes it harder for convection to occur, and large scale X-lines do not form as often resulting in less substorms.

3. The extended X-line duration, Y axis extent, and X location are not strongly affected by the change in conductivity. Once a substorm is triggered, whatever mechanisms that determine how energy is released and where they form, does not appear to be affected by the conductivity. Further study would be required to see if this is a general rule, or just the case for this simulation date.

4. Many similar findings shown in Chapter 2 are identified here, namely, the conductivity does play a significant role in the CPCP, and while it can affect reconnection for short time periods (hours) there is not an appreciable difference over more than ten hours on average, and the saturation effect in CPCP scales with conductivity.

These findings emphasize the importance of the ionospheric conductivity on the M-I system.

3.2 Variation of $F_{10.7}$ and Effects on Substorms

Section 3.1 showed the importance of modifying the entire ionospheric conductance on substorms, this section focuses on changing the dayside ionospheric conductance through modifying $F_{10.7}$ values that are used as a proxy in the CTIM model for the solar UV flux. Modifying $F_{10.7}$ values in CTIM changes the amount of solar UV flux entering the atmosphere on the dayside, and gives us an indication on the importance of dayside conductance to substorm frequency and magnitude. This section is in contrast to Chapter 2 which focused on nightside conductance, and Section 3.1 which changed the entire ionosphere conductance.

3.2.1 Simulation Setup

The solar wind conditions were set with a 450 km/s incoming solar wind, with no B_y or B_x component. The magnetic field was set at a static -5 B_z field with a plasma density of 7 particles/cc

and a plasma pressure of 4 nPa. The simulation is run for 24 hours. The fully coupled OpenGGCM-CTIM-RCM model with a grid size of about 16 million grid cells was used. The simulation for a spring equinox condition for the dipole to minimize hemispheric asymmetry was chosen.

$F_{10.7}$ Value	Solar Cycle Coverage
70	Solar minimum
110	Ascending and descending solar cycle values
150	Average 27-day max of solar cycle 2010-17
200	Average 27-day max of solar cycles 1976-2005
250	Highest 27-day max of solar cycles 1976-2005

Table 3.3: A table showing the values of $F_{10.7}$ selected, and when they occurred during recent solar cycles.

Table 3.3 shows the values of $F_{10.7}$ chosen to run 5 different simulations. A range of $F_{10.7}$ values that correspond to periods in the solar cycle was selected. The $F_{10.7} = 250$ value was included to show the maximum 27 day average from the big solar cycles.

Figure 3.11 shows the real 27 day averages of the $F_{10.7}$ since the dawn of the space age. The $F_{10.7}$ 27-day average illustrates the waxing and waning of the solar cycle and shows how the chosen $F_{10.7}$ values correlate with maximums, minimums, and ascending or descending slopes. The last solar cycle that peaks in 2015 was especially peculiar in that the 27-day average $F_{10.7}$ during maximum was very low. The other solar cycles centered on 1982, 1991 and 2002 show larger peaks, and according to sunspot record, are more typical. Note that some of the daily averages of $F_{10.7}$ can range up to 350.

3.2.2 Effect of Changing $F_{10.7}$ on Ionospheric Conductivity

Figure 3.12 shows the potential and conductivity profile at a snapshot at 11:21 UT. The potential is shown on the left hand panels and the Pedersen conductance is shown on the right. The potential spans from 124 kV down to 71 kV, with the $F_{10.7} = 70$ having largest potential and the higher ones smaller potentials in general.

The Pedersen conductance ranges from 39 S to 57 S over the 5 simulations which is a typical spread throughout the simulations. This spread is the smallest of all the studies in this thesis. The

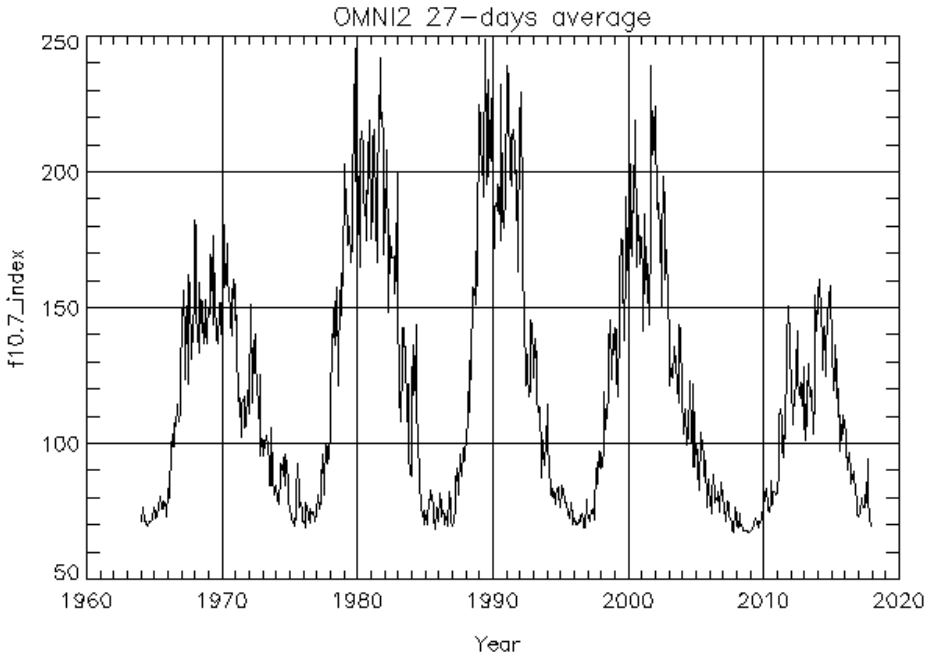

Figure 3.11: The $F_{10.7}$ 27-day average values since the dawn of the space age are graphed. This was taken from OMNI web (https://omniweb.gsfc.nasa.gov/form/dx1.html)

β study had a spread of about 90 S and the precipitation study had a spread of about 120 S for the maximum conductance. The average spread in Pedersen conductance for the $F_{10.7}$ run is not as high as the others, not because it is less important, but because of the design of the simulations.

Figure 3.13 shows the CPCP for the NH and SH for the duration of the simulations. The CPCP is much more erratic during these simulations since there is less conductance overall. As a consequence, the variability does not change as much for the $F_{10.7}$ simulations.

Figure 3.14 shows the reconnection rates calculated from both hemispheres. The reconnection rates become more bursty around 8:00 UT. Trying to identify periods where the reconnection rates peak and an associated peak in the CPCP data occurs is quite difficult, but there are some associations in the largest reconnection peaks and the CPCP.

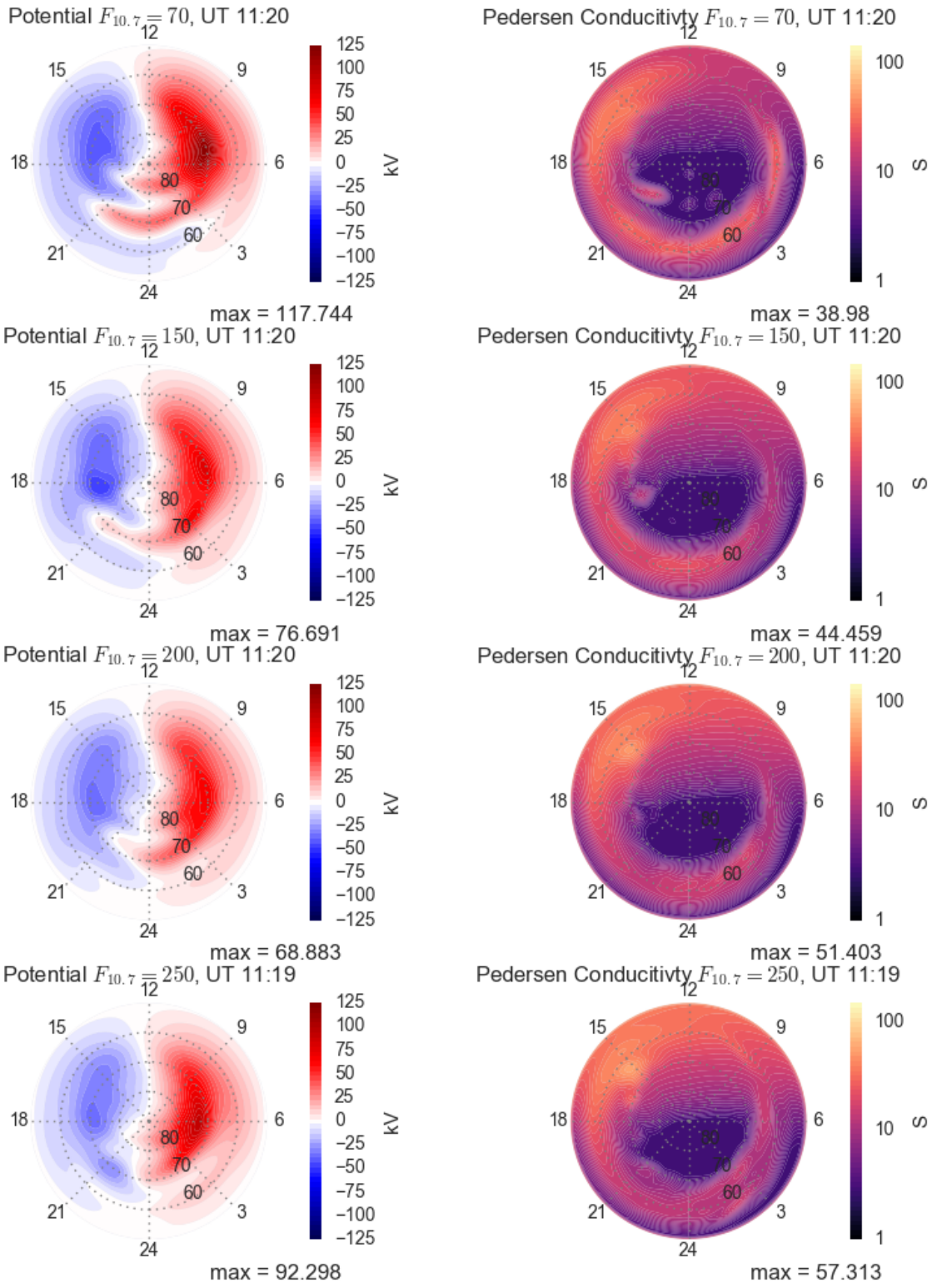

Figure 3.12: Ionospheric potential is graphed on left panels for varying $F_{10.7}$ values. The right panels contain the Pedersen conductance for the varying $F_{10.7}$ values. This snapshot of time is taken during spring equinox conditions at 11:12 after the simulation started.

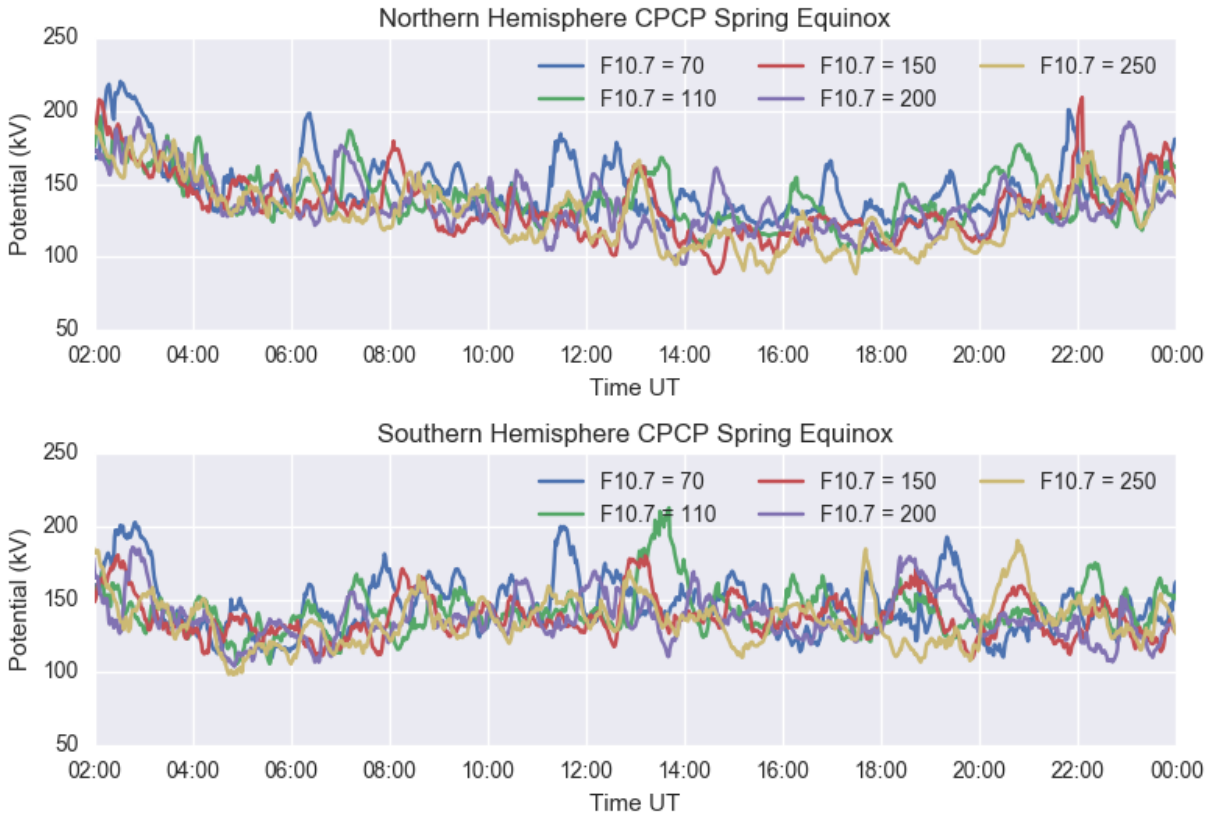

Figure 3.13: CPCP is graphed for $F_{10.7}$ values showing both the Northern and Southern Hemispheres.

Figure 3.15 shows the average CPCP and reconnection. The CPCP is greater than the reconnection rate showing that there must be something causing an increase in CPCP above the reconnection rates. Viscous interactions probably have a strong influence in these runs that have a low ionospheric conductance, permitting magnetospheric convection to proceed unhindered. The CPCP is greater than the reconnection by 25-40 kV for all the simulations. The amount of conductivity in the ionosphere for these conditions do not appear to affect the reconnection rate as much, even though it is $-5\ B_z$. By comparison the reconnection rates for the β simulations were in the 120-140 kV range. The velocity of 450 km/s and density of 7 particles per cc is a great driver for viscous interaction, which could contribute to CPCP by up to 40 kV (Bruntz et al., 2012)

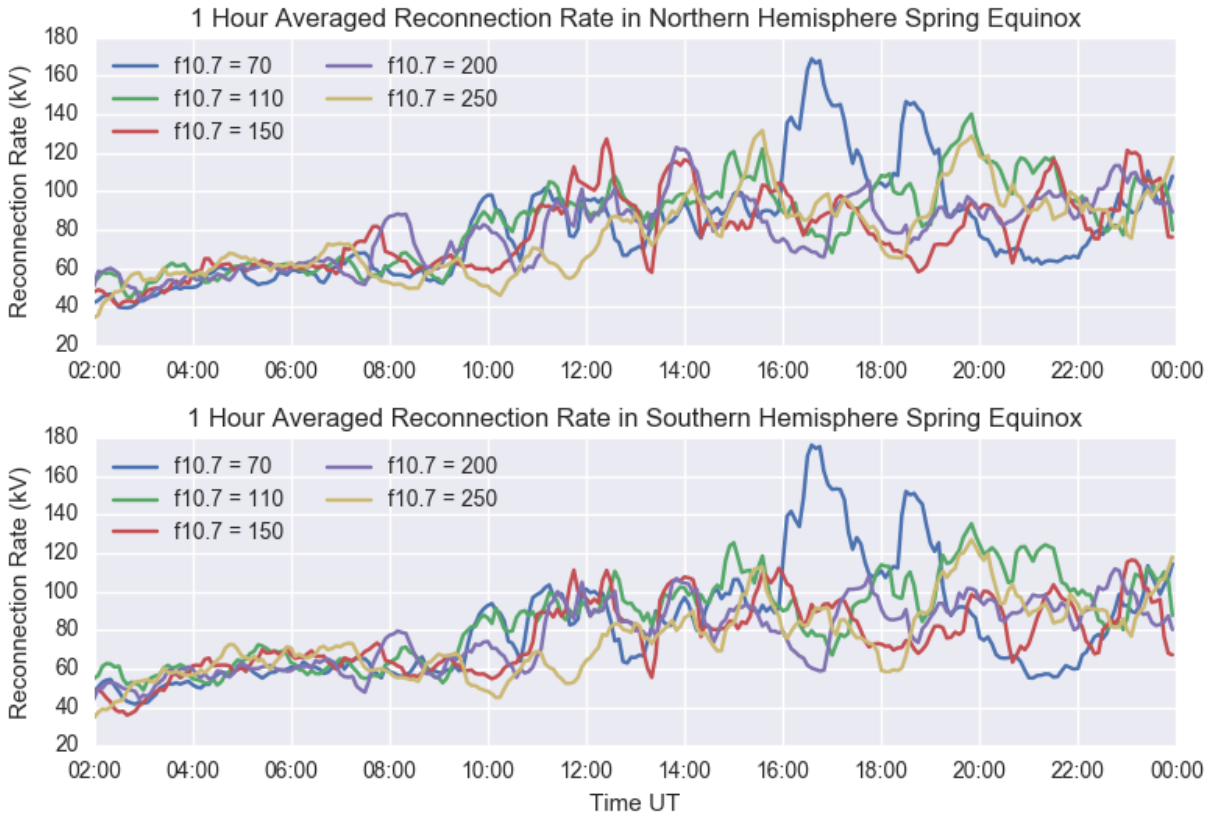

Figure 3.14: Reconnection rates are graphed from magnetic field lines originating in Northern and Southern Hemisphere using the HFB method for all five values of $F_{10.7}$.

3.2.3 Auroral Enhancement Analysis

Figure 3.16 shows the maximum precipitation of the $F_{10.7}$ simulations. The initialization of the simulation occurs for the first five hours as the simulation ramps up. The first large peak occurs at around 6:00 UT for all simulations. There appears to be some reducing of variability in the precipitation for the higher $F_{10.7}$. The lower $F_{10.7}$ simulations tend to have higher precipitation rates.

As was done for the β simulations, auroral enhancements were identified using the criteria when maximum precipitation energy flux increases by $1\ mW/m^2$ in 20 minutes. There are no auroral enhancements that pass the 80% threshold, the highest peak that occurs in the $F_{10.7} = 70$ simulation at 18:25 with in increase by 71%.

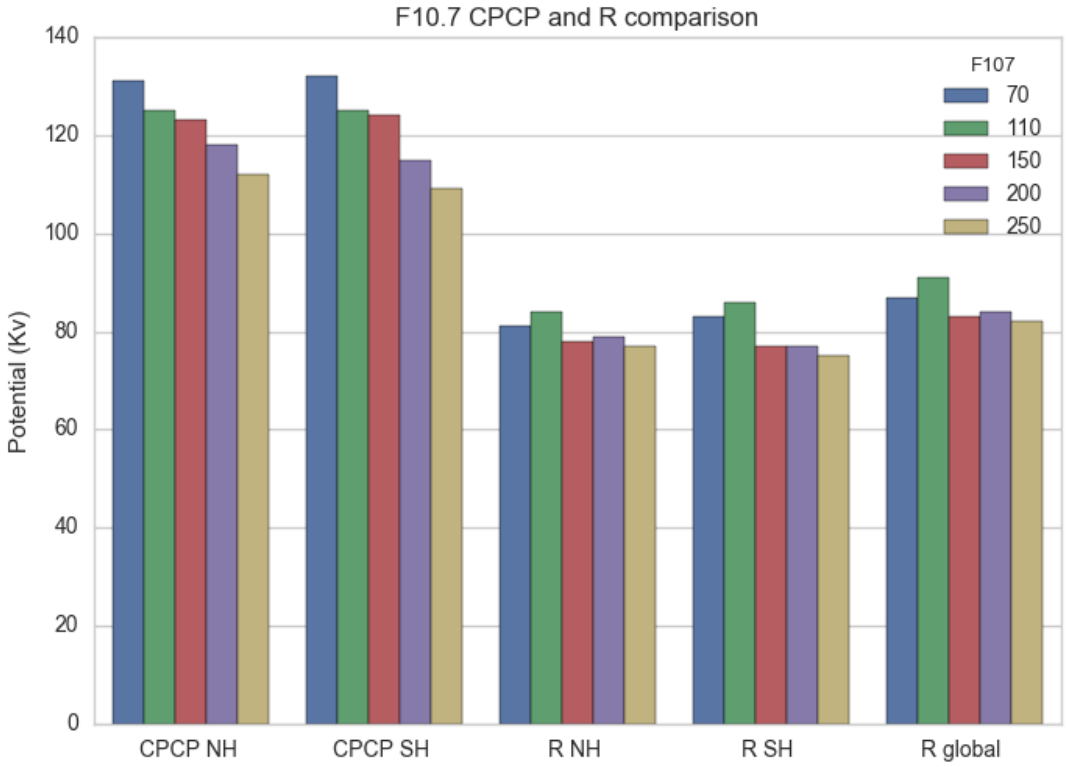

Figure 3.15: Day average for CPCP and R for spring equinox conditions.

Table 3.4 shows the auroral enhancement identified for the $F_{10.7}$ simulations using the same procedure as done for the β simulations, increase by 1 mW/m^2 There are a few enhancements that occur at similar times between the simulations. Times in Table 3.4 are in bold if an X-line occurred within 30 minutes of the enhancement, with the majority of enhancements occurring before the X-line has become established. In the β simulation as conductivity increased, the enhancements tended to decrease. For this simulation there is a slight decreasing trend as well, but the $F_{10.7}$ mostly affects the dayside conductivity, so there is not as large an effect on the nightside conductivity. Auroral enhancements were identified after 5:00, to avoid initialization effects.

None of the auroral enhancements in table 4 meet the substorm criteria where there needs to be a 80% increase within 20 minutes. None of the auroral enhancements in Table 3.4 meet this

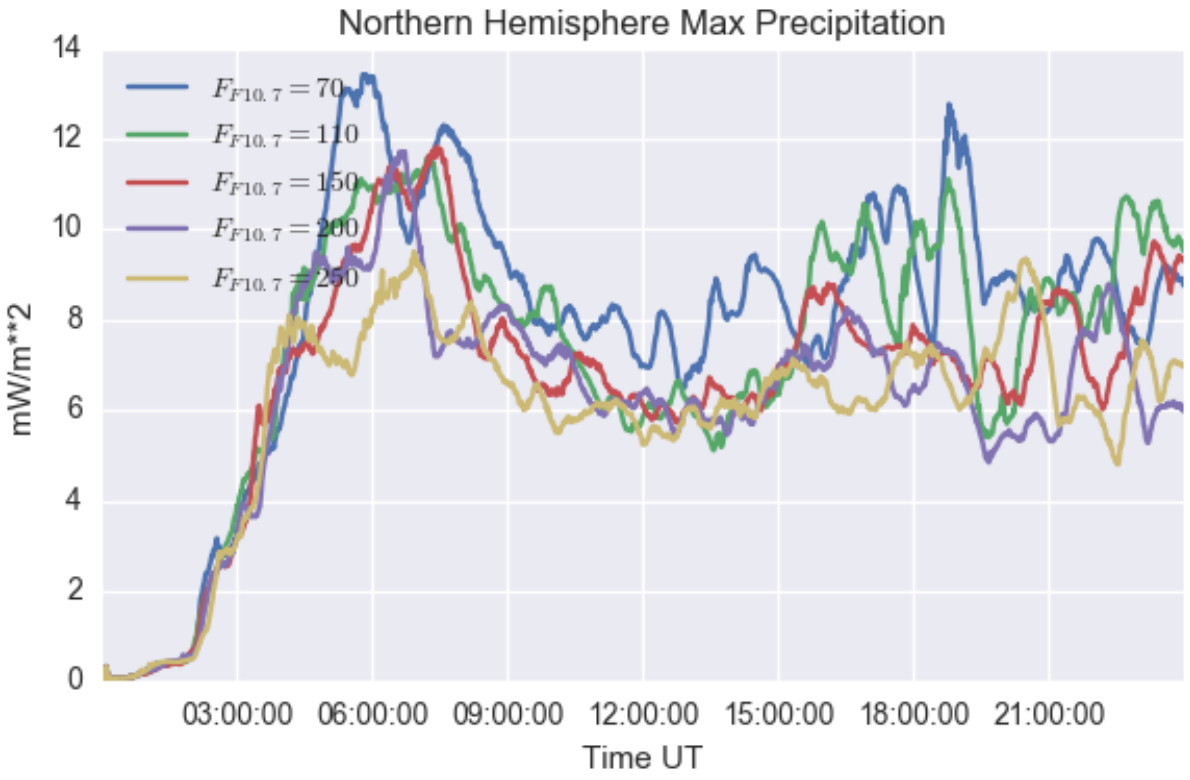

Figure 3.16: The maximum precipitation for each of the $F_{10.7}$ simulations is graphed.

criteria. There is one auroral enhancement in the $F_{10.7} = 70$ simulation at 18:25 UT that increases by 71% in 20 minutes, which has the highest precipitation energy flux increase in 20 minutes.

Figure 3.17 shows the number of auroral enhancements, and shows that there is no discernible trend that can be identified. The number of auroral enhancements does not appear affected by changes in the $F_{10.7}$. The timing and strength of auroral enhancements vary, but the total number did not change significantly in this analysis.

3.2.4 X-line Analysis for $F_{10.7}$

Table 3.5 shows the X-lines identified for the $F_{10.7}$ simulations. The total amount of time that there is an X-line identified is included at the bottom row of the table. As $F_{10.7}$ increases there is a decreasing trend in the total time of X-lines present with the exception of the $F_{10.7} = 200$ simulation. Since Table 3.2 showed that the X and Y positions of the X-lines did not have an

Auroral Enhancement	$F_{10.7}$ =70	$F_{10.7}$ =110	$F_{10.7}$ =150	$F_{10.7}$ =200	$F_{10.7}$ =250
~6:30	6:54	n/a	n/a	n/a	**5:45**
~15:20	**13:18**	**15:40**	**15:10**	**15:20**	n/a
~17:00	**16:31**	**17:47**	n/a	**17:56**	n/a
~18:30	**18:25**	**20:13**	**20:30**	**21:10**	**19:06**
~22:30	n/a	**22:20**	23:12	n/a	22:07

Table 3.4: The times of auroral enhancements during the simulation. Times shown in bold correspond with a X-line in the magnetotail. Boxes with an n/a had no enhancements around that time.

obvious trend, only the times are listed here in Table 3.5, and times that are bold are associated with the maximum auroral enhancements. X-lines in the magnetosphere should have an auroral signature, but not all of them contribute to the maximum precipitation, so some of the X-lines occur but do not give a strong enough signature to affect the maximum precipitation.

Figure 3.18 shows the total minutes

3.2.5 Summary of Effects from Changing $F_{10.7}$

Ionospheric conductivity was modifed through $F_{10.7}$ manipulation, which resulted in changes to the dayside conductance. Since the simulations used a spring equinox condition the hemispheres were equally sunlit, and hemispheric asymmetries were minimized. A summary of findings are listed.

1. $F_{10.7}$ does not have as large an affect on substorms as the β simulations, but there is a slight correlation between the frequency and magnitude of substorms.

2. While there is not a clear trend, it is clear that there are changes to the substorms and X-lines, even though $F_{10.7}$ was changing the dayside conductance. This shows that substorms are highly variable in nature, or the simulation introduces much variability.

3. Changing $F_{10.7}$ resulted in smaller changes compared to the other methods, but many of the same trends are still evident, namely, increasing conductivity decreases the CPCP, the number of auroral enhancements, substorms, and X-lines.

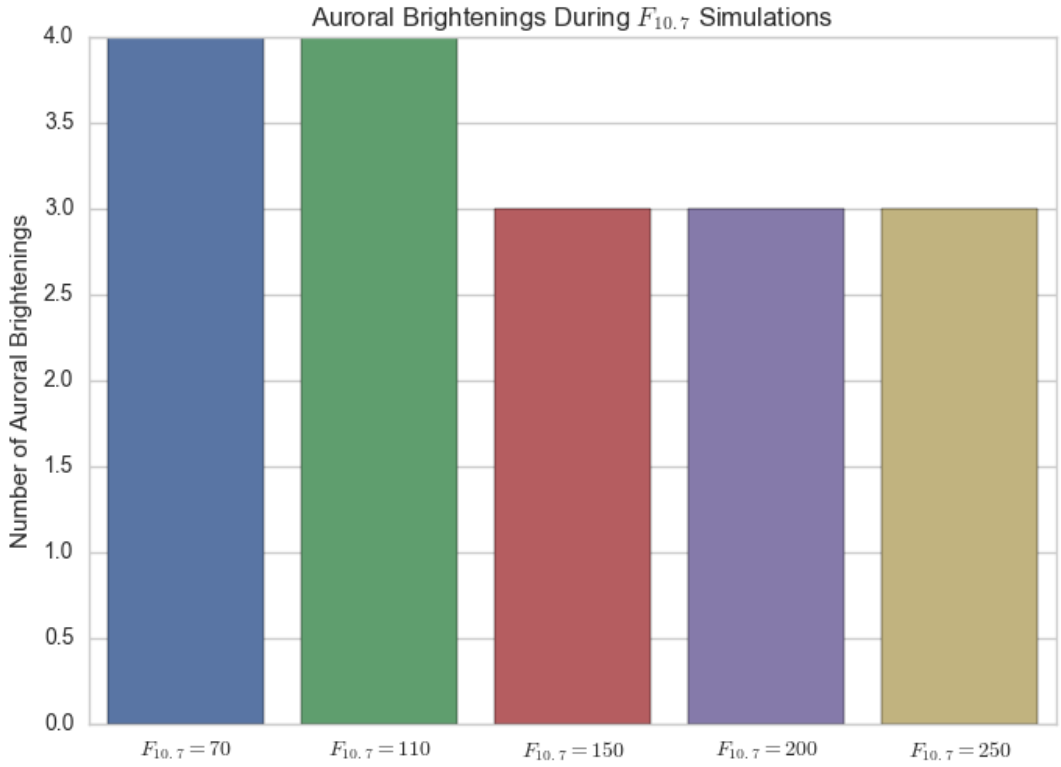

Figure 3.17: Number of auroral enhancements is shown for each of the $F_{10.7}$ simulations.

$F_{10.7}$ does not have a large affect on substorms, but to probe the possible correlation between the frequency and magnitude of substorms, section 3.3 shows some of the same β variations for 16 May 2011, simulated with $F_{10.7}$ variations.

3.3 β and $F_{10.7}$ Variation Combined

To help separate the dayside versus nightside conductivity influences on substorm strength and frequency both the β and $F_{10.7}$ were varied in the same simulations. The 16 May 2011 storm period that was used in the β study was simulated, but now the $F_{10.7}$ was varied for two values of β. Values of $\beta = .25$ and 1 were chosen. Strong auroral enhancements already existed in the $\beta = .25$ simulations, so varying $F_{10.7}$ values would help understand the trend of auroral enhance-

Auroral Enhancement	$F_{10.7}$ =70	$F_{10.7}$ =110	$F_{10.7}$ =150	$F_{10.7}$ =200	$F_{10.7}$ =250
Other X-lines	6:11-6:20 7:31-7:39 7:47-7:57 9:01-9:19 11:17-11:27 11:36-11:50 12:18-12:20 **13:48-14:16** 14:59-15:11 **16:23-16:58** 17:36-17:46 **18:53-19:20** 21:07-21:18 21:31-21:55 22:58-23:09 23:20-23:28	5:33-5:42 5:52-6:00 7:08-7:28 8:43-8:53 9:14-9:23 11:33-11:39 12:58-13:30 14:33-15:01 **16:00-16:29** **18:17-18:27** 19:28-19:39 **20:24-20:57** 21:08-21:24 21:56-22:05 23:32-23:37	5:29-5:36 7:50-8:18 10:04-10:18 11:23-11:32 12:38-13:12 13:50-14:00 14:47-15:03 **15:21-15:42** 18:17-18:33 **20:11-20:35** 21:49-22:30	5:27-5:37 6:06-6:36 6:49-7:17 8:49-9:16 10:29-10:40 11:45-12:05 13:00-13:27 14:01-14:39 **15:24-15:33** 16:50-16:57 **18:06-18:25** 20:10-20:30 **21:13-21:50** 22:45-23:03	5:20-5:33 **6:05-6:33** 8:10-8:50 11:11-11:28 12:57-13:16 14:18-14:29 16:00-16:18 17:31-17:44 **19:18-19:27** 19:58-20:10 20:24-20:48 23:29-23:40

Table 3.5: The times X-lines exist that satisfy the criteria, $y > 10R_e$ and $V_x > 50km/s$. X-line times that are bold correspond to an auroral enhancement in the ionosphere. The total number of minutes there is an X-line in the magnetosphere is included at the bottom.

ment strengthening or weakening with changing dayside conductance. The $\beta = 1$ simulation had no substorms, but since there were a few auroral enhancements that almost passed the substorm criteria, the $\beta = 1$ value was simulated to see if the auroral enhancements would strengthen with the change in $F_{10.7}$.

Four values of $F_{10.7}$ were used to simulate $F_{10.7} = 70$, 95, 170, and 250. The actual value of $F_{10.7}$ for 16 May 2011 was 95, and was the value used in section 3.1. The CPCP and reconnection rates showed the same trends that have been seen in the previous sections so that analysis has not been shown here, only substorm frequency and magnitude analysis were included.

3.3.1 Simulation $\beta = .25$ with Varying $F_{10.7}$

Figure 3.19 shows the maximum precipitation for the $\beta = .25$ simulations with varying $F_{10.7}$. Since $\beta = .25$, the resultant conductivity due to photoionization is reduced by .25, so the effects from changing $F_{10.7}$ is further reduced. The $F_{10.7} = 95$ simulation is the one shown during the

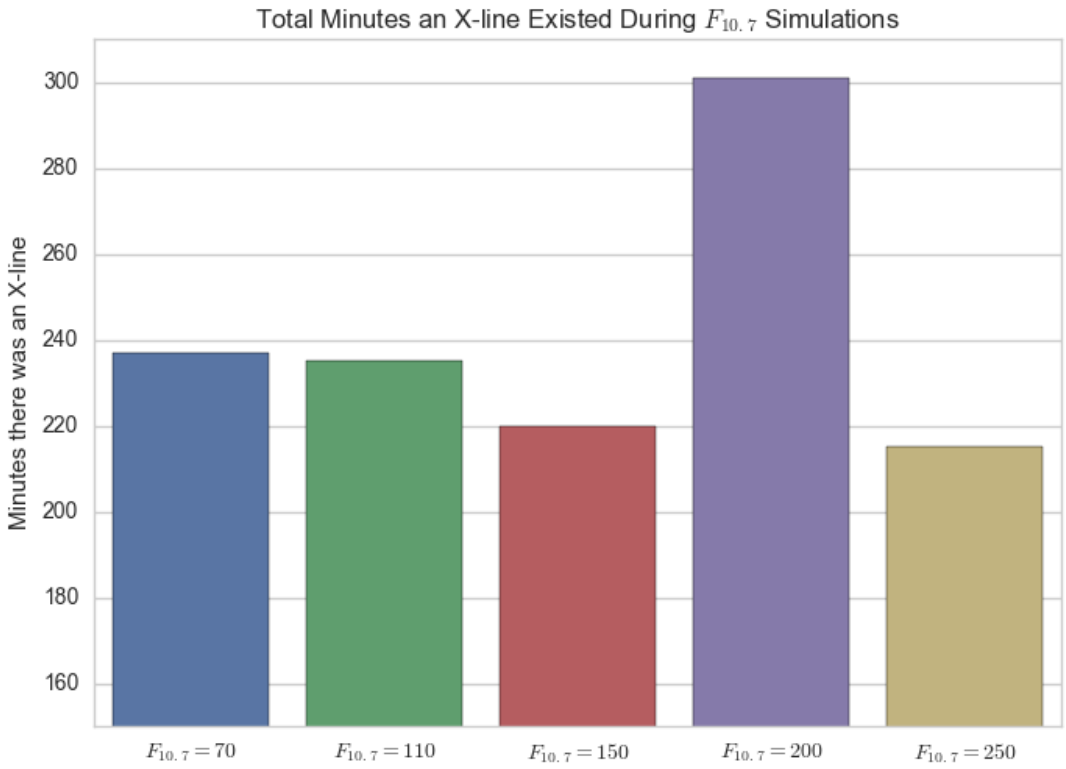

Figure 3.18: The maximum precipitation for each of the $F_{10.7}$ simulations is graphed.

β analysis and has substorms signatures at 9:52 and 11:12. The $F_{10.7} = 70$ simulation does not have any substorm signatures, there are some auroral enhancements that occur at similar times, but the magnitude is smaller than the $F_{10.7} = 95$ simulation. The $F_{10.7} = 170$ simulation mimics the $F_{10.7} = 95$ simulation most closely and has substorms that occur at similar times. The $F_{10.7} = 250$ has auroral enhancements that occur at similar times, but the magnitude of precipitation is the least of the four simulations. The trend of increasing $F_{10.7}$ leads to less precipitation, is somewhat evident here.

Table 3.6 shows the substorms identified, and also included for reference are the strong auroral enhancements that increase by more than 60% in 20 minutes. The sum of the maximum precipitation was also included on the bottom row, as another measure to compare between simulations. This trend shows that for the most part the precipitation decreases as the $F_{10.7}$ increases, but the

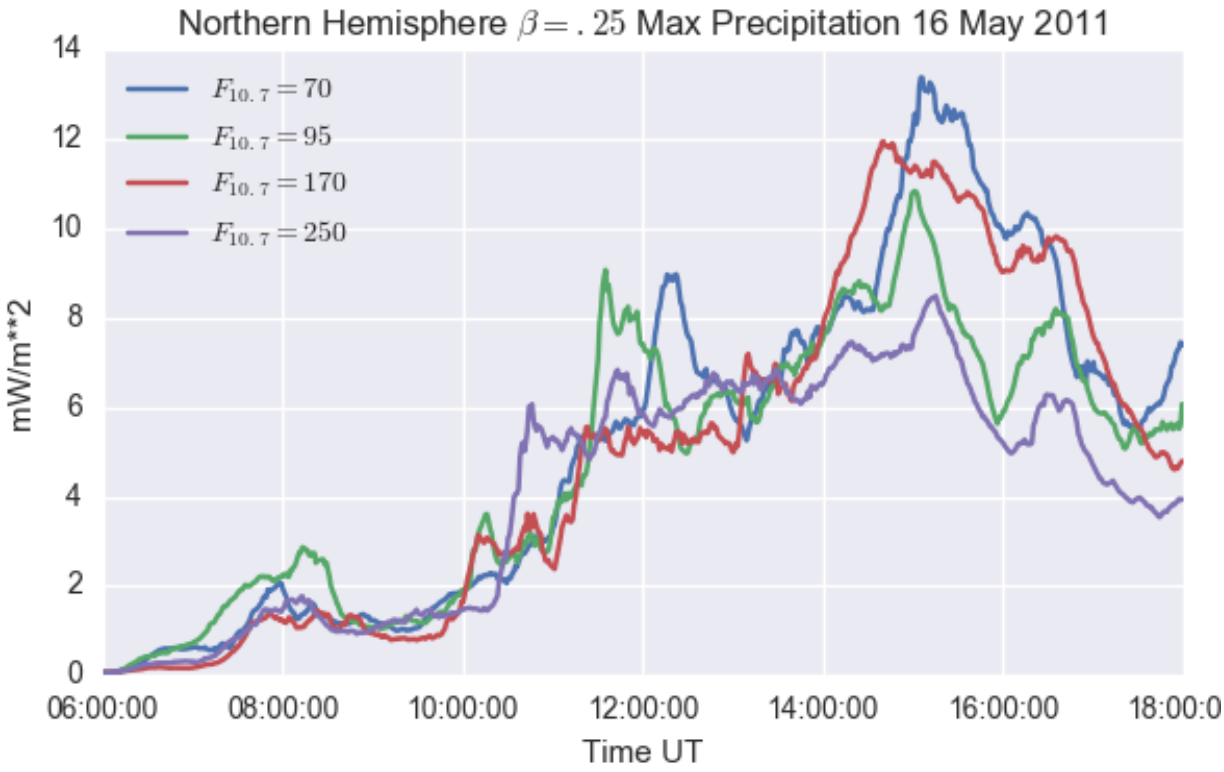

Figure 3.19: Maximum precipitation with conductivity modified at $\beta = .25$ and the ionizing radiation modified by four different $F_{10.7}$ values.

variation is small and not always consistent. The inverse relationship that was once easily identified in the β simulations, is not as clear. Possible reasons for the difficulty could be due to the dayside conductivity not having a large influence, because $F_{10.7}$ mostly affects the dayside, and then the $\beta = .25$ further limits the effects of the $F_{10.7}$ modifications. It could also be that the range of $F_{10.7}$ studied is not sufficient to identify trends.

3.3.2 Simulation $\beta = 1$ with Varying $F_{10.7}$

Figure 3.20 shows the maximum precipitation for $\beta = 1$, while varying $F_{10.7}$. Table 3.7 shows the identified substorms and also the auroral enhancements that increase by at least 60% in 20 minutes. The $F_{10.7} = 95$ simulation was shown previously and there is only one substorm present at 6:48. There is an auroral enhancement that increases by 60% in 20 minutes at 9:39 that is at the

Substorm	$F_{10.7} = 70$	$F_{10.7} = 95$	$F_{10.7} = 170$	$F_{10.7} = 250$
~7:00	7:24	7:02	7:16	7:12
~10:00	9:30 (67%)	9:52	9:48	8:54 (62%)
~11:10	10:57 (69%)	11:12	11:00	10:18
Sum	3751	3432	3520	2970

Table 3.6: The times of substorms identified for the $\beta = .25$ run with varying $F_{10.7}$ that increase by 80% within 20 minutes. Auroral enhancements that did not meet the substorm criteria, but passed the 60% threshold are also included for reference, with their respective percentage increases.

start of the slowly rising precipitation from 9:40 to 12:00. In contrast, the $F_{10.7} = 70$ simulation does have a substorm at 10:35, and while all the other simulations do have an increase at the same time they do not increase by 80% within 20 minutes. There may be a weak trend of decreasing precipitation as $F_{10.7}$ increases which was seen more clearly in the β simulations.

The $F_{10.7} = 70$ simulation has the highest sum of the maximum precipitation by a significant margin, the others are at about the same level. The variation of the substorm magnitude is difficult to ascertain since there are not many substorm events. In each simulation a substorm occurs at the start of the simulation, and then the $F_{10.7} = 70$ has an additional substorm at 10:35. More substorms in the lower $F_{10.7}$ simulation could hint at the trend of increasing conductivity decreases the substorm magntidue, since the $F_{10.7} = 95$ simulation has an auroral enhancement earlier that increases 63%, and then also has a much slower increase in precipitation at the same time as the substorm.

Substorm	$F_{10.7} = 70$	$F_{10.7} = 95$	$F_{10.7} = 170$	$F_{10.7} = 250$
~7:00	7:19	6:48	6:20	6:56
~10:35	10:35	9:39 (63%)	n/a	10:32 (69%)
Integral	2675	1945	2133	1915

Table 3.7: The times substorms are identified for the $\beta = 1$ runs with varying $F_{10.7}$ that increase by 80% within 20 minutes.

3.3.3 Summary of β and $F_{10.7}$ Variation

The main results from the modification of both $F_{10.7}$ and β are,

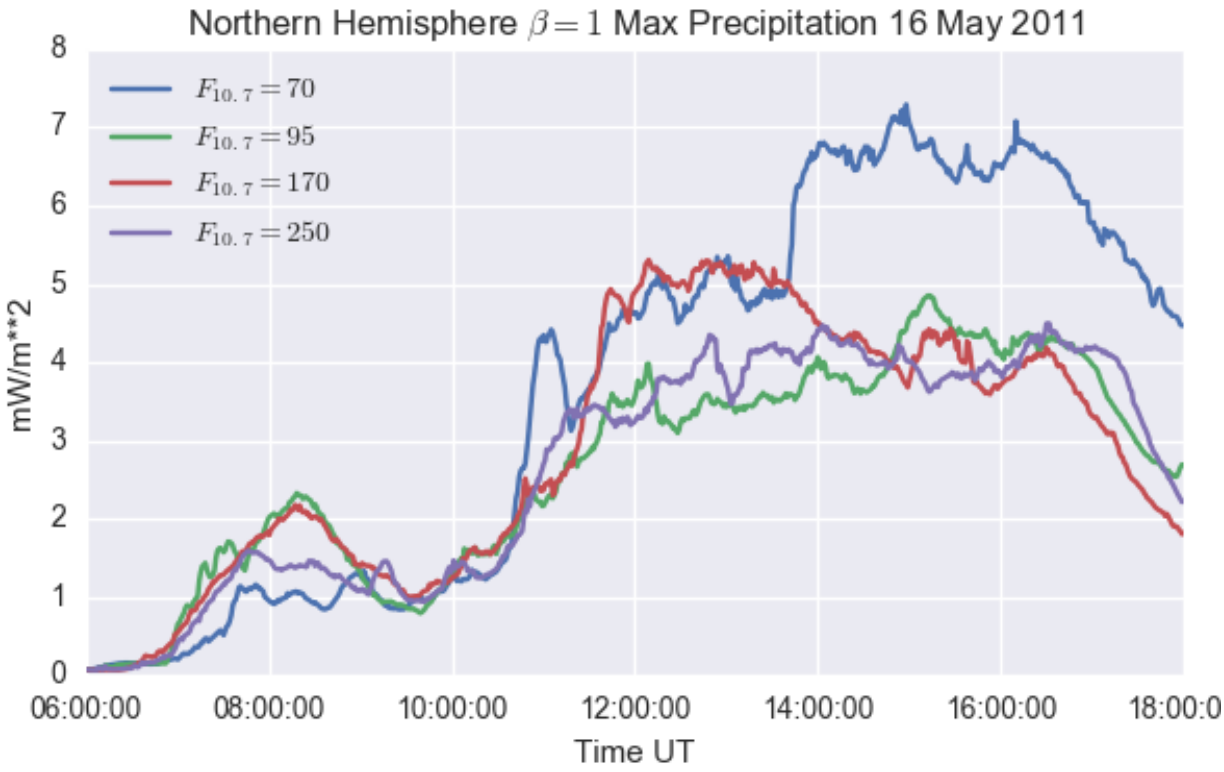

Figure 3.20: Maximum precipitation with conductivity modified at $\beta = 1$ and the ionizing radiation modified by four different $F_{10.7}$ values.

1. Even though $F_{10.7}$ does not have a strong correlation with the total number of auroral enhancements, but the timing of auroral enhancements changes. There have been studies to probe how chaotic the M-I system is, and these results may lend some strength to those arguments (Horton et al., 1999).

2. The trend of increased conductivity results in lower frequency of substorms by varying $F_{10.7}$ is not evident, but there is variation in the timing of substorms. This variation hints at some chaotic nature of substorms in the simulation.

3. There is a weak correlation of higher $F_{10.7}$ causing lower magnitude substorms, and precipitation. The higher ionospheric conductivity constricts the magnetospheric convection, which

results in slower rise times of the maximum precipitation. Both the decrease and slower rise of precipitation prevent the event to qualify as a substorm.

The possible mechanism whereby $F_{10.7}$ could control substorms is, that the dayside conductance modifies the dayside reconnection rate, which then influences the tail lobe energy loading, this affects magnitude and frequency of substorm energy release in the tail.

3.4 Discussion and Comparison to Other Works

Borovsky et al. (2009) did a study of the effects of Pedersen conductance on the saturation of the CPCP. They did this using the Block-Adaptive-Tree Solarwind Roe Upwind Scheme (BATS-R-US) a magnetohydrodynamic code that simulates the geospace environment from Michigan (Powell et al., 1999; Gombosi et al., 2002). Borovsky et al. (2009) did not use a coupled ionosphere/thermosphere code. In this version of BATS-R-US a flat height integrated Pedersen conductance was used over the entire ionosphere starting at a value of 5 S and then slowing increasing the conductance to 20 S, then they looked at the changes to the system. They kept Hall conductance at zero during the whole simulation. They used a resistive spot on the nose of the magnetopause to capture the correct reconnection rate.

A summary of the results from Borovsky et al. (2009) are included in Table 3.8, a reproduction of their table 4. A direct comparison of all results identified by Borovsky et al. (2009) was not undertaken. The items in bold are results that are directly compared in this thesis.

The three items in bold that are influenced by increasing Pedersen conductance found by Borovsky et al. (2009) were shown similarly in chapter 2. In this thesis three different methods were used to vary the ionospheric conductance, and it was found that CPCP decreased for each method.

Borovsky et al. (2009) also found that the dayside reconnection rate remained the same. They stated, "The reconnection rate at the magnetopause is governed by four plasma parameters at the magnetopause (Borovsky, 2008): the magnetic field strength B_m on the magnetospheric side, the

Property influenced by increasing Σ_P	Possible Reason
Cross-polar cap potential reduced	Solar wind cannot deliver current
E_y reduced over polar cap	Mapping of reduced polar cap potential
$V_\perp$ reduced over polar cap	Mapping of reduced polar cap potential
Cross-polar cap currents increase	Ionospheric resistivity is lowered
Dayside magnetic field weakens	Perturbation from polar currents
Magnetopause at nose moves inward	Weakening of dayside field
B_x increases over the polar cap	Perturbation from polar currents
Cusp shifts sunward	Weakening of dayside field
Closed field line region flattens on dayside	Weakening of dayside field
Property not influenced by increasing Σ_P	**Possible Reason**
Geometrical factor $I_{total}/\Sigma_P\Delta_{\phi_{pc}}$ unchanged	Perturbation from polar currents
Dayside reconnection rate unchanged	Weakening of dayside field
Cross-magnetosphere potential unchanged	Perturbation from polar currents
Magnetopause magnetic field strength constant	Weakening of dayside field
Flaring at terminators does not change significantly	Weakening of dayside field

Table 3.8: The results found by Borovsky et al. (2009) when they increased Pedersen conductance. Borovsky et al. (2009) table 4 reproduced here.

magnetic field strength B_s on the magnetosheath side, the plasma mass density ρ_m on the magnetospheric side, and the plasma mass density ρ_s on the magnetosheath side. In order to change the reconnection rate at the dayside magnetosphere something must act to change those local plasma parameters. In the simulations, no physical processes that could change those parameters is observed."(Borovsky et al., 2009)

In this study the reconnection rate was observed to change on short times scales, hours, but the average reconnection rate over tens of hours remained the same. The Borovsky et al. (2009) study used ideal solar wind conditions without being coupled to a ionosphere/thermosphere model, and they only measured the dayside reconnection rate, whereas this thesis includes the global reconnection rate. Thus the larger variation that occurs in this thesis is probably a result of the nightside reconnection that is dominated by substorms and other bursty reconnection events.

Merkin et al. (2005) did a study of the cross polar cap saturation effect using the Lyons-Fedder-Mobury (LFM) MHD model (Fedder et al., 1995, 1998; Lyon et al., 2004). They ran 14 simulations with a height integrated Pedersen conductance of 5 S and 10 S for the entire ionosphere, and with 7 values of solar wind E_y ranging from 4 mV/m to 16 mV/m. Hall conductance was set to zero. Merkin et al. (2005) did not use LFM with a coupled ionosphere-thermosphere code.

Merkin et al. (2005) found that as the solar wind E_y was increased the CPCP increased up to a saturation point, that decreased as the conductance increased. They calculated reconnection rate by integrating the parallel electric field along the two magnetic field lines at the loci of the extrema of the electrostatic potential on the inner boundary of the simulation.

The results found by Merkin et al. (2005) showed that as the conductance was increased, the flanks of the magnetosphere widened causing the bowshock to move sunward, causing the magnetosheath flow to be reconfigured. This reconfiguration caused the dayside magnetic reconnection to be reduced resulting in a saturation effect. Merkin et al. (2005) claimed that while the reconnection rate was slightly higher than the CPCP this was a result of the potential drops along magnetic fields and that the CPCP and reconnection rates should be the same.

Lotko et al. (2014) used LFM model to look at nightside reconnection rates, and how they are affected by Hall conductance. They ran 3 simulations using a uniform ionospheric conductance, an empirical-causal conductance, and a Hall depletion conductance where the Hall conductance is removed in a band in the auroral oval. They calculated magnetic reconnection by integrating the amount of flux that passed through the mapped open-closed boundary in the tail. They found that the Hall conductance has an important role in regulating the location of reconnection and resultant plasma flows in the tail. They showed that the meridional gradient in the Hall conductance causes more reconnection flows to occur in the premidnight sector. They also found that the reconnection rate and CPCP were comparable for the duration of the simulation.

The methods of this thesis differ from the methods of Borovsky et al. (2009),Merkin et al. (2005), and Lotko et al. (2014) by;

1. OpenGGCM uses coupled ionosphere-thermosphere and ring current model in these simulations that provide two-way feedback. Whereas the three studies use a MHD simultion that is not coupled to ionosphere/thermosphere codes.

2. The conductance for this thesis is modified in three different ways; modifying precipitation, modifying the entire conductance, and changing the F10.7 proxy input into the CTIM model. The methods used in the other papers were uniform conductance, with the Lotko et al. (2014) method using an empirical conductance pattern for one of their simulations.

3. All three previous studies use ideal solar wind conditions that do not change during the run. in this thesis real solar wind data is used that can be highly variable.

4. The previous studies use the BATS-R-US and the LFM models. This thesis uses OpenGGCM.

In addition to comparing with observational data, it is important to compare results with other models. Having multiple models that are applying MHD equations in different ways to the geospace system, can help recognize if a phenomena is a peculiarity of the model, or accurately predicting a real phenomena. The results of this thesis compare well with some of the results of the previous studies, and differ with some of them, namely;

1. The results of Borovsky et al. (2009) and Merkin et al. (2005) showed that increasing the ionospheric conductance reduced the CPCP, and it has similarly been reported in many simulation studies (Bruntz et al., 2012; Nagatsuma, 2004; Siscoe et al., 2002). The reduction in CPCP was reproduced in this thesis. Lotko et al. (2014) modified Hall conductance, which does not have a large effect on the magnitude of the CPCP, but can determine the orientation asymmetry of the reconnection flows in the tail.

2. Borovsky et al. (2009) claimed that the reconnection rates did not change and were not always the same as the CPCP, while Merkin et al. (2005) claimed that the reconnection rates did change and were the same value as the CPCP. There could be some discrepancy between

reconnection rates and CPCP because the methods that the authors use to calculate their reconnection rates are different. The results of this thesis most closely align with those of Borovsky et al. (2009). It was found that on large time scales the reconnection does not change, and that the CPCP and reconnection rates can be different for certain simulations.

3.5 Chapter Summary and Future Work

At Mercury, which does not have an ionosphere, substorms are occurring very rapidly, every 1-10 minutes (Slavin et al., 2007). In addition to having no ionosphere, Mercury is closer to the sun so has higher solar wind density, and does not rotate, these all contribute to magnetospheric convection evolving very rapidly. In simulations of the earth, as the conductivity of the ionosphere decreases the convection in the magnetosphere is more rapid resulting in more substorm activity and X-line formation.

The ionospheric conductivity is an important part of the M-I system. It has been shown that the conductivity, especially the nightside conductivity, is an important factor to consider for particle precipitation, CPCP, reconnection rates, both substorm frequency and magnitude, and X-line formation in the earth's magnetotail. The $F_{10.7}$ index mostly affects the dayside, and while it has contributions to the CPCP and precipitation, the effect on substorms and X-line formation is not as strong as the nightside conductance, but since there are still some changes in substorms it hints at a potential chaotic nature in the system.

Future work that could build upon this dissertation would be,

1. Run the substorm analysis on the precipitation data from Chapter 2. This could be beneficial in isolating the changes to nightside conductivity and their resultant effects.

2. Probe the variability of the system by running simulations with just slight changes in the initial conditions and see how sensitive the simulation is to initial conditions, and the resultant changes to substorms.

3. Determine whether there may be any correlations between where X-lines are forming in the tail and how long they last, and the ionospheric conductivity. These data hint at a relationship, but it is not clear.

4. Understanding the effects on the ionospheric current system would help show how the region 1 and region 2 currents close, and the effects of the ionospheric conductance on current closure.

5. Ion outflow is another way the ionosphere can control the magnetosphere. It would be valuable to see how ionospheric conductivity is influenced by, and/or influences ion outflow.

BIBLIOGRAPHY

R. C. Allen, S. A. Livi, S. K. Vines, J. Goldstein, I. Cohen, S. A. Fuselier, B. H. Mauk, and H. E. Spence. Storm time empirical model of O+ and O6+ distributions in the magnetosphere. *Journal of Geophysical Research: Space Physics*, 122(8):8353–8374, 2017. ISSN 21699402. doi: 10.1002/2017JA024245.

W. I. Axford. Viscous interaction between the solar wind and the earth's magnetosphere. *Planetary and Space Science*, 12(1):45–53, 1964. doi: https://doi.org/10.1016/0032-0633(64)90067-4.

W I Axford and C O Hines. a Unifying Theory of High-Latitude Geophysical Phenomena and Geomagnetic Storms. *Canadian Journal of Physics*, 39(10):1433–1464, 1961. ISSN 0008-4204. doi: 10.1139/p61-172.

W. Baumjohann, G. Paschmann, and C. A. Cattell. Average plasma properties in the central plasma sheet. *Journal of Geophysical Research: Space Physics*, 94(A6):6597–6606, 1989. ISSN 01480227. doi: 10.1029/JA094iA06p06597.

L. Biermann. Kometenschweife und solare Korpuskularstrahlung. *Zeitschrift fur Astrophysik*, 29: 274–286, 1951.

J P Boris. A physically motivated solution of the Alfven problem. *NRL memorandum*, (2167), 1970.

Joseph E. Borovsky. The rudiments of a theory of solar wind/magnetosphere coupling derived from first principles. *Journal of Geophysical Research: Space Physics*, 113(8):A08228, 2008. ISSN 21699402. doi: 10.1029/2007JA012646.

Joseph E. Borovsky, Benoit Lavraud, and Maria M. Kuznetsova. Polar cap potential saturation, dayside reconnection, and changes to the magnetosphere. *Journal of Geophysical Research: Space Physics*, 114(3):A03224, 2009. ISSN 21699402. doi: 10.1029/2009JA014058.

Stephen H. Brecht. Global simulations using MHD codes: A few points to consider before you try one. *Space Science Reviews*, 42(1-2):169–185, 1985. ISSN 00386308. doi: 10.1007/BF00218231.

R. Bruntz, R. E. Lopez, M. Wiltberger, and J. G. Lyon. Investigation of the viscous potential using an MHD simulation. *Journal of Geophysical Research: Space Physics*, 117(3), 2012. ISSN 21699402. doi: 10.1029/2011JA017022.

P. A. Cassak and M. A. Shay. Scaling of asymmetric magnetic reconnection: General theory and collisional simulations. *Physics of Plasmas*, 14(10):102114, 2007. ISSN 1070664X. doi: 10.1063/1.2795630.

F V Coroniti and C F Kennel. Can the ionosphere regulate magnetospheric convection? *Journal of Geophysical Research*, 78(16):2837–2851, 1973. ISSN 2156-2202. doi: 10.1029/JA078i016p02837.

A. E. Covington. Micro-Wave Solar Noise Observations During the Partial Eclipse of November 23, 1946. *Nature*, 159:405–406, 1947. ISSN 00280836. doi: 10.1038/159405a0.

S. W H Cowley. The causes of convection in the Earth's magnetosphere: A review of developments during the IMS. *Reviews of Geophysics*, 20(3):531–565, 1982. ISSN 19449208. doi: 10.1029/RG020i003p00531.

W. D. Cramer, J. Raeder, F. R. Toffoletto, M. Gilson, and B. Hu. Plasma sheet injections into the inner magnetosphere: Two-way coupled OpenGGCM-RCM model results. *Journal of Geophysical Research: Space Physics*, 122(5):5077–5091, 2017. ISSN 21699402. doi: 10.1002/2017JA024104.

John C. Dorelli, Michael Hesse, Maria M. Kuznetsova, Lutz Rastaetter, and Joachim Raeder. A new look at driven magnetic reconnection at the terrestrial subsolar magnetopause. *Journal of Geophysical Research: Space Physics*, 109(A12), 2004. ISSN 21699402. doi: 10.1029/2004JA010458.

J. W. Dungey. Interplanetary magnetic field and the auroral zones. *Physical Review Letters*, 6(2):47–48, 1961. ISSN 00319007. doi: 10.1103/PhysRevLett.6.47.

C. R. Evans and J. F. Hawley. Simulation of magnetohydrodynamic flows : A constrained transport method. *The Astrophysical Journal*, 332(2):659–677, 1988. ISSN 0004-637X. doi: 10.1086/166684.

Charles J. Farrugia, Fausto T. Gratton, and Roy B. Torbert. Viscous-type processes in the solar wind-magnetosphere interaction. *Space Science Reviews*, 95(1-2):443–456, 2001. ISSN 00386308. doi: 10.1023/A:1005288703357.

J. A. Fedder and J. G. Lyon. The solar wind-magnetosphere-ionosphere current-voltage relationship. *Geophysical Research Letters*, 14(8):880–883, 1987. ISSN 00948276. doi: 10.1029/GL014i008p00880.

J. A. Fedder, S. P. Slinker, J. G. Lyon, and R. D. Elphinstone. Global numerical simulation of the growth phase and the expansion onset for a substorm observed by Viking. *Journal of Geophysical Research*, 100(A10):19083, 1995. ISSN 0148-0227. doi: 10.1029/95JA01524.

J A Fedder, S P Slinker, and J G Lyon. A comparison of global numerical simulation results to data for the January 27–28, 1992, Geospace Environment Modeling challenge event. *J. Geophys. Res.*, 103(A7):14799–14810, 1998. ISSN 21699402. doi: 10.1029/97ja03664.

Banafsheh Ferdousi. *The Study of Magnetotail Dynamics and Their Ionospheric Signatures Using Magnetohydrodynamic Simulation Model: OpenGGCM*. PhD thesis, University of New Hampshire, 2017.

T. G. Forbes. The nature of Petschek-type reconnection. *Earth, Planets and Space Planets and Space*, 53:423–429, 2001. doi: https://doi.org/10.1186/BF03353252.

T. J. Fuller-Rowell, D. Rees, S. Quegan, R.J. Moffett, M.V. Codrescu, and G. H. Millward. A Coupled Thermosphere-Ionosphere Model (CTIM). In R.W. Schunk, editor, *Solar Terrestrial Energy Programme (STEP) Handbook*, pages 217–238, NOAA/NGDC, Boulder, Colorado, 1996. Scientific Committee on Solar Terrestrial Physics (SCOSTEP).

N. Y. Ganushkina, M. W. Liemohn, S. Dubyagin, I. A. Daglis, I. Dandouras, D. L. De Zeeuw, Y. Ebihara, R. Ilie, R. Katus, M. Kubyshkina, S. E. Milan, S. Ohtani, N. Ostgaard, J. P. Reistad, P. Tenfjord, F. Toffoletto, S. Zaharia, and O. Amariutei. Defining and resolving current systems in geospace. *Annales Geophysicae*, 33(11):1369–1402, 2015. ISSN 14320576. doi: 10.5194/angeo-33-1369-2015.

A. Glocer, J. Dorelli, G. Toth, C. M. Komar, and P. A. Cassak. Separator reconnection at the magnetopause for predominantly northward and southward IMF: Techniques and results. *Journal of Geophysical Research A: Space Physics*, 121(1):140–156, 2016. ISSN 21699402. doi: 10.1002/2015JA021417.

Tamas I. Gombosi, Gábor Tóth, Darren L. De Zeeuw, Kenneth C. Hansen, Konstantin Kabin, and Kenneth G. Powell. Semirelativistic magnetohydrodynamics and physics-based convergence acceleration. *Journal of Computational Physics*, 177(1):176–205, 2002. ISSN 00219991. doi: 10.1006/jcph.2002.7009.

D. C. Hamilton, G. Gloeckler, F. M. Ipavich, W Stüdemann, B. Wilken, G Kremser, and W. Stuedemann. Ring current development during the great geomagnetic storm of February 1986. *Journal of Geophysical Research: Space Physics*, 93(A12):14343–14355, 1988. ISSN 2156-2202. doi: 10.1029/JA093iA12p14343.

A. Harten and G. Zwas. Self-adjusting hybrid schemes for shock computations. *Journal of Computational Physics*, 9(3):568–583, 1972. ISSN 10902716. doi: 10.1016/0021-9991(72)90012-5.

Brian Harvey. *Russian planetary exploration : history, development, legacy, prospects*. 2007. ISBN 9780387496641.

M. Hesse and K. Schindler. A theoretical foundation of general magnetic reconnection. *Journal of Geophysical Research*, 93(A6):5559, 1988. ISSN 0148-0227. doi: 10.1029/JA093iA06p05559.

Michael Hesse, Terry G Forbes, and Joachim Birn. On the Relation between Reconnected Magnetic Flux and Parallel Electric Fields in the Solar Corona. *The Astrophysical Journal*, 631(2): 1227, 2005. ISSN 0004-637X. doi: 10.1086/432677.

W. Horton, J. P. Smith, R. Weigel, C Crabtree, I. Doxas, B. Goode, and J. Cary. The solar-wind driven magnetosphereâĂŞionosphere as a complex dynamical system. *Physics of Plasmas*, 6, 4178, 1999. doi: https://doi.org/10.1063/1.873683.

T. Iijima and T. A. Potemra. Field-aligned currents in the dayside cusp observed by Triad. *Journal of Geophysical Research*, 81(34):5971–5979, 1976. ISSN 01480227. doi: 10.1029/JA081i034p05971.

Joseph B. Jensen, Joachim Raeder, Kristofor Maynard, and W. Douglas Cramer. Particle Precipitation Effects on Convection and the Magnetic Reconnection Rate in Earth's Magnetosphere. *Journal of Geophysical Research: Space Physics*, 2017. ISSN 21699380. doi: 10.1002/2017JA024030.

C Y Johnson. Ion and neutral composition of the ionosphere. *Annals of the IQSY*, 5:197–213, 1969.

Shiva Kavosi. *Kelvin-Helmholtz Instability at Earth's magnetopause: THEMIS Observations and OpenGGCM Simulations*. PhD thesis, University of New Hampshire, 2015.

Michael C. Kelly. *The Earth's Ionosphere: Plasma Physics and Electrodynamics*. Academic Press, 2 edition, 2009. ISBN 978-0-12-088425-4.

C. F. Kennel and H. E. Petschek. Limit on stably trapped particle fluxes. *Journal of Geophysical Research*, 71(1):1–28, 1966. ISSN 0148-0227. doi: 10.1029/JZ071i001p00001.

L. Kepko, R. L. McPherron, O. Amm, S. Apatenkov, W. Baumjohann, J. Birn, M. Lester, R. Nakamura, T. I. Pulkkinen, and V. Sergeev. Substorm Current Wedge Revisited. *Space Science Reviews*, 190(1-4), 2015. ISSN 15729672. doi: 10.1007/s11214-014-0124-9.

L. M. Kistler, C. G. Mouikis, H. E. Spence, A. M. Menz, R. M. Skoug, H. O. Funsten, B. A. Larsen, D. G. Mitchell, M. Gkioulidou, J. R. Wygant, and L. J. Lanzerotti. The source of O+ in the storm time ring current. *Journal of Geophysical Research A: Space Physics*, 121(6):5333–5349, 2016. ISSN 21699402. doi: 10.1002/2015JA022204.

Margaret G. Kivelson and Christopher T. Russell. *Introduction to Space Physics*. Cambridge University Press, 1st edition, 1995. doi: 0521457149.

Stephen Knight. Parallel electric fields. *Planetary and Space Science*, 21(5):741–750, 1973. ISSN 00320633. doi: 10.1016/0032-0633(73)90093-7.

C. M. Komar, P. A. Cassak, J. C. Dorelli, A. Glocer, and M. M. Kuznetsova. Tracing magnetic separators and their dependence on IMF clock angle in global magnetospheric simulations. *Journal of Geophysical Research: Space Physics*, 118(8):4998–5007, 2013. ISSN 21699402. doi: 10.1002/jgra.50479.

William Lotko, Ryan H Smith, Binzheng Zhang, Jeremy E Ouellette, Oliver J Brambles, and John G Lyon. Ionospheric control of magnetotail reconnection. *Science*, 345(6193):184–7, 2014. ISSN 1095-9203. doi: 10.1126/science.1252907.

G Lu, A. D. Richmond, B. A. Emery, P. H. Reiff, O. de la Beaujardière, F. J. Rich, W. F. Denig, H. W. Kroehl, L. R. Lyons, J. M. Ruohoniemi, E. Friis-Christensen, H. Opgenoorth, M. A. L. Persson, R. P. Lepping, A. S. Rodger, T. Hughes, A. McEwin, S. Dennis, R. Morris, G. Burns, and L. Tomlinson. Interhemispheric asymmetry of the high-latitude ionospheric convection pattern. *J. Geophys. Res.*, 99:6491, 1994. ISSN 0148-0227. doi: 10.1029/93JA03441.

J. G. Lyon, J. A. Fedder, and C. M. Mobarry. The Lyon-Fedder-Mobarry (LFM) global MHD magnetospheric simulation code. *Journal of Atmospheric and Solar-Terrestrial Physics*, 66(15-16 SPEC. ISS.):1333–1350, 2004. ISSN 13646826. doi: 10.1016/j.jastp.2004.03.020.

V. G. Merkin, A. S. Sharma, K. Papadopoulos, G. Milikh, J. Lyon, and C. Goodrich. Global MHD simulations of the strongly driven magnetosphere: Modeling of the transpolar potential saturation. *Journal of Geophysical Research: Space Physics*, 110(A9), 2005. ISSN 21699402. doi: 10.1029/2004JA010993.

Kyle R. Murphy, Ian R. Mann, I. Jonathan Rae, Colin L. Waters, Harald U. Frey, Andy Kale, Howard J. Singer, Brian J. Anderson, and Haje Korth. The detailed spatial structure of field-aligned currents comprising the substorm current wedge. *Journal of Geophysical Research: Space Physics*, 118(12):7714–7727, 2013. ISSN 21699402. doi: 10.1002/2013JA018979.

T. Nagatsuma. Conductivity dependence of cross-polar potential saturation. *Journal of Geophysical Research: Space Physics*, 109(A4), 2004. ISSN 21699402. doi: 10.1029/2003JA010286.

Denny M. Oliveira. *A study of interplanetary shock geoeffectiveness controlled by impact angles using simulations and observations*. PhD thesis, University of New Hampshire, 2015.

J. E. Ouellette, B. N. Rogers, M. Wiltberger, and J. G. Lyon. Magnetic reconnection at the dayside magnetopause in global Lyon-Fedder-Mobarry simulations. *Journal of Geophysical Research: Space Physics*, 115(8), 2010. ISSN 21699402. doi: 10.1029/2009JA014886.

E. N. Parker. Dynamics of the Interplanetary Gas and Magnetic Fields. *The Astrophysical Journal*, 128:664, 1958. ISSN 0004-637X. doi: 10.1086/146579.

Harry E. Petschek. Magnetic Field Annihilation. In W. N. Hess, editor, *The Physics of Solar Flares, Proceedings of the AAS-NASA Symposium*, page 425. NASA Spec. Publ. SP-50, 1964. ISBN 9780874216561. doi: 10.1007/s13398-014-0173-7.2.

Kenneth G. Powell, Philip L. Roe, Timur J. Linde, Tamas I. Gombosi, and Darren L. De Zeeuw. A Solution-Adaptive Upwind Scheme for Ideal Magnetohydrodynamics. *Journal of Computational Physics*, 154(2):284–309, 1999. ISSN 00219991. doi: 10.1006/jcph.1999.6299.

J. Raeder and G. Lu. Polar cap potential saturation during large geomagnetic storms. *Advances in Space Research*, 36(10):1804–1808, 2005. ISSN 02731177. doi: 10.1016/j.asr.2004.05.010.

J. Raeder, J. Berchem, and M. Ashour-Abdalla. The importance of small scale processes in global MHD simulations: Some numerical experiments. In T.Chang and J.R. Jasperse, editors, *The Physics of Space Plasmas*, volume 14, page 403, Cambridge, Mass., 1996. MIT Cent. for Theoret. Geo/Cosmo Plasma Phys.

J. Raeder, Y.L. Wang, T.J. Fuller-Rowell, and H.J. Singer. Global Simulation of Magnetospheric Space Weather Effects of the Bastille Day Storm. *Solar Physics*, 204(1/2):323–337, 2001a. ISSN 1573-093X. doi: 10.1023/A:1014228230714.

Joachim Raeder. Global Magnetohydrodynamics - A Tutorial. In Jörg Büchner, Manfred Scholer, and Christian T Dum, editors, *Space Plasma Simulation*, volume 615, chapter Global Mag, pages 212–246. Springer Berlin Heidelberg, Berlin, Heidelberg, 2003. ISBN 978-3-540-00698-5. doi: 10.1007/3-540-36530-3.

Joachim Raeder, Yongli Wang, and Timothy J Fuller-Rowell. Geomagnetic Storm Simulation with a Coupled Magnetosphere-Ionosphere-Thermosphere Model. In P. Song, G. Siscoe, and H. J. Singer, editors, *Space Weather, AGU Geophys. Monogr. Ser.*, volume 125, pages 377–384. American Geophysical Union, 2001b. doi: 10.1029/GM125p0377.

Joachim Raeder, Douglas Larson, Wenhui Li, Emil L. Kepko, and Timothy Fuller-Rowell. OpenGGCM simulations for the THEMIS mission. *Space Science Reviews*, 141(1-4):535–555, 2008. ISSN 00386308. doi: 10.1007/s11214-008-9421-5.

Joachim Raeder, William D. Cramer, Joseph Jensen, Timothy Fuller-Rowell, Naomi Maruyama, Frank Toffoletto, and Hien Vo. Sub-Auroral Polarization Streams: A complex interaction between the magnetosphere, ionosphere, and thermosphere. *Journal of Physics: Conference Series*, 767(1):012021, 2016. ISSN 1742-6588. doi: 10.1088/1742-6596/767/1/012021.

A. D. Richmond and Y. Kamide. Mapping electrodynamic features of the high-latitude ionosphere from localized observations: Technique. *Journal of Geophysical Research*, 93(A6):5741, 1988. ISSN 0148-0227. doi: 10.1029/JA093iA06p05741.

A.D. Richmond, G Lu, B.A. Emery, and D.J. Knipp. The AMIE procedure: Prospects for space weather specification and prediction. *Advances in Space Research*, 22(1):103–112, 1998. ISSN 02731177. doi: 10.1016/S0273-1177(97)01108-3.

A. J. Ridley, T. I. Gombosi, and D. L. Dezeeuw. Ionospheric control of the magnetosphere: conductance. *Annales Geophysicae*, 22(2):567–584, 2004. ISSN 1432-0576. doi: 10.5194/angeo-22-567-2004.

R M Robinson, R R Vondrak, K Miller, T Dabbs, and D Hardy. On calculating ionospheric conductances from the flux and energy of precipitating electrons. *Journal of Geophysical Research (ISSN 0148-0227)*, 92:2565, 1987. ISSN 0148-0227. doi: 10.1029/JA092iA03p02565.

G Rostoker, S.-I. Akasofu, J Foster, R A Greenwald, Y Kamide, K Kawasaki, A T Y Lui, R L McPherron, and C T Russell. Magnetospheric Substorms- Definitions and Signatures. *J. Geophys. Res.*, 85(A4):1663–1668, 1980. doi: https://doi.org/10.1029/JA085iA04p01663.

Tetsuya Sato and Takesi Iijima. Primary sources of large-scale Birkeland currents. *Space Science Reviews*, 24(3):347–366, 1979. ISSN 00386308. doi: 10.1007/BF00212423.

Simon G. Shepherd. Polar cap potential saturation: Observations, theory, and modeling. *Journal of Atmospheric and Solar-Terrestrial Physics*, 69(3):234–248, 2007. ISSN 13646826. doi: 10.1016/j.jastp.2006.07.022.

G. Siscoe, J. Raeder, and A. J. Ridley. Transpolar potential saturation models compared. *Journal of Geophysical Research: Space Physics*, 109(A9):A09203, 2004. ISSN 21699402. doi: 10.1029/2003JA010318.

G. L. Siscoe, G. M. Erickson, B. U Ö Sonnerup, N. C. Maynard, J. A. Schoendorf, K. D. Siebert, D. R. Weimer, W. W. White, and G. R. Wilson. Hill model of transpolar potential saturation: Comparisons with MHD simulations. *Journal of Geophysical Research: Space Physics*, 107 (A6), 2002. ISSN 21699402. doi: 10.1029/2001JA000109.

J A Slavin, S M Krimigis, M H Acuna, B J Anderson, D N Baker, P L Koehn, H Korth, S Livi, B H Mauk, S C Solomon, and T H Zurbuchen. MESSENGER: Exploring mercury's magnetosphere. *Space Science Reviews*, 131(1-4):133–160, 2007. doi: 10.1007/s11214-007-9154-x.

Gary A. Sod. *Numerical Methods in Fluid Dynamics*. Cambridge University Press, Cambridge, 1985. doi: https://doi.org/10.1017/CBO9780511753138.

Jan J. Sojka, Joseph Jensen, Michael David, Robert W. Schunk, Tom Woods, and Frank Eparvier. Modeling the ionospheric E and F1 regions: Using SDO-EVE observations as the solar irradiance driver. *Journal of Geophysical Research: Space Physics*, 118(8):5379–5391, 2013. ISSN 21699402. doi: 10.1002/jgra.50480.

Jan J. Sojka, Joseph B. Jensen, Michael David, Robert W. Schunk, Tom Woods, Frank Eparvier, Michael P. Sulzer, Sixto A. Gonzalez, and J. Vincent Eccles. Ionospheric model-observation comparisons: E layer at Arecibo Incorporation of SDO-EVE solar irradiances. *Journal of Geophysical Research: Space Physics*, 119(5):3844–3856, 2014. ISSN 21699402. doi: 10.1002/2013JA019528.

B Sonnerup. Magnetic field reconnection at the magnetopause: An overview. *Magnetic Reconnection in Space and Laboratory Plasmas*, 30:92–103, 1984. doi: 10.1029/GM030p0092.

B. U. Ö Sonnerup and L. J. Cahill. Magnetopause structure and attitude from Explorer 12 observations. *Journal of Geophysical Research*, 72(1):171, 1967. ISSN 0148-0227. doi: 10.1029/JZ072i001p00171.

B. U. Ö. Sonnerup and L. J. Cahill. Explorer 12 observations of the magnetopause current layer. *Journal of Geophysical Research*, 73(5):1757–1770, 1968. ISSN 0148-0227. doi: 10.1029/JA073i005p01757.

David P. Stern. Euler Potentials. *American Journal of Physics*, 38(4):494, 1970. ISSN 00029505. doi: 10.1119/1.1976373.

David P. Stern. The art of mapping the magnetosphere. *Journal of Geophysical Research*, 99(A9): 17169, 1994. ISSN 0148-0227. doi: 10.1029/94JA01239.

T. Tanaka. Magnetosphere-ionosphere convection as a compound system. *Space Science Reviews*, 133(1-4):1–72, 2007. ISSN 00386308. doi: 10.1007/s11214-007-9168-4.

K. F. Tapping. The 10.7 cm solar radio flux (F10.7). *Space Weather*, 11(7):394–406, 2013. ISSN 15427390. doi: 10.1002/swe.20064.

Frank Toffoletto, Stanislav Sazykin, Robert Spiro, and Richard Wolf. Inner magnetospheric modeling with the rice convection model. *Space Science Reviews*, 107(1-2):175–196, 2003. ISSN 00386308. doi: 10.1023/A:1025532008047.

VytenisM Vasyliunas. Mathematical Models of Magnetospheric Convection and its Coupling to the Ionosphere. In B M McCormac, editor, *Particles and Fields in the Magnetosphere*, volume 17, pages 60–71, Dordrecht, 1970. Dordrecht, Netherlands: D. Reidel. ISBN 978-94-010-3286-5. doi: 10.1007/978-94-010-3284-1_6.

Liang Wang, Ammar H. Hakim, A. Bhattacharjee, and K. Germaschewski. Comparison of multi-fluid moment models with particle-in-cell simulations of collisionless magnetic reconnection. *Physics of Plasmas*, 22(1), 2015. ISSN 10897674. doi: 10.1063/1.4906063.

R. M. Winglee. Ion cyclotron and heavy ion effects on reconnection in a global magnetotail. *Journal of Geophysical Research: Space Physics*, 109(A9), 2004. ISSN 21699402. doi: 10.1029/2004JA010385.

R A Wolf. Effects of ionospheric conductivity on convective flow of plasma in the magnetosphere. *Journal of Geophysical Research*, 75(25):4677–4698, 1970. ISSN 0148-0227. doi: 10.1029/JA075i025p04677.

Steven T. Zalesak. Fully multidimensional flux-corrected transport algorithms for fluids. *Journal of Computational Physics*, 31(3):335–362, 1979. ISSN 10902716. doi: 10.1016/0021-9991(79)90051-2.

B. Zhang, O. J. Brambles, M. Wiltberger, W. Lotko, J. E. Ouellette, and J. G. Lyon. How does mass loading impact local versus global control on dayside reconnection? *Geophysical Research Letters*, 43(5):1837–1844, 2016. ISSN 19448007. doi: 10.1002/2016GL068005.